UNIVERSIDADE
BEIRA INTERIOR

Analysis of the Structural Efficiency of Arch Bridges with High Strength Concrete Filled Tubes

Mohamad Maher Hummeid

Dissertação para obtenção do Grau de Mestre em
Engenharia Civil
(mestrado integrado)

Orientador: Prof. Doutor Clemente Martins Pinto

Janeiro de 2021

Dedications

To my parents,

To my sisters and brother,

To my family and friends,

To the Global Platform for Syrian Students.

Acknowledgments

First of all, I would like to express my gratitude to my thesis supervisor Professor Dr. Clemente Martins Pinto for his patient guidance, continues support, encouragement and useful critiques of this research work. I deeply appreciate all the time, effort and dedication he put with me to complete this work.

I would also like to extend my great appreciation to all my professors and to UBI for receiving me very well. Moreover, I would like to thank my friends who were of great support during my years of study in UBI. A special mention to Abdelhakim Benhamouda, Naim Sedira and Shadi Kalthoum for their support and continues encouragement not only in writing this thesis but throughout all my years of study.

Most importantly, I would like to express my sincere gratitude to the Global Platform for Syrian Students, its founder His Excellency Dr. Jorge Sampaio, his diplomatic adviser, Dr. Helena Barroco and all the staff for the generous opportunity they have given me to study in Portugal. My educational pursuits would not be possible without their endless supports, they were like a family for me during my years of study and I am greatly honored to be part of this family.

Finally, I must express my very profound gratitude to my family for providing me with unfailing support and continuous encouragement throughout my years of study and through the process of researching and writing this thesis. This accomplishment would not have been possible without them.

Abstract

Concrete-filled steel tubes (CFST) have been increasingly applied in long span arch bridges due to their high compressive strength and efficiency in construction. The objective of this work is to evaluate the efficiency of using high strength concrete in long span CFST arch bridges.

Experimental results on the behaviour of CFST elements were collected from literature, aiming to analyze the behaviour of high strength concrete in CFST solutions. The analysis of the results was based on the internal mechanical behaviour and failure mechanism of the concrete core and their effect in the loading capacity of CFST sections.

The analysis has shown that the different behaviour between normal and high strength concrete results in different effects concerning the confinement level and the loading capacity of CFST sections. The steel tube changes the cracking process of the concrete core, contributing to an unfavorable failure mode in case of high strength concrete, which reduces the efficiency of the combination of the steel tube and the high strength concrete core.

An initial design of a long span railway CFST arch bridge was carried out, considering two combinations of materials, namely normal and high strength materials. The application of high strength materials shows the advantages of reducing the structure self-weight and the materials consumption by about the half when compared to normal strength materials.

Keywords

Concrete-Filled Steel Tube; high strength concrete; concrete cracking; arch bridges.

Resumo

Tubos de aço preenchidos com betão (TAPB) têm sido cada vez mais aplicados em pontes em arco de grande vão, devido à elevada capacidade de carga e eficiência na construção. O objetivo desta tese é avaliar a eficiência do uso de betão de alta resistência em pontes em arco TAPB de grande vão.

Com o objetivo de analisar o comportamento de betão de alta resistência em soluções de TAPB, foram recolhidos e analisados resultados experimentais da literatura, sobre o comportamento de elementos da TAPB.

A análise dos resultados baseou-se no comportamento mecânico interno e no mecanismo de rotura do betão dentro do tubo, e o seu efeito na capacidade de carga de seções TAPB.

A análise mostrou que o comportamento diferente entre o betão normal e o de alta resistência resulta em diferentes efeitos quanto ao nível de confinamento e a capacidade de carga de secções TAPB. O tubo de aço altera o processo de fissuração do betão, contribuindo para um modo de rotura desfavorável no caso de betão de alta resistência, o que resulta em menor eficiência da combinação dos tubos de aço com o núcleo de betão.

Adicionalmente, foi realizada uma análise preliminar de uma ponte ferroviária em arco TAPB de grande vão, considerando duas combinações de materiais, nomeadamente materiais de resistência normal e materiais de alta resistência. A aplicação de materiais de alta resistência tem a vantagem de reduzir o peso próprio da estrutura e o consumo de materiais para metade, quando comparados aos materiais de resistência normal.

Palavras-chave

Tubos de aço preenchidos com betão; betão de alta resistência; fissuração do betão; pontes em arco.

Contents

List of Figures

List of Tables

List of abbreviation

AAEM	Age-adjusted effective modulus
CFST	Concrete-filled steel tube
HSC	High strength concrete
LM 71	Load model 71
SLS	Serviceability limit state
UHSC	Ultra-high strength concrete
UHSCFST	Ultra-high strength concrete-filled steel tube
ULS	Ultimate limit state

List of symbols

A_c	Cross-sectional area of concrete
A_s	Cross-sectional area of steel
$A_{,eq}$	Cross-sectional area of the equivalent section
D	Outer diameter of circular tubular sections
E_c	Modulus of elasticity of concrete
E_S	Modulus of elasticity of steel
F_w	Wind force
$G_{kj,sup}$	Dead load
L_{cr}	Buckling length
M_{Ed}	Design bending moment
$M_{y,Ed}$	Design bending moment about the y-y axis
$M_{z,Ed}$	Design bending moment about the z-z axis
M_{Rk}	Characteristic value of the resistance moment of the composite section
$M_{pl,N,Rd}$	Plastic bending resistance taking into account the normal force
N_{Ed}	Design value of the compressive normal force
N_{cr}	Critical normal force
N_{Rd}	Design value of the resistance to compressive force
N_{Rk}	Characteristic value of the composite section to compressive force
$N_{b,Rd}$	Buckling resistance of the section
N_u	Capacity of CFST section
N_{hollow}	Capacity of the hollow steel tube section
$Q_{k,1}$	Live load
SI	Strength index
$T_{k,i}$	Temperature variation
e_o	Imperfection value
d	Outer diameter of circular tubular sections
f_{cd}	Design value of the compressive strength of concrete
f_{ck}	Characteristic value of the compressive strength of concrete
f_y	Nominal value of the yield strength of steel
f_{yd}	Design value of the yield strength of steel
q_{cr}	Critical distributed load
t	Thickness
α	Imperfection factor for buckling curves

λ	Slenderness
$\bar{\lambda}$	Non-dimensional slenderness
χ	Reduction factor for the relevant buckling curve
δ	Vertical deflection
i	Radius of gyration about the relevant axis
Φ	Diameter of the tubes
ρ	Sectional steel ratio
ξ	Confinement factor
$\gamma_{Q,}$	Recommended design factors for ULS combinations
$\psi_{o,i}$	Recommended values of factors for railway bridges

Chapter 1 Introduction

1.1 Introduction

Concrete-filled steel tubes (CFST) have been increasingly used as a structural solution for arch bridges and as columns in high-rise buildings and underground infrastructures due to their several advantages such as high compressive strength and efficiency in construction. The cross-section of concrete-filled steel tube elements is composed of steel tube and concrete core. The steel gives confinement for the concrete, which increases the load-bearing capacity and improves the ductility of the concrete core. Additionally, the concrete core reduces the occurrence of local buckling of the steel tube. The steel tube also acts as a framework for the concrete, which results in efficiency in construction [1].

In CFST solutions, the steel tubes can be filled with normal strength concrete or high strength concrete [2]. With the developments in materials technologies, ultra-high-strength concrete (UHSC) with strength exceeding C100 has been gradually used in CFST solutions forming ultra-high-strength concrete-filled steel tube (UHSCFST). The application of high strength materials in CFST structures can increase the bearing capacity of the structural members, decreasing the consumption of materials, cross-sectional area and structures self-weight. Thus, their use can be advantageous in the construction of high-rise buildings and long-span bridges [3]. Moreover, the concrete core can be more dense and uniform in UHSCFST than the ordinary CFST, due to the finer composition of UHSC making it more suitable for the filling [4].

However, due to some limitations about the mechanical behaviour of high strength concrete when applied in CFST solutions, its application in arch bridges is limited. Limited research has been performed on the use of high strength concrete in CFST solutions. The application of the current design codes is limited to normal strength concrete. For example, Eurocode 4 is applied to concrete grades up to C60, the Chinese codes up to C80. Only the Australian code is applied to concrete grades up to C100, which is considered as a high strength concrete. Therefore, additional research to understand the mechanical behaviour of high strength concrete-filled steel tube is needed to safely design structures using UHSCFST, as long-span arch bridges.

1.2 CFST applications

1.2.1 General applications

CFST solutions are used in different structures such as buildings and bridges. The SEG Plaza in Shenzhen (Figure 1.1 (a)) with 291.6 m height, is one of the earliest application of CFST members in high-rise building. The applied CFST columns have a circular cross-section, composed of C60 concrete and S355 steel. In this case, the quantity of the used steel corresponds to 50% of the needed quantity using simple hollow steel sections [2]. Canton Tower in Guangzhou (Figure 1.1 (b)) is another example with a main body height of 454 m and a pinnacle height of 600 m, where ϕ2000mm×50mm CFST columns were used [2]. In Australia, CFST solutions were applied in several projects including Market City in Sydney, Casselden Place and the Commonwealth Centre in Melbourne [5]. CFSTs have also been widely used in Japan as structural solutions such as bridge piers [6].

Figure 1.1 a) SEG Plaza (adapted from [7]) b) Canton tower (adapted from [2])

1.2.2 Application of CFST solutions in bridges

CFST arch bridges have become a good alternative to reinforced concrete arch bridge and steel arch bridges [8]. CFST use in arch bridges permits to reduce the arch self-weight and to improve the ductility when compared with reinforced concrete arch bridges. Additionally, CFST use is more cost-effective compared to steel arch bridges [9].

The first CFST arch bridge was constructed in the 1930s in the USSR, with a 140m span. Due to limitations in construction methods, no other CFST arch bridges were built for many years. Despite existing some examples of CFST arch bridges around the world, the number of these bridges is small compared to other types of bridges. CFST arch bridges are becoming a very popular solution for use in long-span application owing to their high compressive strength and efficiency in construction. China has gained a world-leading position in the development of CFST arch bridges. Due to the mountainous nature of China, where a lot of rivers rush through deep valleys and ravines, arch bridges are a particularly suitable solution to span over these areas [10]. The chinese researchers have made a great development on the mechanism and construction methods of CFST arch bridges. The improved techniques of concrete pumping and segmental hoisting have expanded the feasibility of CFST arch bridges.

More than 400 CFST arch bridges have been built in China. According to [11], the first Hejiang Yangtze River Highway Bridge (Figure 1.2) is a half-through CFST arch bridge whose main span of 530 m is the longest in CFST arch bridges at present. The arch ribs have a catenary axis with a 1/4 rise-to-span ratio. The arch ribs are two parallel trusses (Figure 1.3), each one consists of 4 tubes with 1300 mm diameter and variable thickness between 22 mm and 34 mm, filled with C60 concrete. The height of the ribs varies between 7 m and 14 m and the width is 4.0 m, with a center to center distance of 25.3 m between the two ribs. Steel tubes with a diameter of ϕ760 mm are used to connect the CFST chords transversely, and tubes with a diameter of ϕ660 mm connect the chords vertically.

Figure 1.2 The First Hejiang Yangtze River Bridge (adapted from [12])

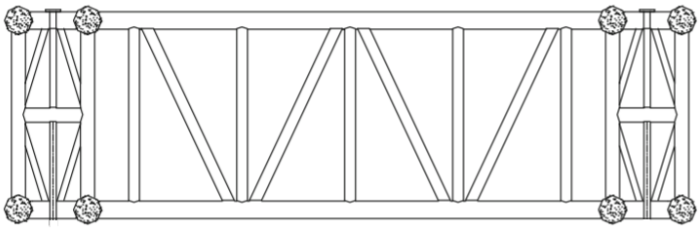

Figure 1.3 The Cross section of the main arch in the first Hejiang Yangtze River Highway Bridge [11]

Wushan Yangtze River Bridge (Figure 1.4) in China is a combined highway and railway bridge with a main span of 460 m [13], the half-through arch consists of two CFST truss ribs and the height of the rib section is various ranging from 7 m in the crown to 14 m in the spring, with a center to center distance of 19.7 m between the two ribs. Each rib consists of four ϕ1220×22mm CFSTs with C60 concrete (Figure 1.5). The arch longitudinal axis is a catenary curve [14].

Figure 1.4 Wushan Yangtze River Bridge (adapted from [15])

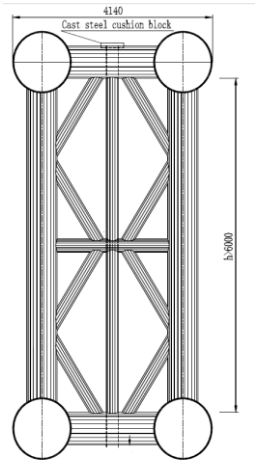

Figure 1.5 Sketch of the arch rib in Wuxia Yagntze River Bridge (units in mm)(adapted from [14])

The Liancheng Highway Bridge (Figure 1.6) with a span of 400 m has a unique configuration, combining arches and stayed-cables to support the deck structure. The two ribs have a rectangular cross-section with a height of 9 m, with 6 CFSTs in each rib. The dimensions of the CFSTs are variable between ϕ850mm×28mm and ϕ850mm×20mm [16].

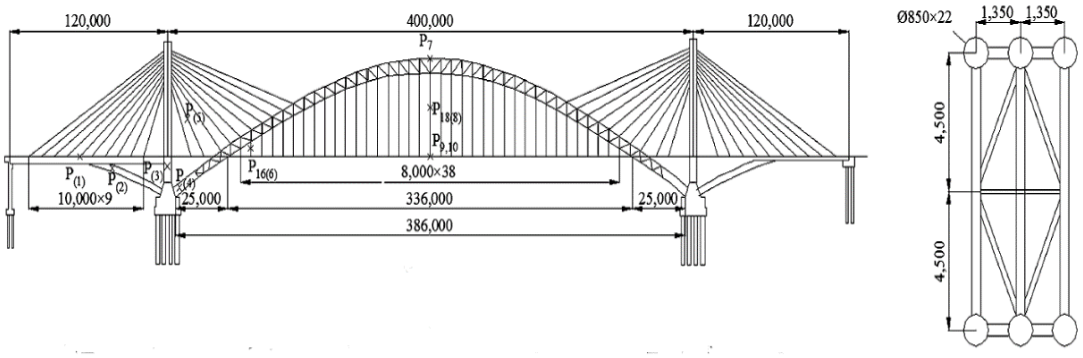

(a) (b)

Figure 1.6 Liancheng Bridge a) Elevation view b) Rib cross section (adapted from [16]) (units in mm)

Zhijing River Bridge with a main span of 430 m (Figure 1.7), is another example of long span CFST arch bridges in China.

Figure 1.7 Zhijing River Bridge (adapted from [17])

Critical priorities arise in the design of high-speed railway bridges, which become increasingly longer. Recent examples of long span railway arch bridges are the Yachi River Bridge [18] (Figure 1.8), with 436 m span, and the Nujiang Railway Bridge Darui [19] (Figure 1.9), with 490 m span. Both bridges were constructed in China, using steel arches. In the case of Yachi River Bridge, the flanges are covered by concrete, totally in the upper flanges and partially in the bottom flanges.

Figure 1.8 Yachi River Bridge [20]

Figure 1.9 Nujiang Railway Bridge Darui [21]

The stiffness requirements for long-span railway bridges are satisfied in "massive" concrete arches as in Beipanjiang Railway Bridge [22] (Figure 1.10), which is one of the most important railway bridges in China. In this case, CFST elements were used in the "skeleton" that supported the construction of the concrete arch and contribute to their section resistance. According to [13], using CFST elements in the "skeleton" permitted to reduce about 50% in steel consumption, when compared with a simple steel solution. The stiffened CFST arch has a catenary axis line. The main span is 445 m and the rise to span ratio is 1/4.45. The arch section height is 9 m and the width is variable between 20 and 28 m (Figure 1.11). Four CFSTs on each side with a diameter of 750 mm filled with C80 and the surrounding concrete is C60 [23].

Figure 1.10 Beipanjiang Railway Bridge, with a main span of 445 m [24]

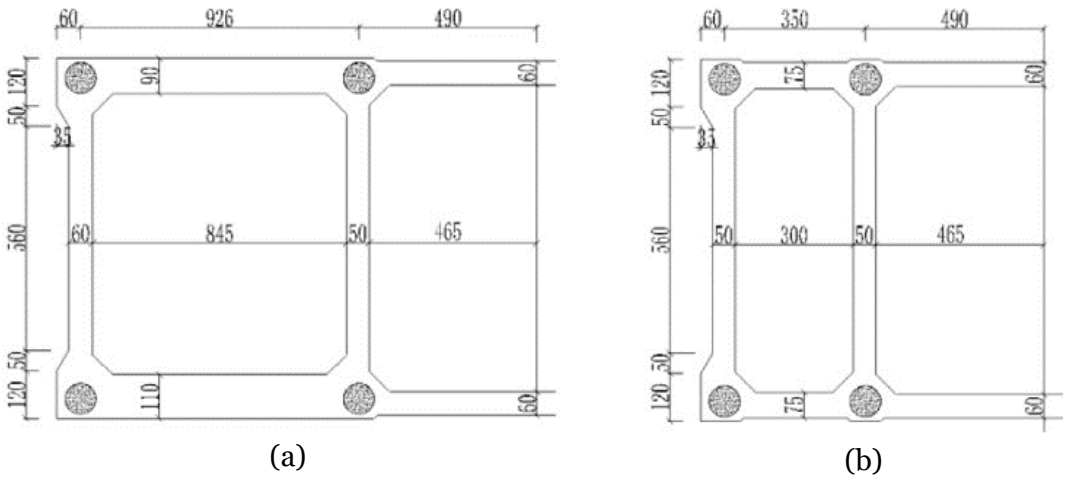

Figure 1.11 Cross section of the arch of Beipanjiang Bridge a) arch springing b) arch crown (adapted from [23]) (units in cm)

1.2.3 Application of high strength concrete in CFST solutions

High-strength concrete (HSC) and ultra-high-strength concrete (UHSC) have become an interesting alternative to normal strength concrete due to the high compressive strength, improving the bearing capacity and reducing the cross-sectional size, materials consumption and the structural self-weight. However, material brittleness is one of the disadvantages of high strength concrete. Filling high strength concrete into steel tubes (UHSCFST) can improve the compressive brittleness of UHSC [4] [25].

Therefore, UHSCFST has been gradually applied in civil engineering. In Japan, Techno station in Tokyo is one of the application of high strength concrete in CFST solutions [25], with S780 steel tubes filled with C160 concrete. Another example of UHSCFST application in Japan is Abeno Harukas, where a S780 steel tube was filled with C150 [25]. High-strength concrete has been used in some bridges elements, such as piers and arches. In Labajin

Bridge (Figure 1.12), C80 was filled into tubular columns and used in the 182.5 m height piers. Another application of high strength concrete is in Zhaohua Jialingjiang Bridge (Figure 1.13), with 364 m span, a C80 concrete was used in the encased CFST elements [26]. C100 concrete was used in CFST elements in Modaoxi Bridge (Figure 1.14) with a main span of 280 m and in Guanshen Qujiang Bridge with a main span of 320 m [3]. In Beipanjiang Railway Bridge, referred above, C80 concrete was used in CFST elements of the "skeleton" that supported the arch construction.

Figure 1.12 Labajin Bridge, pier height of 182.5 m [27]

Figure 1.13 Zhaohua Jialingjiang Bridge, main span of 364 m [28]

Figure 1.14 Modaoxi Bridge, main span of 280 m [29]

1.3 Objectives

The present work intends to study and evaluate the efficiency of high strength concrete for long span CFST arch bridges. The specific aims are as follows:

- Understand and analyze experimental studies performed by different authors on the behaviour of CFST elements using high strength concrete.
- Initial design of a long span arch bridge, comparing the use of UHSCFST and ordinary CFST.
- Present a comparative structural analysis between the two solutions, taking into account geometrical nonlinearities and the effect of the concrete creep on the long-term deformations and stresses redistribution.

Chapter 2 Literature review

2.1 Description of CFST solutions and techniques

Different cross-sections can be used in CFST members such as square section, rectangular section and circular section. The circular section theoretically gives the best confinement for the concrete and local buckling is more expected to happen in square and rectangular sections [2].

A comparison study has been made by Lin-Hai Han [2] on stub columns with hollow steel, reinforced concrete and CFST sections, with the same dimensions and the same type of concrete, with 78 MPa compressive strength. The used steel has a yield strength of 363 MPa. The measured results showed that the ultimate strength of the CFST column is greater than the summation of the strength of the steel column and the reinforced concrete column (Figure 2.1 (a)). The load versus deformation relationship (Figure 2.1 (b)) shows that the ductility of the column increased significantly when using CFST section.

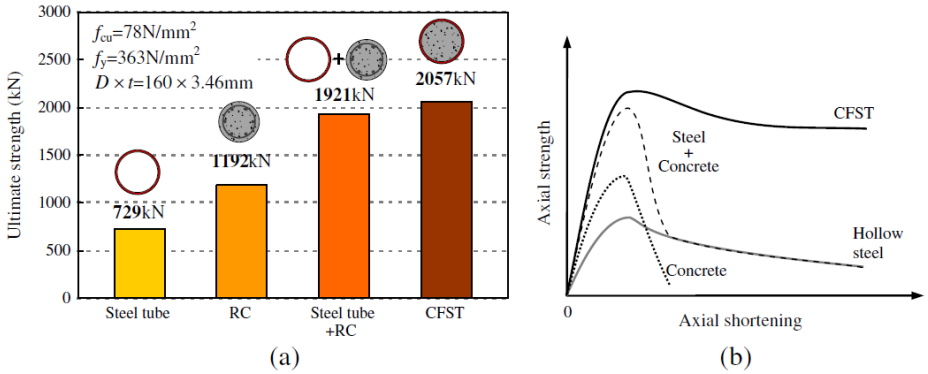

Figure 2.1 Axial Compressive Behavior of CFST Column (adapted from [2])

Various types of structural steel can be used in CFST sections including normal carbon (mild) steel, high-performance fire-resistant steel, high strength steel and stainless steel. The same for concrete, where normal-weight concrete, normal and high strength concrete can be used in CFST solutions. Strict attention should be paid to the water to cement ratio since the excess water cannot be removed from the sealed tube. Hence, the water to cement ratio should not exceed 0.4 for normal weight concrete [2]. Different combinations of materials, concerning compressive strength, can be adopted. However, better structural behaviour is achieved when the strength of the used materials is matched [30]. The most commonly used steel grades in CFST arch bridges in China are Q235 and Q345 which are similar to S235 and S355 grades in Eurocode standards [1]. The common concrete grades of investigated CFST arch bridges in China are shown in Figure 2.2.

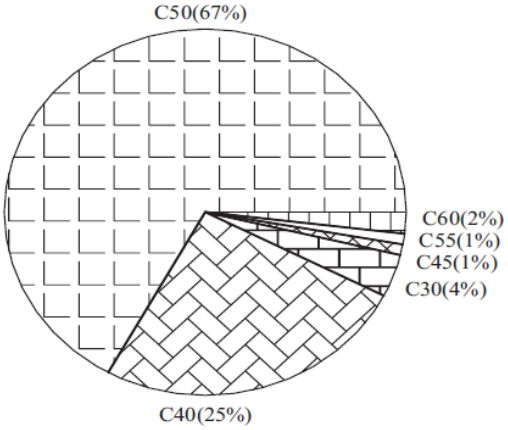

Figure 2.2 Typical concrete grades used in CFST arch bridges in china (adapted from [1])

CFST is an ideal composite structure to use in long-span arch bridges, in which the arch ribs can support large axial pressure [31]. Moreover, the arch steel tube can be filled with concrete with no need for the formwork, making the erection of long-span arches easier. Additionally, the use of arches can significantly reduce bending moments. These advantages enhance the structural efficiency of the CFST arch system [32] [33]. With the developments of construction technologies and the advanced analysis, engineers have been able to gradually increase the span of CFST arch bridges. The development of the maximum span of CFST arch bridges in china is shown in Figure 2.3.

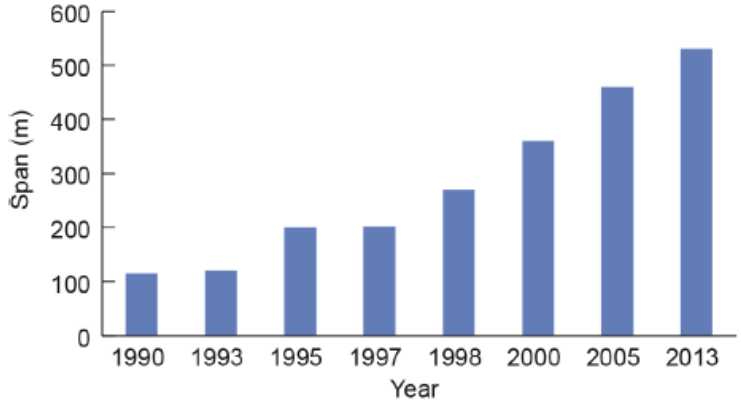

Figure 2.3 The development of the maximum span in CFST arch bridges in china (adapted from [13])

The structural configuration of CFST arch bridges can be categorized into main five types: deck arch, half-through true arch, through deck-stiffened arch, through rigid-frame arch and fly-bird-type arch (Figure 2.4). The axis of the arch should be close to the compression line to take the advantage of CFST structure. Different configurations are used for the axis such as catenary and parabola functions. The data about different constructed bridges indicates that catenary or parabola are used in most through and half-through arches and catenary configuration is the most adopted for deck arches [1]. Several cross-sectional

shapes can be used in the CFST arch ribs, including single tube, dumbbell-shaped, trussed type among others (Figure 2.5). Usually trussed rib is more suitable for long span arches [10].

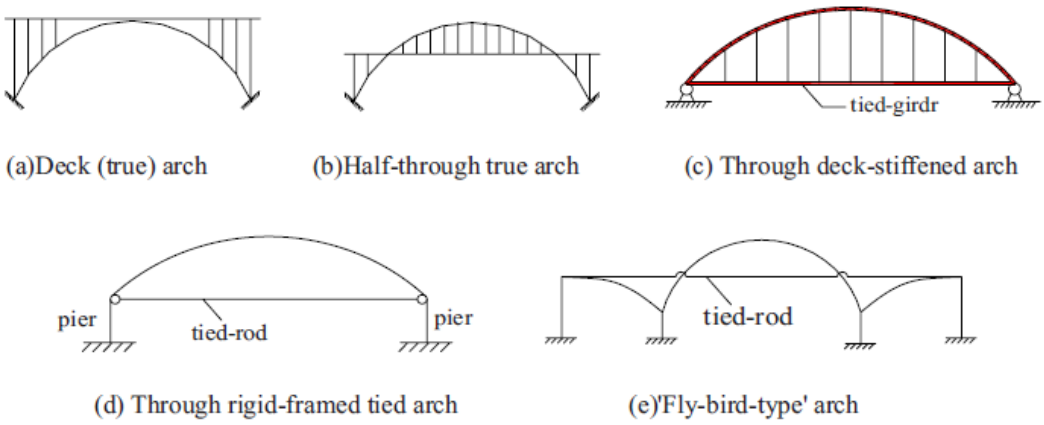

Figure 2.4 Main types of CFST bridges (adapted from [1]).

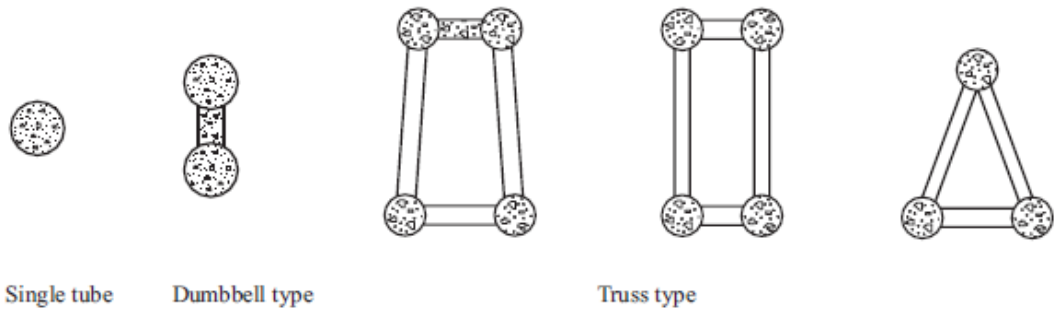

Figure 2.5 Typical ribs section in CFST arch bridges (adapted from [1])

In the construction of CFST bridges, the steel tube is erected at first, which is the most important stage in the construction of CFST arch bridges, and then it is filled in with the pumped concrete [13] [1]. The concrete curing process is simplified inside the steel tube as the tube prevents moisture from evaporating making suitable humidity conditions and saving the water curing process [31]. The most common construction methods of CSFT bridges are cantilever method, swing method and scaffolding method [8]. The cantilever method is the most adopted for the construction of CFST arch bridges. In this method cables controlled by jacks are used to guarantee equilibrium and stability during construction, achieving high precision, the arch is fixed and consolidated segment by segment. This method has been used to erect hundreds of arch bridges including the First Hejiang Yangtze River Bridge (with a main span of 530 m) (Figure 1.2) and the Wushan Yangtze River Bridge (with a main span of 460 m) (Figure 1.4). The swing method includes vertical and horizontal swing. In the vertical swing method, semi-arch rips are fabricated and then lifted up to the design level. Examples of CFST arch bridges constructed by this method are Wuzhou

Guijiang Bridge and Jing-hang Canal bridges in China. The horizontal swing method is based on a pushing system using jacks with a high rotation capacity. The Beipanjiang Railway Bridge (Figure 1.10) is a case where the horizontal swing method was adopted [13] [34].

Figure 2.6 Erection procedure by cantilever method in Wushan Yangtze River Bridge (adapted from [1])

The concrete should be poured into the steel tube of the arch rib in one time in order to ensure the integrity of the infilled concrete. For example, according to [14], in Wushan Yangtze River Bridge, three pouring ports were used at each side of the tube (Figure 2.7). The concrete pouring starts at arch spring using port no.1 until the slurry gets out of the slurry outlet of pouring port no.2. The air then is released from the tube using valves at pouring port no.2 and the concrete is pumped using pouring port no.2. By the same process, the tube is filled until the top of the arch.

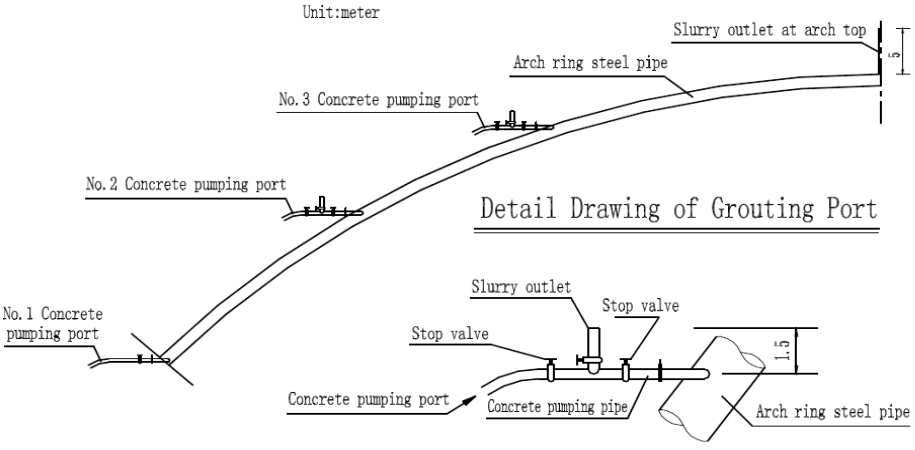

Figure 2.7 Indication sketch of concrete-filled steel pipe grouting of the main arch (adapted from [14])

2.2 Codes for CFST design

As the application of CFST structures is gradually increasing around the world, several national standards provide guidelines for the design of this type of structures such as Eurocode 4 part 1-1 (design of composite steel and concrete structures) [35], American Institute of Steel Construction (Specification for Structural Steel Buildings) AISC 360-16 [36], Standards Australia (Composite Structures) AS 2327 [37], Architectural Institute of Japan (AIJ) (Recommendations for Design and Construction of Concrete Filled Steel Tubular Structures) [38] and China National standard (Technical code for CFST Arch Bridges) GB 50923-2013 [39]. However, the chinese code [39] is the only one specified for CFST arch bridges. In addition to the different design codes, various authors have proposed models for predicting the ultimate load capacity of CFST elements [40]–[45] among others. In this section, a summary of design recommendations is presented according to different design codes and researches, in addition to aspects related to the applicability of these methods in high-strength materials.

The applicability of the most current codes is limited to normal strength materials. However, the Australian standard includes high strength concrete up to 100 MPa and high strength steel up to 690 MPa. Table 2.1 contains the strength limits of concrete and steel in different design codes.

Table 2.1 Materials strength limits in current design codes

Design code	Concrete compressive strength (MPa)	Steel yield stress (MPa)
EC4 [35]	60	460
GB 50923 [39]	70	420
AS 2327 [37]	100	690
AISC 360-16 [36]	69	525
AIJ [38]	90	440

The expression suggested by EC4 [35] to calculate the compressive strength of CFST sections, for relative slenderness $\bar{\lambda} \leq 0.5$ and $e/d < 0.1$, is defined in equation (2.1), where d is the diameter of the tube and e is the loading eccentricity. The confinement effect is taken into account by a coefficient (η_c) for the concrete where concrete strength is improved, while the steel strength is reduced by a coefficient (η_s) as the hoop stresses decrease the effective yield strength of the steel. To consider the global buckling effect, a reduction factor χ is multiplied by the strength of the column. This factor is related to the relative slenderness

and the buckling curve. However, EC4 does not provide a specific approach for columns with relative slenderness beyond the limit $\bar{\lambda}$≤0.5.

$$N_{pl,Rd} = \eta_s A_s f_{yd} + A_c f_{cd}\left(1 + \eta_c \frac{t}{D}\frac{f_{yd}}{f_{cd}}\right) \tag{2.1}$$

With

$$\eta_c = \eta_{c0}\,(1 - 10e/d) \tag{2.2}$$

$$\eta_s = \eta_{s0} + (1 - \eta_{s0})(10e/d) \tag{2.3}$$

$$\eta_{c0} = 4.9 - 18.5\,\bar{\lambda} + 17\,\bar{\lambda}^2 \geq 0 \tag{2.4}$$

$$\eta_{s0} = 0.25(3 + 2\bar{\lambda}) \leq 1 \tag{2.5}$$

$$\bar{\lambda} = \sqrt{\frac{N_{pl,Rk}}{N_{cr}}} \tag{2.6}$$

Where $N_{pl,Rk}$ is the characteristic value of the plastic resistance to compression and N_{cr} is the critical normal force for the relevant buckling mode, calculated with the effective flexural stiffness defined by expression (2.7). A reduction is considered in the concrete stiffness due to cracking.

$$(EI)_{eff} = E_s I_s + 0.6E_c I_c \tag{2.7}$$

The recommendation concerning the steel contribution in the section axial resistance should satisfy the expression (2.8).

$$0.2 \leq \frac{A_s f_y}{A_s f_y + A_c f_{ck}} \leq 0.9 \tag{2.8}$$

The diameter to thickness ratio should not exceed the limit defined in (2.9).

$$\frac{D}{t} \leq 90\frac{235}{f_y} \tag{2.9}$$

In the Australian standard AS 2327 [37], the ultimate strength of CFST elements is given by expression (2.10). The confinement effect of concrete provided by the steel tube is considered for circular sections. To account for local buckling effect, a factor (k_f) is used, which corresponds to the ratio between the effective area and the gross area of the steel tube section. Expression (2.10) is multiplied by a reduction factor (α_c), based on member slenderness, to obtain the strength of a CFST column.

$$N_{us} = k_f \eta_s A_s f_{yd} + A_c f_{cd}\left(1 + \eta_c \frac{t}{D}\frac{f_{yd}}{f_{cd}}\right) \tag{2.10}$$

The slenderness ratio should not exceed a limit defined in expression (2.11).

$$\frac{D}{t}\frac{f_y}{250} \leq 0.19\frac{E_s}{f_y} \tag{2.11}$$

Unlike EC4, AS 2327 does not consider a reduction in the flexural stiffness of concrete.

$$(EI)_{eff} = E_s I_s + E_c I_c \tag{2.12}$$

In the American standard AISC 360-16 [36], different types of sections are considered, as defined in Table 2.2.

Table 2.2 Section classification according to AISC 360-16

Section type	Compact section	Non-compact section	Slender-element section
Slenderness $\lambda = d/t$	$\lambda \leq \lambda_p$	$\lambda_p \leq \lambda \leq \lambda_r$	$\lambda_r \leq \lambda$

Where:

$$\lambda_r = 0.19\frac{E_s}{f_y} \tag{2.13}$$

$$\lambda_p = 0.09\frac{E_s}{f_y} \tag{2.14}$$

For compact circular sections, the ultimate compressive strength is given by expression (2.15). The steel tube is assumed to yield before buckling. A limitation for the cross-sectional areas of the steel tube and the concrete core is given in expression (2.16).

$$N_u = N_p = A_s f_{yd} + 0.95 A_c f_{cd} \tag{2.15}$$

$$A_s \geq 0.01(A_s + A_c) \tag{2.16}$$

The ultimate compressive strength of non-compact sections is given in expression (2.17). The compressive strength is reduced due to considerable volumetric dilation when the

concrete is subjected to compressive stresses of $0.7f_c$, and the steel tube is expected to yield with local buckling.

$$N_u = N_p - \frac{N_p - N_y}{(\lambda_r - \lambda_p)^2}(\lambda_r - \lambda_p)^2 \tag{2.17}$$

Where:

$$N_y = A_s f_y + A_c 0.7 f_c \tag{2.18}$$

The ultimate compressive strength for slender circular sections is given in expression (2.19). A reduction is considered in the concrete strength due to a shortage of confinement effect. The steel tubes are expected to undergo an elastic local buckling.

$$N_u = A_s f_{cr} + A_c 0.7 f_c \tag{2.19}$$

With

$$f_{cr} = \frac{0.72 f_y}{(D f_y / E_S t)^2} \tag{2.20}$$

The strength of a CFST column is given as:

$$N_{uc} = N_u \left(0.658^{\frac{N_u}{N_{cr}}}\right) \quad \text{for} \quad \frac{N_u}{N_{cr}} \leq 2.25 \tag{2.21}$$

$$N_{uc} = 0.877 N_{cr} \quad \text{for} \quad \frac{N_u}{N_{cr}} > 2.25 \tag{2.22}$$

With

$$N_{cr} = \frac{\pi^2 (EI)_{eff}}{L_e^2} \tag{2.23}$$

The effective flexural stiffness is calculated as:

$$(EI)_{eff} = E_s I_s + C_3 E_c I_c \tag{2.24}$$

With

$$C_3 = 0.45 + 3\frac{A_s}{A_s + A_c} \leq 0.9 \tag{2.25}$$

The slenderness limit should satisfy the expression (2.26).

$$\frac{D}{t} \leq 0.31 \frac{E_s}{f_y} \tag{2.26}$$

Architectural Institute of Japan (AIJ) [38] provides a design method for CFST columns in the standard for composite concrete and steel (SRC). The ultimate compressive strength of a CFST column is calculated considering three situations as follows:

$$N_{u1} = N_{u,c} + 1.27 N_{u,s} \quad \text{for} \quad \frac{l_k}{D} \leq 4 \tag{2.27}$$

$$N_{u2} = N_{u1} - 0.125(N_{u1} - N_{u3}).(\frac{l_k}{D} - 4) \quad \text{for} \quad 4 < \frac{l_k}{D} \leq 12 \tag{2.28}$$

$$N_{u3} = N_{cr,c} + N_{cr,s} \quad \text{for} \quad 12 < \frac{l_k}{D} \tag{2.29}$$

Where:

l_k: Effective length of a CFST column

$N_{u,c}$: Ultimate strength of a concrete column

$N_{u,s}$: Ultimate strenght of a steel column

$N_{cr,c}$: Buckling strength of a concrete column

$N_{cr,s}$: Buckling strength of a steel column

The confinement effect is considered in short columns with circular sections as shown in equation (2.27). For slender columns, the strength of the section is calculated by summing the buckling strengths of the steel tube and the infilled concrete columns separately. The limitation regarding the D/t ratio is given in expression (2.30). The code also suggests a limit for the maximum effective length l_k of the CFST compression members shown in expression (2.31).

$$\frac{D}{t} \leq 1.5 \frac{23500}{F} \tag{2.30}$$

Where F is a standard strength to determine allowable stresses of steel.

$$\frac{l_k}{D} \leq 50 \tag{2.31}$$

There are no systematic standards for CFST arch bridges' design. Instead, two methods are adopted for designing such bridges, load and resistance factor (LRFD) method, used for designing concrete and masonry bridges, which is based on inelastic behaviour, and the allowable stress design method (ASD), used for designing steel and timber bridges. The (LRFD) method is adopted for highway bridges and (ASD) method is usually used for railway bridges [1] [12]. However, the norm GB 50923-2013 (China National Standard-

Technical Code for CFST Arch Bridges) [39] developed in 2013, is considered to be the most important design code for CFST arch bridges in china [12]. This code provides recommendations related to the design and construction of highway CFST arch bridges. The expression adopted in this code to calculate the ultimate capacity of a single CFST member with a circular section in axial compression is as follows:

$$N_0 = k_3(1.14 + 1.02\xi_0)(1 + \rho_c)f_{cd}A_c \tag{2.32}$$

Where ξ_0 is the confinement factor, calculated by expression (2.33), k3 is a conversion coefficient for design compressive strength and ρ_c is the steel ratio.

$$\xi_0 = \frac{A_s f_{yd}}{A_c f_{cd}} \tag{2.33}$$

The expression (2.32) is also applied to dumbbell-shaped and truss CFST stub columns, by summing the strength of the tubes in the section in addition to the connection steel webs plates. For members in eccentrically compression, expression (2.32) is used considering a reduction factor of eccentricity ratio. The expression (2.32) considers a stability factor when applied to slender CFST columns.

The equivalent beam-column method is adopted to predict the ultimate load-carrying capacity of CFST arches, where an arch rib is considered as a single beam-column with an effective length using a reduction factor of 0.36 for fixed arches, 0.54 for two-hinge arches and 0.58 for three-hinge arches. In bridges with a span no larger than 300m, an empirical equation may be used to estimate the section height of the arch rib H for uniform cross sections (2.34). The width may be 0.40H to 0.75H.

$$H = k_1 k_2 \left[0.2\left(\frac{l_{01}}{100}\right)^2 + \frac{l_{01}}{100} + 1.2\right] \tag{2.34}$$

Where l_{01} is the arch span, k_1 is a load level coefficient and k_2 is a driveway coefficient.

The recommendations regarding the steel tube suggest that the thickness of the tube should be at least 8mm, the diameter to thickness ratio should be within the limits defined in expression (2.35) and the steel ratio should be within the limits defined in expression (2.36).

$$35\frac{235}{f_y} \leq \frac{D}{t} \leq 100\frac{235}{f_y} \tag{2.35}$$

$$0.04 \leq \rho = \frac{A_s}{A_c} \leq 0.20 \tag{2.36}$$

The presented formulas defined in the current codes are applied to normal strength concrete as mentioned above. Thus, beyond the description of the codes above, a survey of research about the design of CFST sections using high strength concrete is presented. Thai

et al. [46] presented a reliability study on EC4 [35], AISC 360-16 [36] and AS 2327 [37], based on 3208 columns' test data including circular stub and long columns, circular beam-columns as well as stub, slender rectangular columns and rectangular beam-columns, with a considerable number of columns exceeding the slenderness limits and the strengths of the materials provided by the design codes. The conclusion of the study is that the limits of materials strength and slenderness can be extended for higher levels in the three codes. The AISC 360-16 [36] gives the most conservative approach. Liew et al. [47] carried out experiments on CFST columns including steel tubes filled with ultra-high-strength concrete and concluded that EC4 could be used for predicting the ultimate capacity of short columns filled with UHSC with strength up to 200 MPa, while more investigation is needed for longer columns. Guler et al. [48] stated that EC4 overestimates the axial compressive strength of high strength CFST, and therefore cannot be safely applied for CFST with concrete compressive strength higher than 100 MPa, while AISC 360-16 [36] is too conservative. Portoles et al. [49] reported that when the column is eccentrically loaded, EC4 [35] can be used safely for HSC and UHSC, while it is less accurate when the columns are centrically loaded. Additionally, the buckling curves should be reviewed. Huang et el. [50] performed comparison between AS 2327 [37], EC4 [35] and AISC 360-16 [36] based on experimental tests on stub and slender CFST columns with concrete strengths up to 100 MPa. The results show that the limits of these codes can be safely extended to include high strength concrete. Chen et al. [4] confirmed that AISC 360-16 [36], EC4 [35] and AIJ [38] provide conservative prediction methods for UHSCFSTs ultimate capacity, based on experimental tests on UHSCFST circular and square specimens and comparing their ultimate capacity to the three codes. According to the results, the EC4 [35] is the most accurate. Xiong et al. [51] reported that for short CFST columns incorporating high strength and ultra-high strength materials, the limits in AISC 360-16 [36], EC4 [35] and AIJ [38] could be extended to include concrete with compressive strength up to 190 MPa. Hoang et al. [52], based on an analytical study, reported that AISC 360-16 [36] approach is appropriate to estimate the ultimate capacity of UHSCFSTs when the entire section is loaded while the AIJ [38] gives the best estimation when the loading is applied on the concrete core. EC4 [35] and AIJ [38] become less accurate with the increase of D/t ratio while AISC provides good estimations for this case. EC4 [35] had the best estimations with high confinement index.

A number of authors have proposed models and recommendations for the design of CFST members incorporating high strength materials. Liew et al. [25] presented a design guide for CFST members with a concrete compressive strength between 90 MPa and 190 MPa and steel yield strength not exceeding 550 MPa using a reduction factor of 0.8 for the compressive strength of concrete and therefore ignoring the confinement effect. A model

proposed by Chen et al. [4] for circular and square UHSCFST considering the confinement effect is as follows:

$$N_u = f_y A_s + (1 + k) f_c A_c \tag{2.37}$$

with $$k = 0.17 - 0.0013 D/t \sqrt{f_y/235} \quad \text{for circular sections} \tag{2.38}$$

$$k = 0.3 - 0.004 B/t \sqrt{f_y/235} \quad \text{for square sections} \tag{2.39}$$

Hoang et al. [52] have proposed a simplified model to predict the ultimate capacity of circular UHSCFSTs for two cases of loading pattern as shown in expressions (2.40) and (2.41). The two formulas are valid for concrete compressive strength between 150 MPa and 200 MPa, steel yield strength between 235 MPa and 460 MPa, and confinement index between 0.1 and 0.7.

$$N_u = (1 + 1.27\xi) A_c f_c \quad \text{Loading on entire section} \tag{2.40}$$

$$N_u = (0.8 + 1.8\xi) A_c f_c \quad \text{Loading on concrete core} \tag{2.41}$$

2.3 Survey of experimental results

In order to come to a better understanding of the mechanical behaviour of CFSTs with high strength concrete, discussions on different test results are presented in this section, based on experimental results collected from [3], [4], [58], [25], [30], [51], [53]–[57]. The parameters used to evaluate the performance of CFSTs are the confinement factor (ξ) and strength index (SI). The confinement factor (ξ) is considered as a key factor affecting the interaction between the concrete core and the steel tube, and can be defined from equation (2.42). Strength index (SI) is another relevant parameter used to evaluate the capacity of CFST sections and can be calculated from equation (2.43).

$$\xi = \frac{f_y A_s}{f_c A_c} \tag{2.42}$$

$$SI = \frac{N_u}{N_{hollow} + f_c A_c} \tag{2.43}$$

Where N_u is the capacity of CFST section; N_{hollow} is the capacity of the hollow steel tube section; f_y is the yield strength of steel; f_c is the compressive strength of concrete; A_c and A_s are the areas of the concrete core and the steel tube, respectively.

Figure 2.8 contains the relation between the compressive strength of concrete and strength index (SI) with different levels of concrete compressive strength. A particular result using expansive agent is also shown.

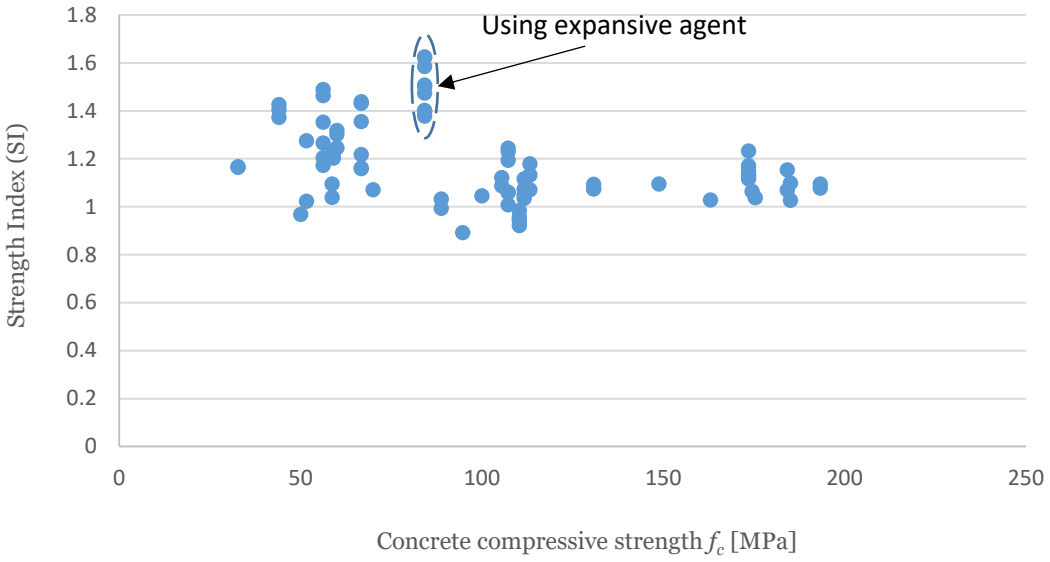

Figure 2.8 Relation between the compressive strength fc and strength index (SI)

Separating the results of normal strength concrete and high strength concrete (f_c >100 MPa), the strength index is generally higher when normal strength concrete is used, despite some dispersion of values above and below 1.2. The strength index is generally below 1.2 for high strength concrete as shown in Figure 2.10, which demonstrates the relatively reduced confinement effect of the steel tube. The influence of the expansive agents is evident, in which the obtained strength index is higher than 1.4.

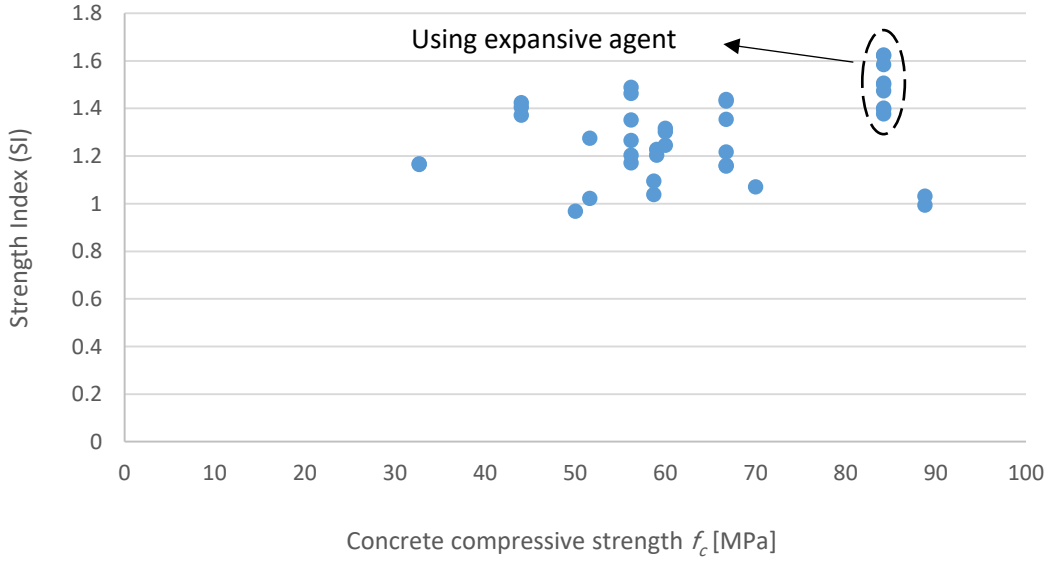

Figure 2.9 Relation between concrete compressive strength and strength index (SI) for concrete with compressive strength lower than 100 MPa

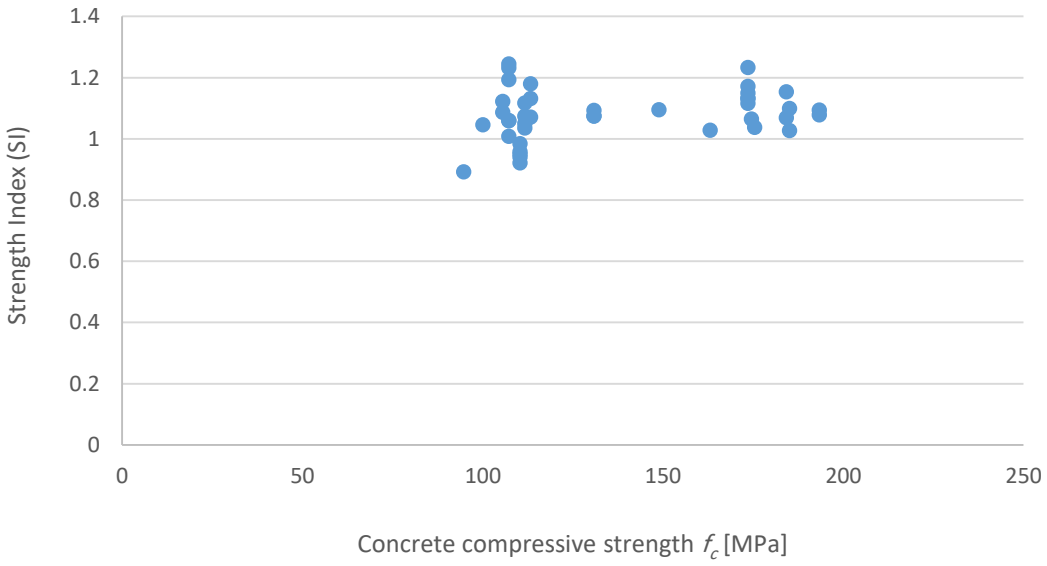

Figure 2.10 Relation between concrete compressive strength and strength index (SI) for concrete with compressive strength higher than 100 MPa

The relation between the confinement factor (ξ) and strength index (SI) is presented in Figure 2.11, Figure 2.12 and Figure 2.13. The results show that higher confinement effect implies higher strength index. However, the separation between normal strength concrete and high strength concrete shows different effects between the two levels of strength. For normal strength concrete, the strength index tends to increase when the confinement factor is increased, which does not happen with high strength concrete.

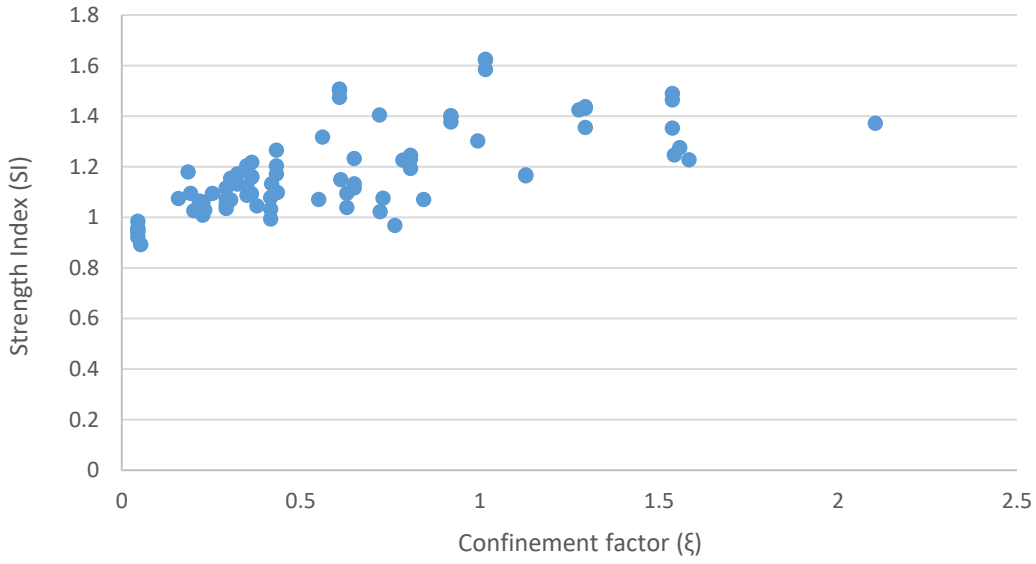

Figure 2.11 Relation between the strength index and the confinement factor

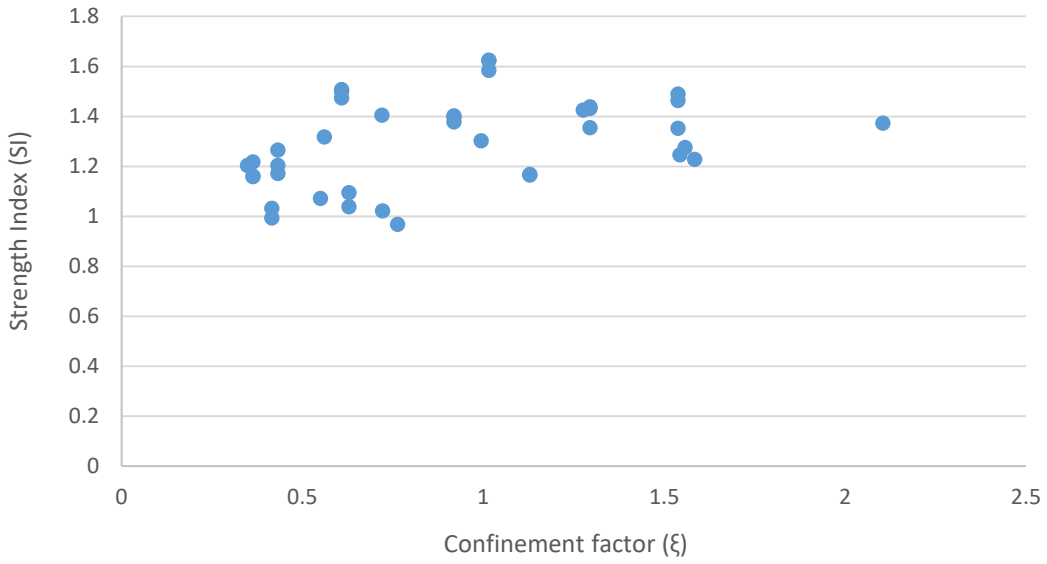

Figure 2.12 Relation between the confinement factor and the strength index for concrete with compressive strength lower than 100 MPa

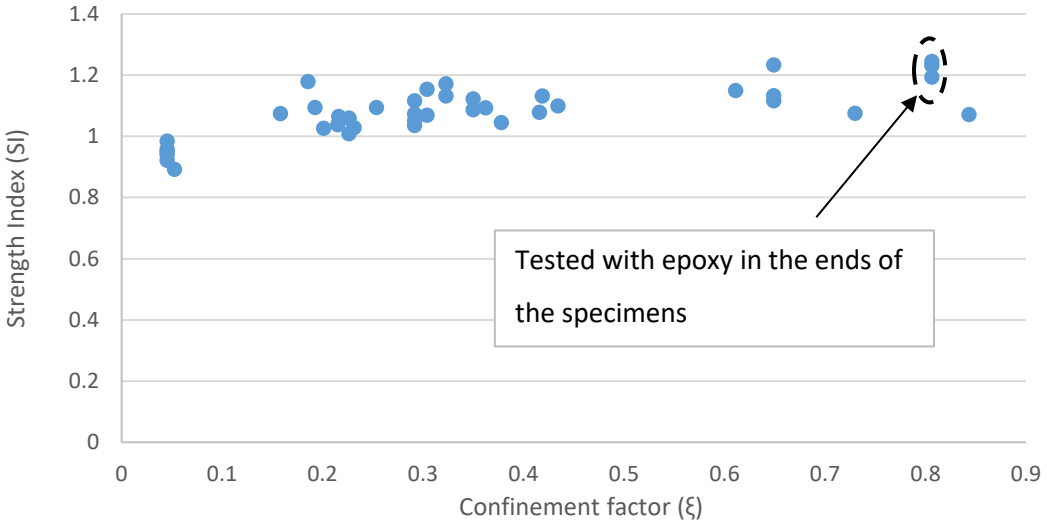

Figure 2.13 Relation between the confinement factor and the strength index for concrete with compressive strength higher than 100 MPa.

The results from [4] for different concrete grades show that the confinement effect is not clear when steel cross-sectional area is increased (Figure 2.14 and Figure 2.15), which theoretically corresponds to the increase of the confinement effect. Strength index tends to decrease with the confinement factor increasing. The reduction is more significant for the concrete with 113 MPa compressive strength. It is also obvious that the confinement provided by the steel tube is more significant in normal strength concrete. The two types of tested high strength concrete differ only in the quantity of used steel fibers. The tested

normal concrete differs from the high strength concrete by the use of coarse aggregate. Circular sections are expected to have more confinement effect when compared to square sections. However, the comparison of Figure 2.14 and Figure 2.15 shows that the difference is not significant.

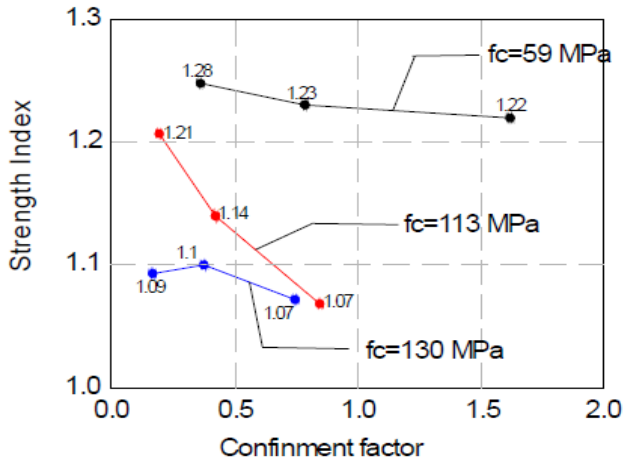

Figure 2.14 Relation between strength index and confinement factor obtained in experimental tests of circular sections described in [4] (adapted form [4])

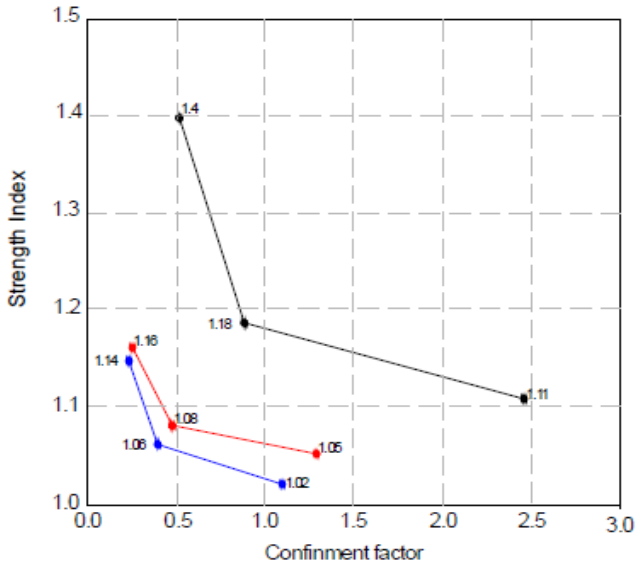

Figure 2.15 Relation between strength index and confinement factor obtained in experimental tests of square sections described in [4] (adapted from [4])

The higher values of strength index as a function of the confinement factor were obtained in specimens tested with epoxy layers in the ends [56]. In this particular case, in which high compressive strength concrete was used, the increase of the confinement factor corresponds to an increase in the strength index as shown in Figure 2.16, then it is possible to suppose that the ends with epoxy layer had a favorable contribution, by an influence on the failure mode.

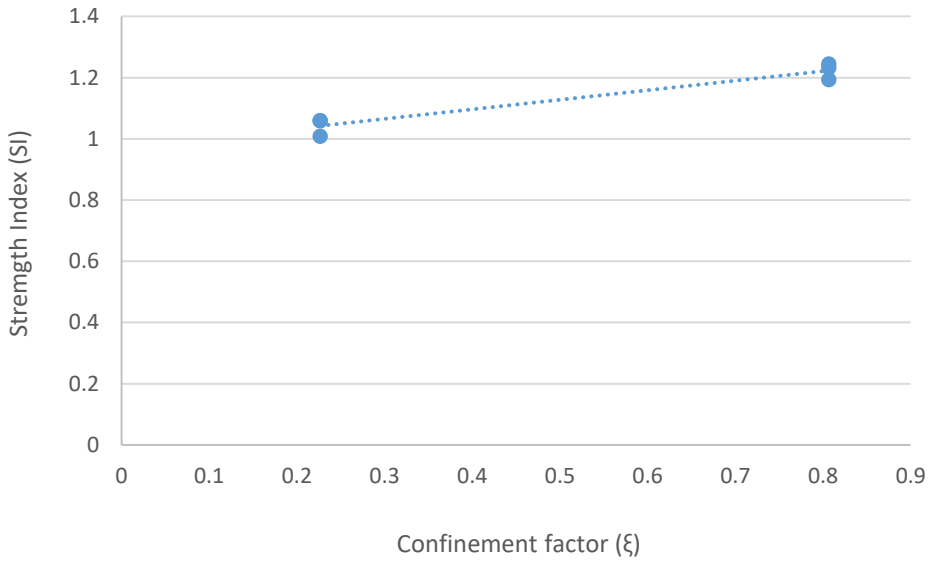

Figure 2.16 Relation between the confinement factor and the strength from results of [56] using an epoxy layer in the ends of the tested circular specimens.

The main factors that affect the failure modes of CFST columns are slenderness, concrete strength and cross-sectional shape [59]. CFST columns with normal concrete often fail due to radial expansion of the infilled concrete, which results in an outward local buckling. Contrarily, when the slenderness ratio is higher, CFST columns fail due to buckling or "shear" [59]–[61].

According to [4], the obtained failure modes for circular UHSCFSTs vary as a function of the confinement factor. Three types of failure modes were observed: a) shear plane and crack, b) only shear plane (Figure 2.17), and c) failure with multiple bulges (Figure 2.18). The change from a) to c) is related to the increase of the confinement factor. The same type of failure with a formation of inclined shear planes was observed in other researches [53] [59].

Failure of UHSCFST elements in an inclined plane seems to be a relevant observation that should be carefully analyzed. Typical failure of unconfined high strength brittle materials, as high strength concrete, does not typically occur in inclined planes, but with a formation of mini-pillars resultant from the significant progression of some long cracks [62]–[64]. Thus, the change of the concrete failure mode, which determines the CFST failure mode, seems to be an effect of the external steel tube. That change may have an influence on the loading capacity and in the efficiency of CFST solutions.

Under compression loads, the concrete core will be cracked. According to [65], the cracked specimen should be considered as a complex structural system, composed of micro-pillars between the cracks. Thus, failure in inclined plane, typically referred as shear failure, is in fact the result of global instability of the system of micro-pillars, as shown in Figure 2.17.

The result is the inclined failure plane, generally associated with shear, but in fact, shear is not present in the process. Failure mode (c), associated with higher confinement factor, is related to the higher capacity of the steel tube to prevent the global instability of the system of micro-pillars, which permits to concentrate the damage near the faces of the tubes, resulting in the formation of the bulges (Figure 2.18).

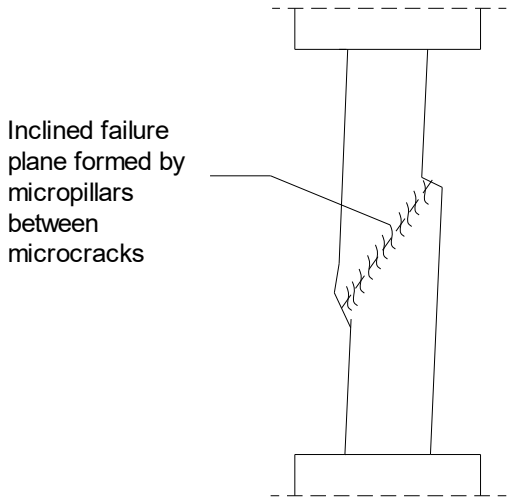

Figure 2.17 Apparent shear failure by instability of micropillars formed between microcracks (based on [53],with relation L/D=5).

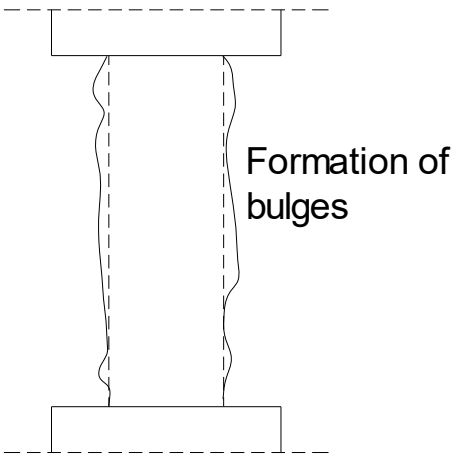

Figure 2.18 Schematic mode of failure with formation of bulges due to transversal pressure of the internal cracked concrete (based on [4], for relation L/D=3).

2.4 Analysis of CFST mechanical behaviour

2.4.1 General analysis

Analyzing the interaction between the concrete core and the steel tube is a fundamental issue to understand the mechanical behaviour of CFST elements. According to [42], [66]–[68], for CFST columns under uniform and concentric load, the steel tube does not provide confinement on the concrete core in the initial phase of loading. In this phase, the concrete core and the steel tube bear the load with minimum interaction. When the micro-cracking of concrete occurs and the lateral expansion of the concrete gradually increases, the concrete effectively mobilizes the steel tube. The interactive contact between the concrete and steel develops bond stresses, and hoop tension in the tube, which tends to prevent the concrete lateral expansion. In this phase, the concrete is considered to be in a tri-axial stress state and the steel tube is subjected to a bi-axial stress state, and both concrete core and steel tube bear the load together, as shown in Figure 2.19.

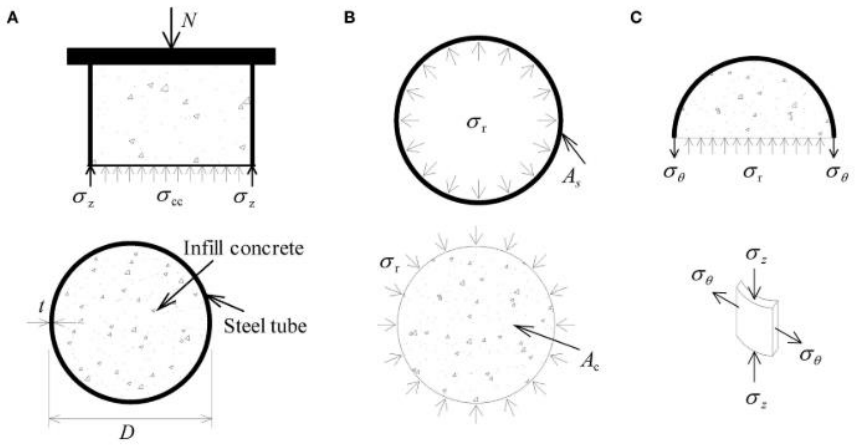

Figure 2.19 Stress state: (A) axial direction; (B) steel tube and infill concrete; (C) free body diagram (adapted from [69])

The confinement effect in load capacity increasing depends on some factors such as the slenderness, concrete type and loading condition. According to [52], confinement effect decreases with the increase of L/D ratio, in which the column fails by buckling before the internal destruction of concrete, with lateral expansion, attains a sufficient level to mobilize the lateral action of the steel tube.

The type of concrete may affect the point at which the confinement starts. This is attributed to the different behaviour between low and high strength concrete under compressive loading, in terms of failure mechanism and deformability. According to [70], the concrete compaction and the corresponding deformability affect its behaviour, this may also have an influence on the interaction between the concrete infill and the steel tube in CFST solutions.

According to [60] and [70], the post-peak strength decrease is lower when the confinement factor increases, which corresponds to higher ductility. Additionally, the post-peak strength decrease is also lower when using low strength concrete than that of high strength concrete. CFST columns show elasto-plastic post-peak behaviour, with strain-hardening when the tubes are filled with normal concrete, and with strain-softening when using high strength concrete, considering a constant confinement factor [53].

The load transfer between the concrete core and the steel tube depends on the bond strength between them. According to [71], the bond strength depends on various factors such as concrete type and cross-sectional size. The bond strength is related to the concrete age and the roughness of the steel-concrete interface. Rusting of steel in the interfacial contact enhances the mechanical bonding owing to the existence of micro-irregularities. The bond strength increases over time, to reach after five years around two and a half times the strength at the age of one year, based on an experimental study performed by [72]. Additionally, bond strength may decrease with the increase of diameter and diameter-to-thickness ratio.

As reported by [73], when the load is applied on the concrete core and the steel tube simultaneously, the bond strength does not affect the behaviour of CFST members. Contrarily, when the concrete core is loaded only, the bond strength has an influence on the confinement effect, affecting the mechanical behaviour of CFST member.

High strength concrete exhibits higher shrinkage properties than normal strength concrete, which may result in weaker bond stresses.

Higher bond stresses are developed in circular high strength CFST than square and rectangular sections [48]. However, the confinement effect is not significantly higher in circular sections as expected.

2.4.2 Analysis of the internal mechanical behaviour

In brittle materials such as high strength concrete, the internal process of destruction is a result of crack formation and its progression, aligned with the principle compressive stresses [62]. The process of cracking results in a structural system of micro-pillars or mini-pillars whose collapse corresponds to the failure of the material [64]. Therefore, failure modes and loading capacity are related to the processes of formation and progression of cracks.

According to [65], the progression of cracks is related to relative displacement between their irregular faces, which induces tension forces in the tips and compression forces in the middle (Figure 2.20). In the case of CFST elements, those compression forces are transferred to the tube, which works as a brace element. Thus, the effect of the steel tube

can be understood as passive confinement, more effective in the prevention of progression of cracks, rather than in preventing their formation.

The difference between confined and unconfined conditions does not have a significant influence on the stress level related to the crack initiation process [74]. The transversal confinement is more effective in the prevention of formed crack progression. When expansive agents are used, the crack initiation is delayed, and consequently the internal destruction processes, which results in higher values of the strength index.

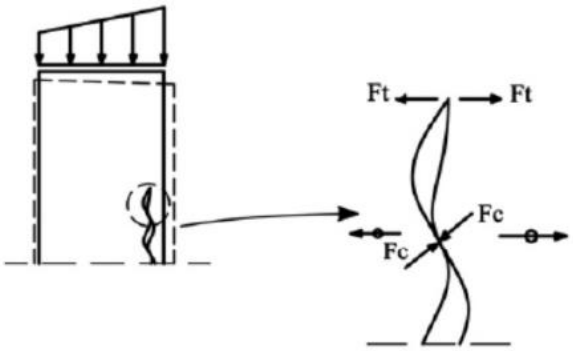

Figure 2.20 Increasing of the crack gap due to the relative displacement of the fitted irregular faces (Fc—force normal to the irregularities in contact; Ft—tension force at the tips) (adapted from [65])

Roughness and friction of the crack faces can be different if the progression of the crack occurs through the grains or mainly in their border. Due to the dense and fine composition of high strength concrete, and the higher matrix strength, the cracks will progress through the grains, making their faces more smooth. Contrarily, in normal strength concrete, the cracks are formed mainly in the borders of the grains, making the crack faces more rough. Thus, the differences of the behaviour between high strength and low strength concrete are possibly related with the crack length and the level of lateral pressure generated in the cracks faces, which have an influence on the crack pattern (Figure 2.21), and consequently, on the failure mode and loading capacity. This fact justifies why failure of CFST elements using normal strength concrete typically occurs with outward local buckling. The more irregular faces of the cracks imply more lateral pressure on the steel tube, contributing to that type of failure.

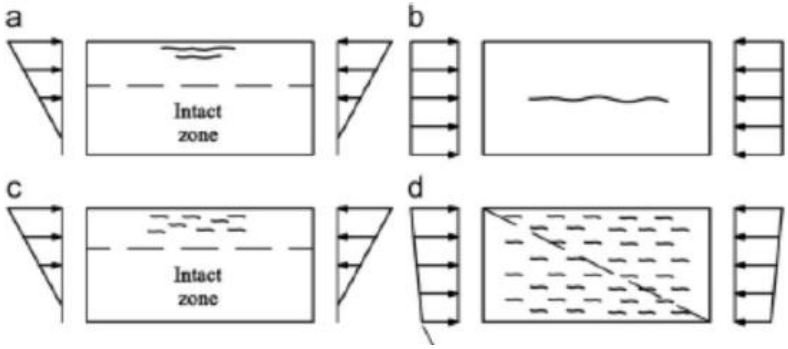

Figure 2.21 Crack pattern for different distribution of the compression forces; (a) and (b) High strength brittle material; (c) and (d) Low strength brittle material (adapted from [64])

The explanation of failure in inclined planes, mainly when high strength concrete is used, is not so clear, especially because this type of failure is not typical for brittle high strength materials, in which the failure results in instability of the formed mini-pillars (Figure 2.22) [65].

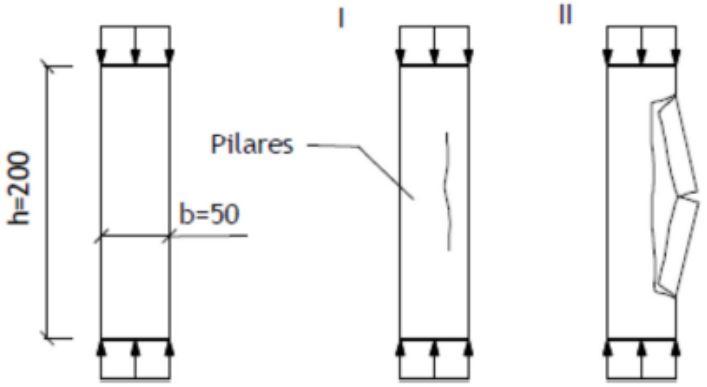

Figure 2.22 Failure of a granite prism (h/b=4); I – Progression of an axial microcrack; II – Buckling of the formed mini-pillar (adapted from [65])

Failure in inclined planes occurs when the internal damage of the material corresponds to a big number of microcracks, which happens when the progression of cracks is limited (Figure 2.23).

According to [75], the progression of cracks produces some confinement in the adjacent zones, preventing the formation of other cracks. If some cracks progress in a significant way, that confinement effect is more global and the number of cracks is smaller (Figure 2.24). Otherwise, if the progression of the cracks is limited, the confinement effect is localized and the number of cracks is higher (Figure 2.23). Thus, failure of CFST elements by instability in an inclined plane means that the number of cracks is high, but their progression is limited, possibly due to the effect of the steel tube. The steel tube seems to be efficient to

prevent the crack progression, but not to avoid the formation of cracks, although they can occur at relatively higher compressive loadings.

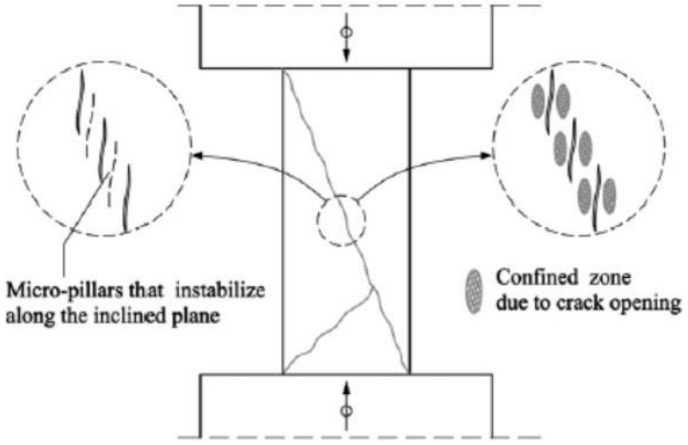

Figure 2.23 Failure by global deformation and simultaneous instability of micro-pillars forming inclined "sliding" planes (adapted from [65])

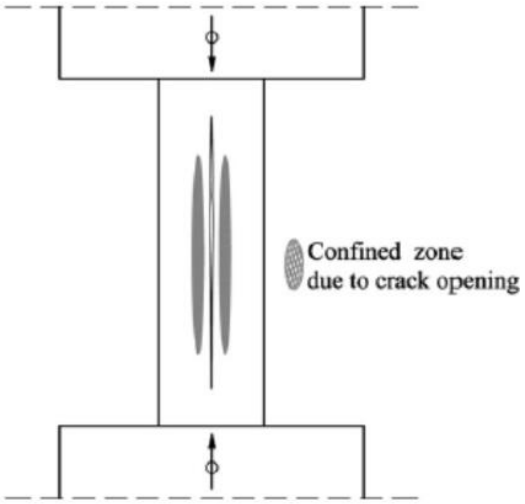

Figure 2.24 Progression of a long crack inhibiting adjacent cracks (adapted from [65])

According to [64], [75], it is possible to have failure of high strength brittle materials under compressive loadings lower than the correspondent to failure loads of conventional compression tests, with failure occurring with the formation of inclined planes of collapse, even in unconfined condition. Those cases occur when the applied loading is higher than the limit of formation of new cracks and lower than the limit for significant progression. The inclined plane forms if the compressive loading is applied very slowly or if it is applied in a cyclic way. Because failure can occur to applied loads close to 50-60% of the conventional compressive strength, the higher number of small cracks is a more unfavorable condition than the formation of a small number of long cracks. Thus, in high compressive strength concrete, the passive confinement of the steel tube, which permits a big number of cracks with limited progression, can produce an undesirable effect, affecting the compressive

strength of the concrete core. In low strength materials, the intrinsic properties of the material do not permit a significant progression of cracks, being the effects of the referred special loading conditions less relevant. In this type of materials, the special loading conditions do not contribute to a change to a less favorable failure mode, as occurs in high strength concrete.

The statements presented above seem to be the reason why the strength index values are not so higher than one when high strength concrete is used in CFST elements. Increasing the confinement factor, which does not correspond to higher active confinement, can imply more limited crack progression and a higher number of cracks, contributing to a less favorable mode of failure.

The positive effect of the steel tube is not exactly the confinement of concrete but a bracing effect on the system of micro-pillars. This may also explain why circular sections do not demonstrate a significantly higher strength index when comparing to square and rectangular sections as expected, due to the theoretically higher confinement effect of circular sections. The theoretically higher confinement of circular sections seems to be insufficient to prevent the formation of cracks, avoiding only their progression. Thus, the number of cracks is higher, and the core concrete is globally more damaged than with square or rectangular tubes. The theoretically lower confinement in square and rectangular sections permits more progression of cracks, leading to more internal confined zones (Figure 2.24) and a more intact concrete core.

2.5 Time-dependent behaviour

In the construction of CFST arch bridges, the steel hollow arch is erected first and the concrete is then filled into the tube. Therefore, the steel tube will support the load prior to the concrete core, which may initially lead to high stresses in the steel tube and low stresses in the concrete core. This difference in loading ages has a significant influence on the time-dependent behaviour of CFST arch bridges [10] [76].

The time-dependent structural behaviour of CFST arches under a sustained loading is related to creep and shrinkage of the concrete core [10]. The creep and shrinkage of the concrete core may increase the time-dependent deformations of CFST structures, causing additional deformations in the arch ribs. Thus, this can be significant in long span CFST arch bridges, as the demands of the serviceability limit state can be fulfilled in the short-term, but due to concrete creep and shrinkage, the structure may undergo excessive deformations under a sustained load, which may violate the requirements of the serviceability limit states. Additionally, the equilibrium configuration may undergo time-dependent alterations due to concrete creep. As a result, the CFST arch may experience

buckling under long term sustained loads, although those loads are lower than the critical buckling loads, in short term analysis [77].

The concrete creep causes a redistribution of stresses between the concrete core and the steel tube, increasing the stresses in the steel tube and decreasing them in the concrete core [76]. The concrete creep develops faster in the early ages of concrete, with the rate decreasing over time. The creep deformation is linear under a small load. With a large load, the deformation may become nonlinear. The main factors affecting the creep behavior of the concrete core in CFST structures are the elastic modulus ratio between the concrete and steel, grade of concrete, stress level, loading age, steel ratio in the cross-sectional area, slenderness ratio of the member and load eccentricity [76], [78]. The creep is considered to be lower in multiaxial stress state than in uniaxial stress. Due to the confinement effect, the concrete core in CFST members seems to be in a triaxial stress state. Thus, concrete creep is considered to be smaller in CFST members than in case of plain concrete. However, some researchers suggest that the concrete core in CFST sections can have confinement effect only under large compression stresses. Hence, the confinement effect on concrete creep behaviour is usually ignored [78].

According to [79], the creep of high strength concrete is lower compared to that of normal strength concrete. The same happens when the concrete is filled into the steel tubes, where the creep coefficient is generally below in high strength CFST than that of normal strength CFST [80].

The creep analysis is important for the design and construction of long-span CFST arch bridges. It is necessary to have an accurate model for predicting the concrete creep effect over time. Several creep and shrinkage models have been proposed [81]–[84]. However, these models have been mainly applied to normal strength concrete. Instead, other models were developed to include the application of high strength concrete, including *fib Model Code for Concrete Structures 2010* [85] and *B4 model* [86]. Fib Model Code for Concrete Structures 2010 model, based on the age-adjusted effective modulus method (AAEM), has been proved to have accurate predictions when applied to long span CFST arches and thus have been used in several researches [23], [87], [88]. The age-adjusted effective modulus method (AAEM) as described in FIB 2010 [85], will be used in the present work to predict the creep behaviour of the concrete. The procedure of the model is described in Appendix A.

Chapter 3 Structural analysis of CFST arch bridge

3.1 Bridge description

The bridge under study is a railway CFST arch bridge with a main span of 400 m and a rise of 100 m so that rise to span ratio is 1/4 (Figure 3.1). The axis of the arch is a parabolic curve. The height of the arch section is variable, with 14.88 m in the arch spring and 10.66 m at the crown. The same occurs in the width, varying between 43.60 m and 13.62 m. The arch is composed of two ribs connected by steel tubes. The bridge solutions were analyzed for two types of ribs, namely with two or four tubes (Figure 3.2 and Figure 3.3), with details described in sections 3.4.1 and 3.5.1.

The bridge deck is a prestressed concrete box section, with 4 m height and 14 m width (Figure 3.4). The braces are formed with transverse hollow steel tubes (with the diameter and thickness of 800 mm and 25 mm, respectively) and diagonal members (with hollow tubes with diameter and thickness of 900 mm and 25 mm, respectively).

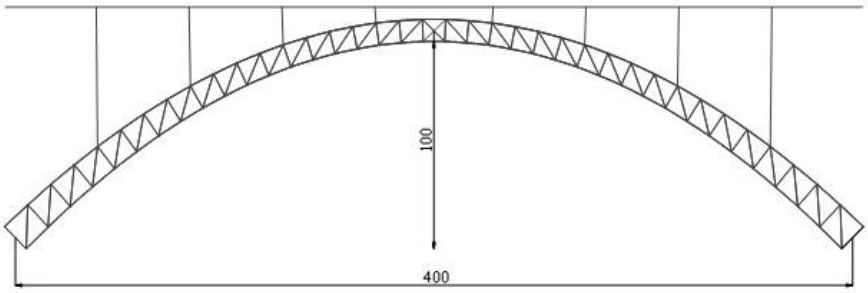

Figure 3.1 A profile view of the bridge (units in m)

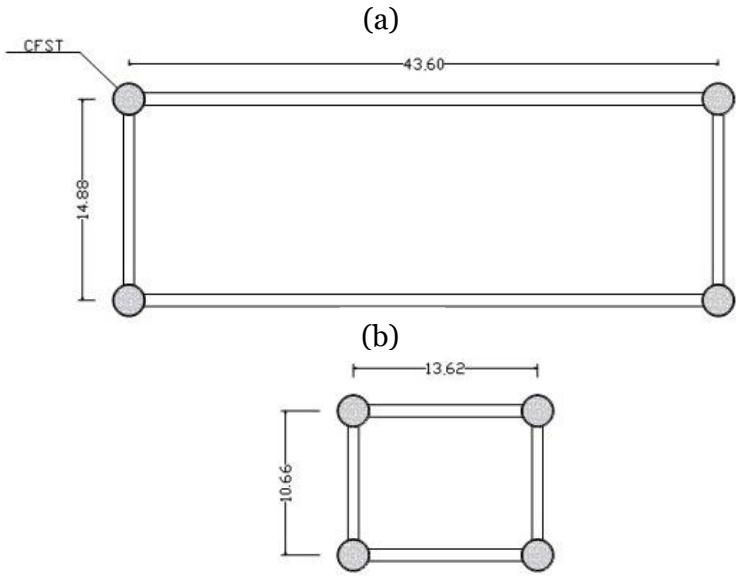

Figure 3.2 Two-tubes rib solution. a) Arch springing b) arch crown (Units in m)

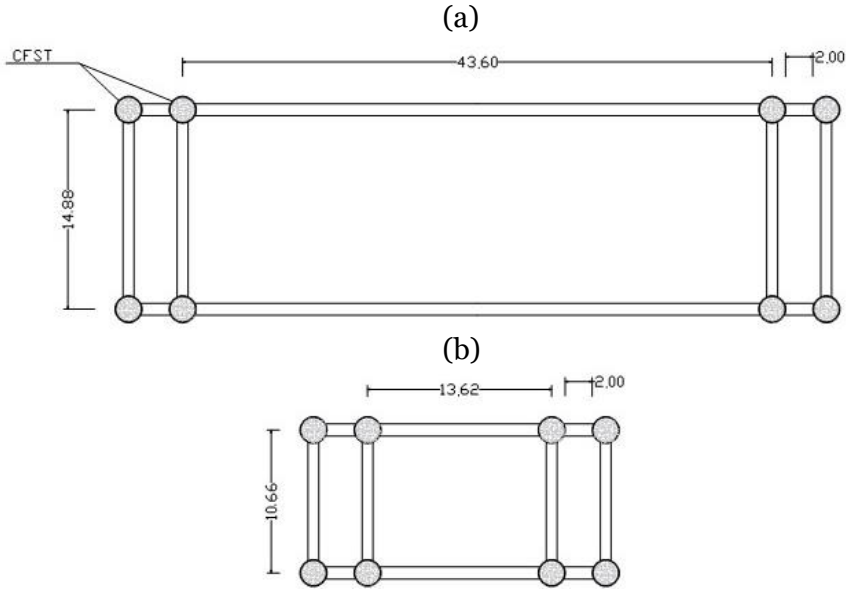

Figure 3.3 Truss rib solution. a) Arch springing b) arch crown (Units in m)

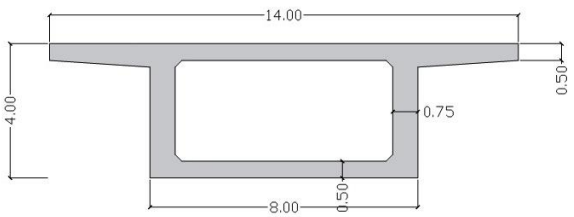

Figure 3.4 Deck section (Units in m)

3.2 CFST materials properties

According to the objectives of the present work, combinations of high strength and low strength materials were considered for the CFST sections. An ultra-high-strength concrete solution (f_{ck}=160 MPA) is compared to a normal strength concrete solution (f_{ck}=60 MPa). According to [3], high strength concrete in CFST sections should be combined with S355 steel or greater grade. According to [2], combining lower strength concrete with lower strength steel is appropriate in the design of CFST section. Therefore, two combinations of materials were studied, the first one is a combination of structural steel with a class of S460 for the tube, filled with concrete C60. The second one is a S700 steel tube filled with concrete C160, since a S700 steel makes the best match to C160 concrete [30].

The concrete properties are described in Table 3.1, where f_{ck} is the characteristic value of compressive strength, f_{cd} is the design value of compressive strength, f_{cm} is the mean value of compressive strength and E_c is the modulus of elasticity.

The modulus of elasticity of concrete was calculated on the basis of FIB 2010 [85] from:

$$E_{ci} = E_{c0}\ \alpha_E \left(\frac{f_{cm}}{10}\right)^{1/3} \tag{3.1}$$

Where:

E_{ci} is the modulus of elasticity at the concrete age of 28.

f_{cm} mean value of compressive strength of concrete

E_{co} =21.5 ·10³ MPa;

α_E taken as 1.

The steel properties are described in Table 3.2, where f_y is yield strength of steel, f_{yd} is the design yield strength and E_s is the modulus of elasticity.

Table 3.1 concrete properties

Concrete class	f_{ck} (MPa)	f_{cd} (MPa)	f_{cm} (MPa)	E_c (GPa)	Weight density (KN/m³)
C60	60.00	40.00	68.00	40.73	25.00
C160	160.00	106.67	168.00	55.06	25.00

Table 3.2 Steel properties

Steel class	f_y (MPa)	f_{yd} (MPa)	E_s (GPa)	Weight density (KN/m³)
S460	460	400	210	77
S700	700	609	210	77

3.3 Actions

The permanent actions defined for the bridge analysis correspond to the structure self-weight and a ballast layer with a distributed load equal to 100 kN/m. Live loads were defined based on EN1991-2 [89], adopting load model LM71 (Figure 3.5), placed in the most unfavorable positions and considering two tracks loaded simultaneously.

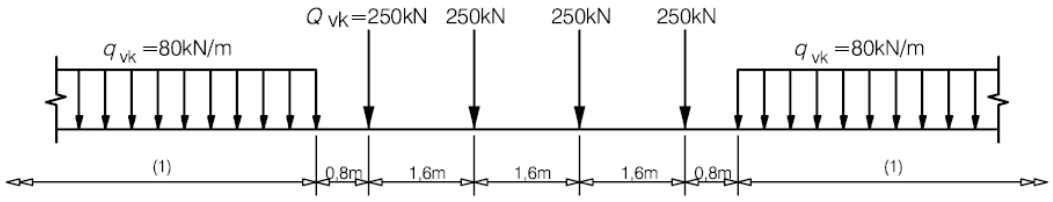

Figure 3.5 Model LM-71 (adapted from [89]).

In addition to the traffic load, a temperature variation corresponding to an overall cooling of -35ºC was considered, taking into consideration that this type of bridge is suitable for mountainous areas, aiming to simulate a very demanding scenario.

The wind action on the structure was calculated according to EN 1991-1-4 [90]. The determination of wind forces is described in Appendix B. Table 3.3 shows the values of the wind forces acting on the deck, columns and on the arch tubes.

Table 3.3 Wind forces on the bridge

Segment	F_w (KN/m)
Deck	15.96
Columns	1.60
Arch tube	12.44

The combinations of actions in Ultimate Limit States (ULS) considered the self-weight of the structure, traffic load, wind action and temperature variation, according to EN1990-Annex 2 [91]. The combination ULS1 considers all the previous loads. The combination ULS2 considers dead loads and load model LM71 for traffic loads. The combination ULS3 considers dead loads and load model LM71 for traffic loads in addition to wind action.

-ULS1 (Ultimate Limit States 1)

$$S_d = \Upsilon_{Gj,sup} G_{kj,sup} + \Upsilon_{Q,1} Q_{k,1} + \Upsilon_{Q,i} \psi_{0.i} T_{k,i} + \Upsilon_{Q,i} \psi_{0.i} F_{w,k} \quad (3.2)$$

$$S_d = 1.35\, G_{kj,sup} + 1.45\, Q_{k,1} + 1.50 \times 0.6\, T_{k,i} + 1.50 \times 0.75\, F_{w,k} \quad (3.3)$$

-ULS2 (Ultimate Limit States 2)

$$S_d = \Upsilon_{Gj,sup} G_{kj,sup} + \Upsilon_{Q,1} Q_{k,1} \quad (3.4)$$

$$S_d = 1.35\ G_{kj,sup} + 1.45\ Q_{k,1} \tag{3.5}$$

-ULS3 (Ultimate Limit States 3)

$$S_d = \Upsilon_{Gj,sup} G_{kj,sup} + \Upsilon_{Q,1} Q_{k,1} + \Upsilon_{Q,i} \psi_{0.i} F_{w,k} \tag{3.6}$$

$$S_d = 1.35\ G_{kj,sup} + 1.45\ Q_{k,1} + 1.50 \times 0.75\ F_{w,k} \tag{3.7}$$

With:

$G_{kj,sup}$ Dead load

$Q_{k,1}$ Load model LM71

$T_{k,i}$ Temperature variation

$F_{w,k}$ Wind action

$\psi_{0,i}$ Recommended values of factors for railway bridges

γ Recommended design values

Regarding Service Limits States (SLS), three combinations were considered. The combinations SLS 1 and SLS 2 with load model LM71 and temperature variation, considering only one loaded track for the verification of deformations, according to [91]. The combination SLS 3 aims to verify the stresses in the steel tubes and considers dead loads, load model LM71 with two loaded tracks, and temperature variation.

SLS 1 (serviceability Limit State 1)

$$S_d = Q_{k,1} + 0.6\ T_{k,i} \tag{3.8}$$

SLS 2 (serviceability Limit State 2)

$$S_d = 0.6\ Q_{k,1} + \ T_{k,i} \tag{3.9}$$

SLS 3 (serviceability Limit State 3)

$$S_d = G_{kj,sup} + \ Q_{k,1} + \ T_{k,i} \tag{3.10}$$

With:

$G_{kj,sup}$ Dead load

$Q_{k,1}$ Load model LM71

$T_{k,i}$ Temperature variation

3.4 Two-tubes rib section

3.4.1 Solution description

In this section the solution of two tubes rib section (Figure 3.2) is analyzed. The cross section of the CFST tubes was defined according to recommendations for the confinement factor (3.11) and the steel ratio (3.12). According to [3] and [32], the confining effect, which improves compressive strength and ductility, is achieved with steel ratio ρ between 8% and

20% for CFST sections and at least 20% for UHSCFST sections. The confinement factor should not be lower than 0.60 [12].

$$\xi = \frac{A_s f_{yd}}{A_c f_{cd}} \tag{3.11}$$

$$\rho = \frac{A_s}{A_c} \tag{3.12}$$

Where:

ξ Confinement factor of CFST.

ρ Sectional steel ratio of CFST.

A_s Sectional area of the steel tube.

A_c Sectional area of the concrete core.

According to EN 1994-1-1 [35], to avoid local buckling, the value of d/t for circular hollow steel sections should not exceed a maximum value given as :

$$max\ (d/t)\ =\ 90\frac{235}{f_y} \tag{3.13}$$

In the solution with the combination of normal strength materials, a CFST section with C60 concrete and S460 steel was used with ϕ2400mm×77mm. In the solution with high strength materials, a section with ϕ1750mm×77mm was used, combining C160 concrete and S700 steel. Table 3.4 and Table 3.5 contain the relevant parameters of the adopted CFST sections.

Table 3.4 CFST sections properties.

Solution	d (cm)	t (cm)	A_c (cm^2)	A_s (cm^2)	$Inertia_{,c}$ (cm^4)	$Inertia_{,s}$ (cm^4)
C60/S460	240.00	7.70	39619.54	5619.40	124913364.59	37946798.57
C160/S700	175.00	7.70	20005.79	4047.03	31849414.05	14189184.35

Table 3.5 d/t relation and steel percentage in CFST sections

Solution	d/t	max (d/t)	ρ (%)	ξ
C60/S460	31.17	45.98	0.14	1.42
C160/S700	22.73	30.21	0.20	1.15

To calculate the bearing capacity of CFST section, the superposition principle was adopted, by adding the bearing capacity of the steel tube and the concrete core, without considering a confining effect.

$$N_{Rd} = A_c f_{cd} + A_s f_{yd} \tag{3.14}$$

Where:

A_c Sectional area of concrete core.

A_s Sectional area of steel tube.

f_{cd} Design value of the compressive strength of concrete

f_{yd} Design value of the yield strength of steel

According to [35], in steel and concrete composite sections, the steel contribution ratio should satisfy the condition $0.2 \leq \delta \leq 0.9$, where δ is defined in (3.15). Table 3.6 contains the axial resistance of the section and the steel contribution ratio.

$$\delta = \frac{A_s f_{yd}}{N_{Rd}} \tag{3.15}$$

Table 3.6 The axial resistance of the section and the steel contribution ratio

Solution	N_{Rd} (MN)	$A_s f_{yd}$ (MN)	δ
C60/S460	383.25	224.78	0.59
C160/S700	459.74	246.34	0.54

3.4.2 Construction phase

The analysis of the construction phase considers only a steel arch, loaded with fresh concrete, ignoring its stiffness. Being a simplified analysis, it does not take into account pouring process sequences, which corresponds to considering all the arch loaded by fresh concrete.

The combination of actions for this phase (3.16) was defined according to [91], taking into consideration the self-weight, wind action and temperature variation.

$$S_d = 1.05\ G_{kj,sup} + 1.50 \times 0.60\ T_{k,i} + 1.50 \times 0.75\ F_{w,k} \tag{3.16}$$

3.4.2.1 Structural analysis

The steel arch was analyzed using Autodesk Robot Structural Analysis 2019 [92], with a three-dimensional bar model (Figure 3.6), with fixed translations in the arch supports.

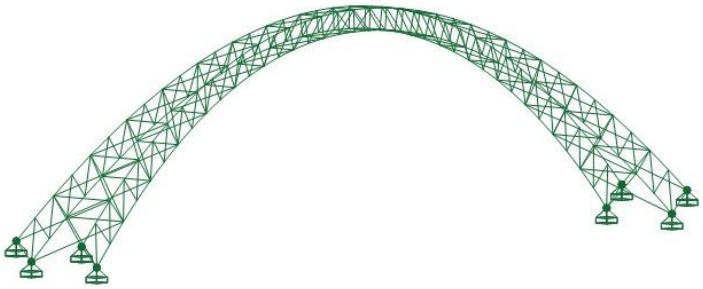

Figure 3.6 Three-dimensional bar model of the steel arch

Linear static analysis was performed. Additionally, a geometrically nonlinear analysis was performed considering different global and local imperfections. The imperfections were modeled based on the buckling mode shapes, namely an out-of-plane local imperfection near the arch base with a value equal to L/350 (Figure 3.7). Additionally, a global imperfection was considered (Figure 3.8) with a value equal to L1/300, with $L1=\sqrt{20L}$, according to EN1993-1-1 [93] and EN1993-2 [94].

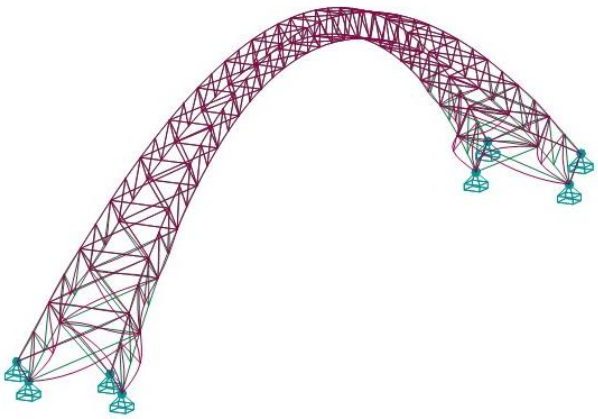

Figure 3.7 Local buckling shape of the arch

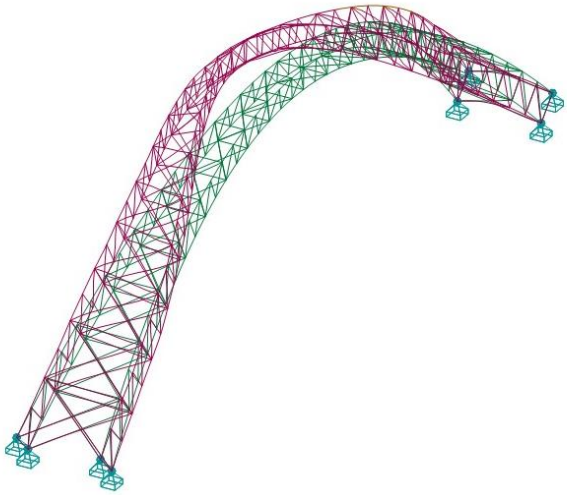

Figure 3.8 Global buckling shape of the arch

Table 3.7 Local and global initial imperfection values e_0 for the steel arch.

	Imperfection e_o (m)
Global	0.30
Local	0.08

The maximum axial forces in the arch occur in the cross sections in arch springing. The maximum axial forces resulting from the combination (3.16) are presented in Table 3.8.

Table 3.8 Maximum axial forces in the steel tube in (MN)

Solution	Linear analysis	Nonlinear analysis
C60/S460	85.412	85.617
C160/S700	60.091	60.287

3.4.2.1.1 Stability structural analysis

The critical buckling distributed load on the arch was obtained by a linear buckling analysis, with the results described in Table 3.9, for the first buckling mode (Figure 3.9 and Figure 3.10). For the C60/S460 combination, the buckling mode is global. Contrarily, for the C160/S700, the buckling mode is local, near to the base of the arch.

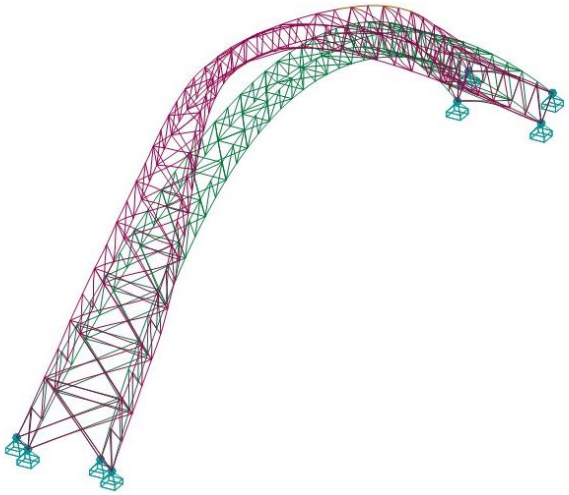

Figure 3.9 First buckling mode of the arch C60/S460 (construction phase)

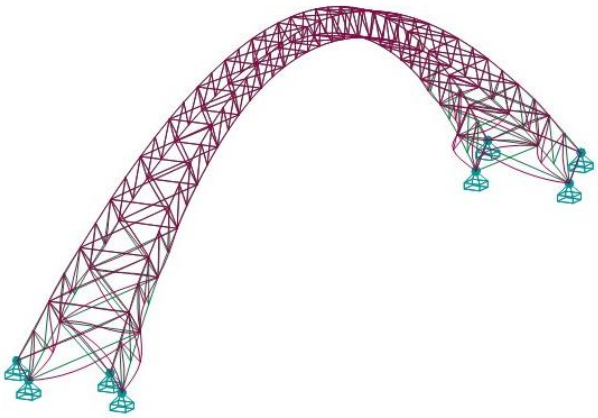

Figure 3.10 First buckling mode of the arch C160/S700 (construction phase)

Table 3.9 The critical distributed load on the arch associated with the first buckling mode (construction phase).

Solution	q_{cr} (KN/m)
C60/S460	2627.02
C160/S700	1141.82

Table 3.10 contains the critical axial force N_{cr}, the slenderness λ as well as the buckling length L_{cr} associated with the first buckling mode of the steel arch, for two conditioning bars with the maximum axial force and the minimum critical force, located in arch springing.

Table 3.10 Critical axial force N_{cr}, the slenderness λ and buckling length L_{cr} associated with the first buckling mode of the arch (construction phase).

Solution	N_{cr} (MN)	λ_y	λ_z	$L_{cr,y}$ (m)	$L_{cr,z}$ (m)
C60/S460	474.82	49.53	49.53	40.70	40.70
	1036.15	33.53	33.53	27.55	27.55
C160/S700	192.28	66.05	66.05	39.11	39.11
	456.52	42.86	42.86	25.38	25.38

3.4.2.2 Resistance check of steel tubes

According to [93], the following condition should be satisfied for members in compression:

$$\frac{N_{Ed}}{N_{b,Rd}} \leq 1{,}0 \tag{3.17}$$

The buckling resistance of the steel tube section was calculated by the following expression:

$$N_{b,Rd} = \chi A_s f_{yd} \tag{3.18}$$

Where χ is the reduction factor for the relevant buckling mode, it is determined as follows:

$$\chi = \frac{1}{\Phi + \sqrt{(\Phi^2 - \bar{\lambda}^2)}} \quad \text{with} \quad \chi \leq 1 \quad \Phi = 0.5[1 + \alpha(\bar{\lambda} - 0.2) + \bar{\lambda}^2] \tag{3.19}$$

The relative slenderness $\bar{\lambda}$ was calculated as:

$$\bar{\lambda} = \sqrt{\frac{Af_y}{N_{cr}}} = \frac{L_{cr}}{i}\frac{1}{\lambda_I} \quad \text{With} \quad \lambda_I = \pi\sqrt{\frac{E}{f_y}} \tag{3.20}$$

Where:

L_{cr} is the buckling length in the buckling plane considered

N_{cr} is the elastic critical force for the relevant buckling mode

i is the radius of gyration about the relevant axis and is given as $i = \sqrt{\frac{I}{A}}$

α is an imperfection factor for buckling curves. (α =0.13 for hollow steel sections which corresponds to buckling curve type a_o).

Table 3.11 contains the results of the axial buckling resistance as well as the design value of the axial force in the tube, for the two conditioning bars. As the results show, the axial buckling resistance is verified for both solutions

Table 3.11 Buckling resistance of the steel tube and the design value of the axial force in the tube.

Solution	$\bar{\lambda}$	i (cm)	λ_I	χ	$N_{b,Rd}$ (MN)	N_{Ed} (MN)
C60/S460	0.74	82.18	67.12	0.88	198.14	45.83
	0.5	82.18	67.12	0.95	213.86	85.62
C160/S700	1.21	59.21	54.41	0.56	138.76	25.74
	0.79	59.21	54.41	0.86	211.69	60.29

3.4.2.2.1 Combined compression and bending moment verification

According to [93], members subjected to combined bending and compression should satisfy the following two equations:

$$\frac{N_{Ed}}{\chi_y \frac{N_{Rk}}{\Upsilon_{M1}}} + k_{yy} \frac{M_{y,Ed}}{\chi_{LT} \frac{M_{y,Rk}}{\Upsilon_{M1}}} + k_{yz} \frac{M_{z,Ed}}{\frac{M_{z,Rk}}{\Upsilon_{M1}}} \leq 1 \quad (3.21)$$

$$\frac{N_{Ed}}{\chi_z \frac{N_{Rk}}{\Upsilon_{M1}}} + k_{zy} \frac{M_{y,Ed}}{\chi_{LT} \frac{M_{y,Rk}}{\Upsilon_{M1}}} + k_{zz} \frac{M_{z,Ed}}{\frac{M_{z,Rk}}{\Upsilon_{M1}}} \leq 1 \quad (3.22)$$

Where:

N_{ed}, $M_{y,Ed}$ and $M_{z,Ed}$ are the design values of the compression force and bending moments

N_{RK} is the characteristic value of the steel section resistance to normal force

$M_{i,Rk}$ is the characteristic moment resistance

χ_y and χ_z are the reduction factors due to flexural buckling

χ_{LT} is the reduction factor due to lateral torsional buckling (taken as 1)

k_{yz}, k_{zy}, k_{yy}, k_{zz} are the interaction factors

Υ_{M1} is a partial factor taken as 1

This verification is applied for two bars with critical combinations of simultaneous axial force and bending moment. The determination of the interaction factors for these bars is described in Appendix C, with the values presented in Table 3.12. The values of N_{ed}, $M_{y,Ed}$, $M_{z,Ed}$, N_{Rk} and $M_{i,Rk}$ are presented in Table 3.13. Both equations verify the condition ≤ 1, for both solutions, as shown in Table 3.14.

Table 3.12 Interaction factors

Solution	K_{yz}	K_{zy}	K_{yy}	K_{zz}
C60/S460	0.90	0.84	0.54	0.50
	0.90	0.93	0.54	0.56
C160/S700	0.90	1.06	0.55	0.65
	1.07	1.11	0.67	0.70

Table 3.13 N_{ed}, $M_{y,Ed}$, $M_{z,Ed}$,N_{Rk} and $M_{i,Rk}$ in the steel arch

Solution	N_{ed} [MN]	$M_{y,Ed}$ [MNm]	$M_{z,Ed}$ [MNm]	N_{Rk} [MN]	$M_{i,Rk}$ [MNm]
C60/S460	85.62	0.45	0.98	258.49	191.21
	51.93	3.04	7.79	258.49	191.21
C160/S700	60.29	0.57	0.64	283.29	150.97
	26.48	0.96	6.24	283.29	150.97

Table 3.14 Combined bending and axial compression verification equations

Solution	Equation (3.21)	Equation (3.22)
C60/S460	0.35	0.40
	0.33	0.39
C160/S700	0.24	0.28
	0.17	0.21

3.4.3 Service phase and ULS design

In this section, the entire bridge under service is analyzed, when the concrete core acts compositely with the steel tube.

3.4.3.1 Structural analysis

The arch bridge solution was analyzed using Robot 2019 [92], with a three-dimensional bar model (Figure 3.11), with fixed translations in the arch supports. The deck was modeled with fixed translations on one side and free displacement in the axial direction on the other.

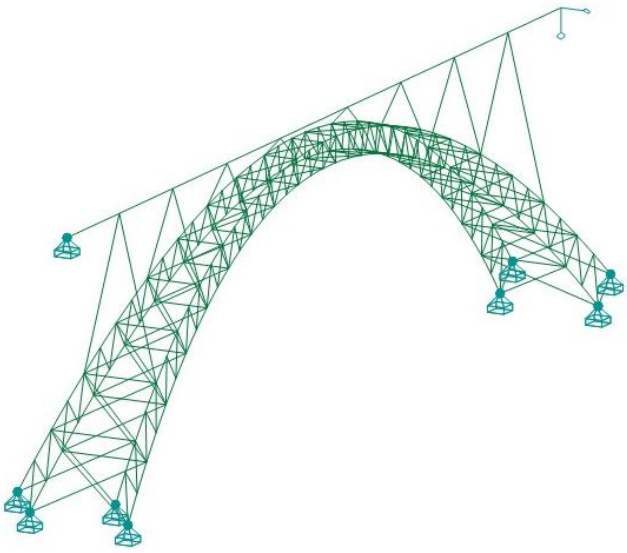

Figure 3.11 three-dimensional bar model of the bridge

The homogenization method was adopted to model the CFST arch sections. The CFST section was modeled with an equivalent concrete section. The properties of the equivalent section are presented in Table 3.15.

Table 3.15 The proprieties of the equivalent CFST sections

Solution	$A_{,eq}$ [cm^2]	$Inertia_{,eq}$ [cm^4]	$Inertia_{x,eq}$ [cm^4]	$E_{,eq}$ [GPa]	W [KN/m]
C60/S460	68590.82	320551270.67	641102541.33	40.73	142.32
C160/S700	35439.87	85962442.34	171924884.68	55.06	81.18

Linear and geometrically nonlinear static analyses were performed. The nonlinear analysis was carried out by inducing the buckling mode shape of the arch to the model as the initial imperfection. Two models were considered, one for an out-of-plane local imperfection near the arch base, with a value of L/300 (Figure 3.12), another one for an in-plane global imperfection with a value of L/600 (Figure 3.13), according to [35] [94].

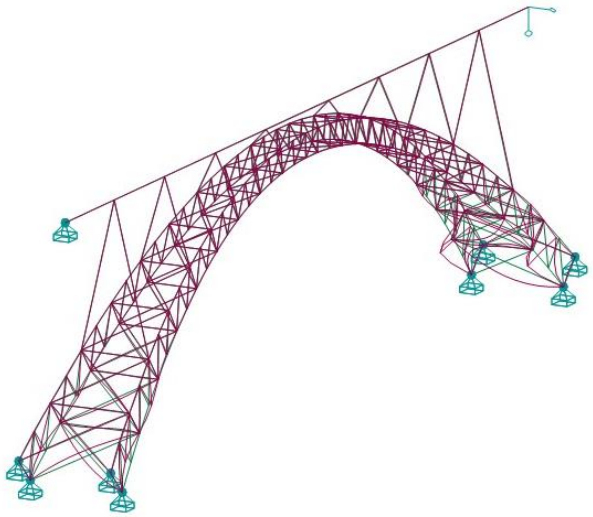

Figure 3.12 Local buckling shape of the arch

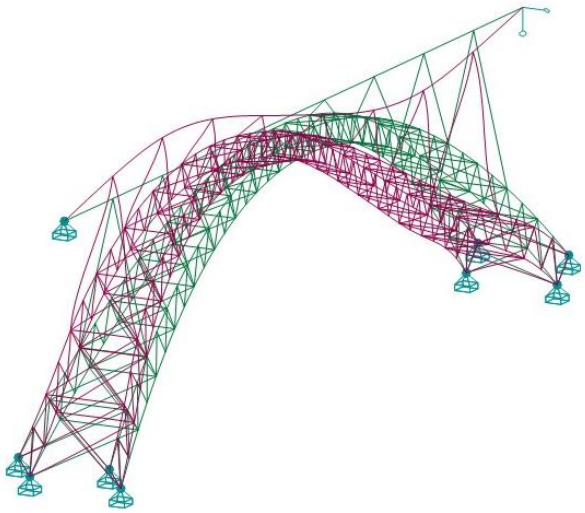

Figure 3.13 Global buckling shape of the arch

Table 3.16 Local and global initial imperfection values e_0.

	Imperfection e_0 (m)
Global	0.66
Local	0.10

The maximum axial force in the arch occurs in the cross section in arch springing, in the left bottom chord. The results of the axial forces of that section for dead load and ultimate limit states combinations are presented in Table 3.17 and Table 3.18 for C60/S460 and C160/S700, respectively. The maximum bending moments occur near the arch crown, with the values listed in Table 3.19.

Table 3.17 Maximum axial forces C60/S460 in (MN)

Analysis type	Dead load	ULS 1	ULS 2	ULS 3
Linear analysis	101.721	194.573	163.831	184.131
Nonlinear analysis	101.935	196.937	165.588	186.452

Table 3.18 Maximum axial forces C160/S700 in (MN)

Analysis type	Dead load	ULS 1	ULS 2	ULS 3
Linear analysis	79.941	165.436	136.014	156.432
Nonlinear analysis	80.127	168.047	137.852	158.853

Table 3.19 Maximum bending moments

Analysis type	Linear analysis		Nonlinear analysis	
Solution	M_y (MNm)	M_z (MNm)	M_y (MNm)	M_z (MNm)
C60/S460	44.858	19.203	45.700	19.526
C160/S700	25.938	9.573	26.480	8.825

3.4.3.1.1 Stability structural analysis

The critical buckling distributed load on the arch was obtained by a linear buckling analysis, with the results described in Table 3.20, for the first buckling mode (Figure 3.14 and Figure 3.15). Figure 3.16 and Figure 3.17 describe the second buckling mode.

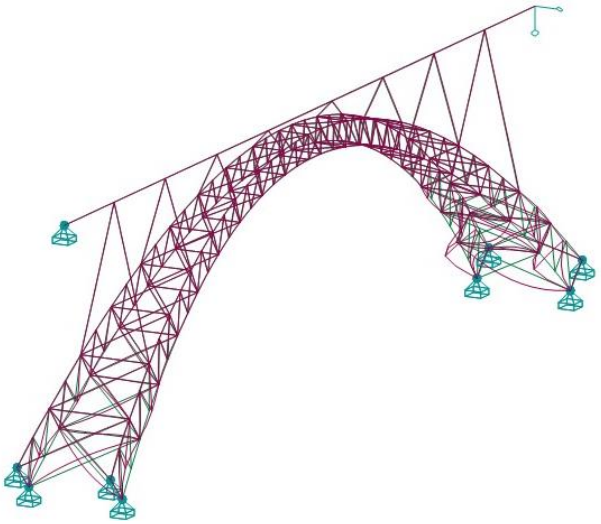

Figure 3.14 First buckling mode of the arch for C60/S460

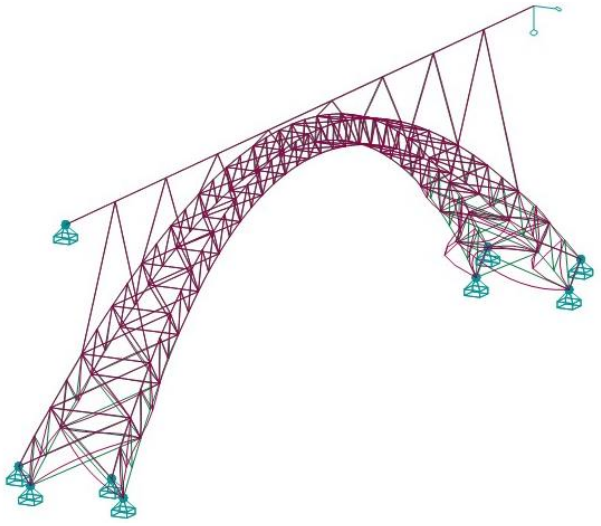

Figure 3.15 First buckling mode of the arch for C160/S700

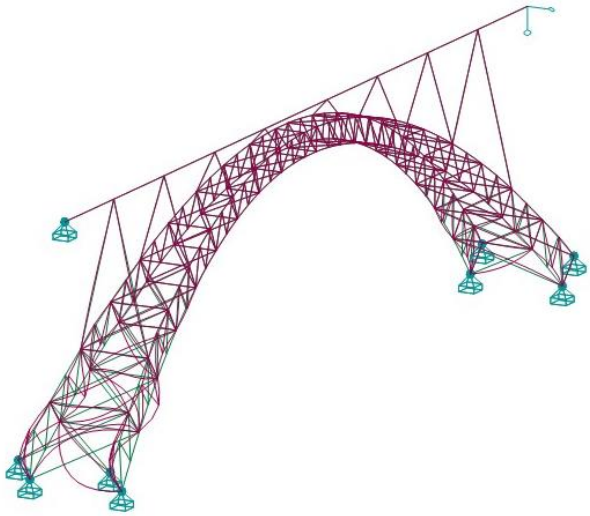

Figure 3.16 Second buckling mode of the arch for C60/S460

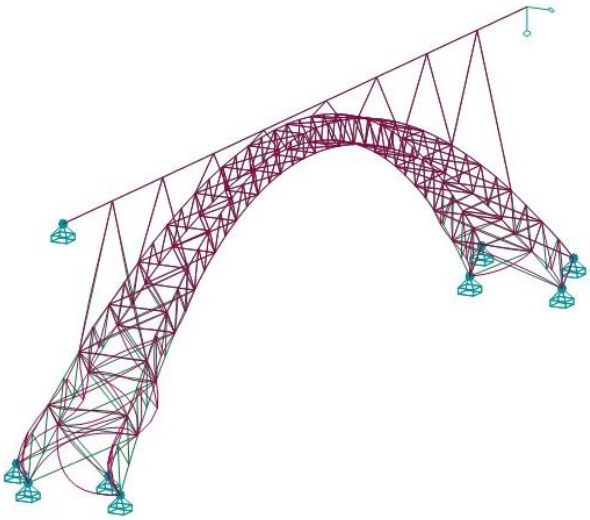

Figure 3.17 Second buckling mode of the arch for C160/S700

Table 3.20 The critical distributed load on the arch associated with the first buckling mode

Solution	q_{cr} (KN/m)
C60/S460	4143.29
C160/S700	1587.46

The critical buckling distributed load on the deck, associated with the arch buckling, was also obtained by a linear buckling analysis, with the values presented in Table 3.21.

The buckling of the arch appears in the 5th buckling mode for C60/S460 as a global in-plane shape (Figure 3.18), where the first 4 buckling modes are associated with the columns, while it happens in the 3rd buckling shape for C160/S700 as a local in-plane shape (Figure 3.19), where the first 2 buckling modes are associated with the columns.

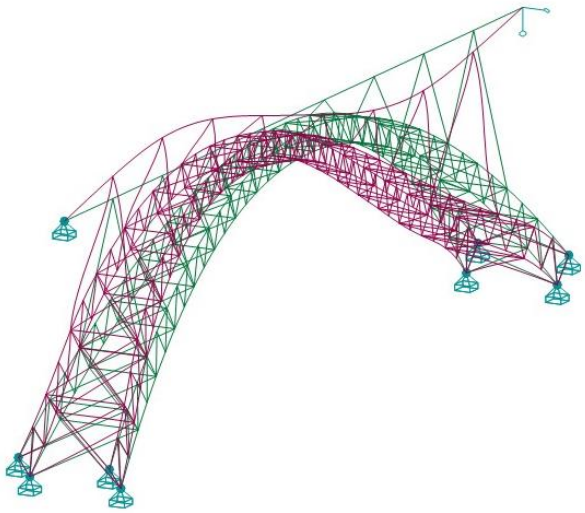

Figure 3.18 Fifth bucking mode of the bridge, the first one associated with the arch C60/S460

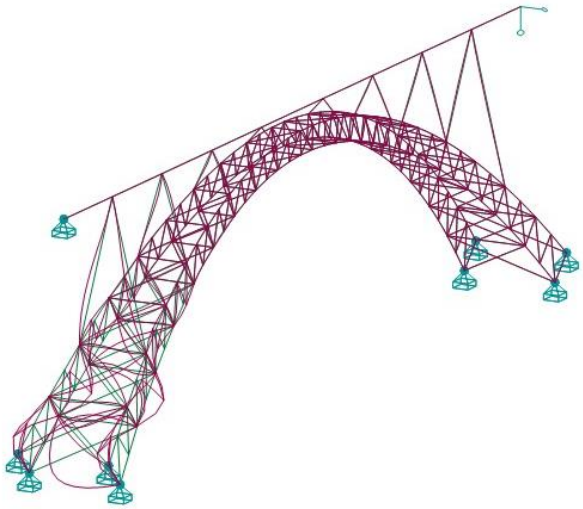

Figure 3.19 Third buckling mode of the bridge, the first one associated with the arch C160/S700

Table 3.21 The critical buckling distributed load on the deck associated with the arch buckling.

Solution	q_{cr} (KN/m)
C60/S460	14184.30
C160/S700	6872.78

Table 3.22 contains the critical axial force N_{cr}, the slenderness λ and the buckling length L_{cr} associated with the first buckling of the arch (Figure 3.18 and Figure 3.19), for two conditioning bars with the maximum axial force and the minimum critical force (one located in arch springing and another in the arch crown).

Table 3.22 Critical axial force N_{cr}, the slenderness λ and the buckling length L_{cr} associated with the first buckling mode of the arch

Solution	N_{cr} (MN)	λ_y	λ_z	$L_{cr,y}$ (m)	$L_{cr,z}$ (m)
C60/S460	1166.04	48.63	48.63	30.54	30.54
	596.51	67.99	67.99	42.70	42.70
C160/S700	583.05	57.48	57.48	26.13	26.13
	259.49	86.15	86.15	39.16	39.16

3.4.3.2 Safety verifications

According to [35], for composite members in axial compression, the buckling resistance should verify the following condition:

$$\frac{N_{Ed}}{\chi\, N_{pl,Rd}} \leq 1.0 \tag{3.23}$$

For the determination of the relative slenderness $\bar{\lambda}$ and the elastic critical force N_{cr}, it was considered a value of effective flexural stiffness $(EI)_{eff}$ of the cross section given by (3.24), where 0.6 is a correction factor as stated in [35].

$$(EI)_{eff} = E_S I_S + 0.6 E_C I_C \tag{3.24}$$

The relative slenderness is then calculated as follows:

$$\bar{\lambda} = \sqrt{\frac{N_{pl,Rk}}{N_{cr}}} \tag{3.25}$$

Where $N_{pl,Rk}$ is the characteristic value of the plastic resistance to compression and N_{cr} is the elastic critical normal force for the relevant buckling mode. The imperfection factor for the buckling curve considered is α =0.21 which corresponds to buckling curve type (a) for CFST sections, according to [35].

The data of the buckling resistance of the two conditioning bars are shown in Table 3.23, in addition to the maximum axial force for ULS combinations, which in this case is the axial force resulting from the combination ULS 1.

Table 3.23 Axial buckling resistance of the CFST tube sections and the axial force due to ULS1 combination

Solution	$\bar{\lambda}$	i (cm)	χ	$N_{b,rd}$ (MN)	N_x (MN)
C60/S460	0.65	62.81	0.87	333.05	196.94
	0.91	62.81	0.73	278.22	82.73
C160/S700	1.02	45.45	0.65	300.44	168.05
	1.52	45.45	0.36	166.48	57.42

As shown in Table 3.23, the axial buckling resistance of the CFST sections to compression is verified.

3.4.3.2.1 Combined compression and bending moment verification

The diagrams of the combined bending moment and compression resistance of the section were obtained using the Interac program [95]. The diagrams are presented in Figure 3.20 for C60/S460 and Figure 3.21 for C160/S700. This verification is applied for two sections with critical combinations of simultaneous axial force and bending moment

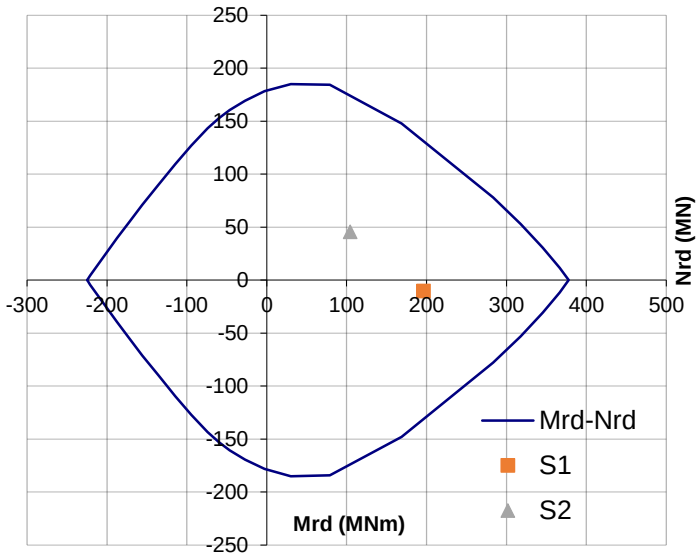

Figure 3.20 Combined bending moment and compression verification for C60/S460.

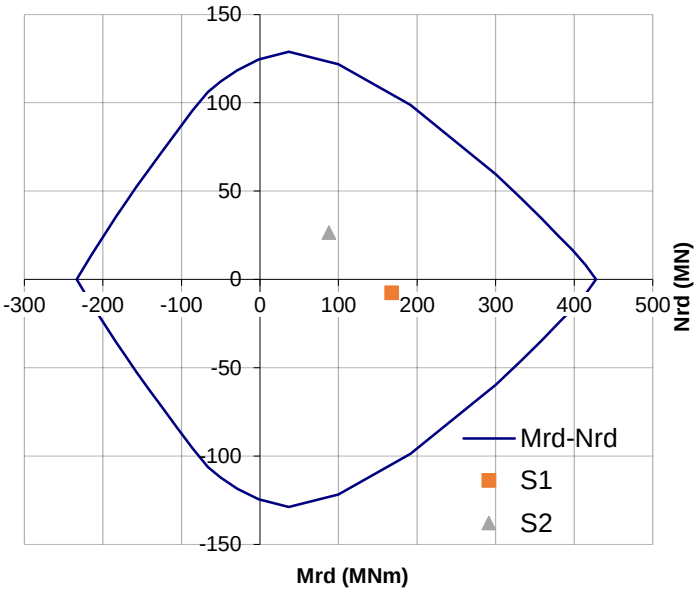

Figure 3.21 Combined bending moment and compression verification for C160/S700

According to [35], the following expression based on the interaction curve should be satisfied:

$$\frac{M_{y,Ed}}{M_{pl,N,Rd}} + \frac{M_{z,Ed}}{M_{pl,N,Rd}} \leq 1.0 \tag{3.26}$$

Where

M_{Ed} is the maximum bending moment.

$M_{pl,N,Rd}$ is the plastic bending resistance taking into account the normal force N_{ed}.

Table 3.24 contains the design values of the bending moments $M_{y,Ed}$ and $M_{z,Ed}$ as well as the plastic bending resistance taking into account the normal force $M_{pl,N,Rd}$.

Table 3.24 $M_{y,Ed}$, $M_{z,Ed}$ and $M_{pl,N,Rd}$.

Solution	$M_{y,Ed}$ (MNm)	$M_{z,Ed}$ (MNm)	$M_{pl,N,Rd}$ (MNm)	$\frac{M_{y,Ed}}{M_{pl,N,Rd}} + \frac{M_{z,Ed}}{M_{pl,N,Rd}}$
C60/S460	45.70	19.53	173	0.38
	44.86	19.20	170	0.38
C160/S700	26.48	8.83	123	0.29
	25.39	9.57	122	0.29

As Table 3.24 shows, the expression (3.26) is satisfied, the combined compression and bending moment resistance is verified for both solutions.

3.4.4 Creep analysis

To take into consideration the time-dependent behavior of the concrete core inside the steel tube, age-adjusted effective modulus (AAEM) procedure from FIB 2010 [85] was adopted. However, in the present work, the performed creep analysis is simplified, without taking into consideration the construction sequence and the different concrete ages concerning the permanent loading application.

The reduction of the modulus of elasticity equivalent to the creep effects corresponds to 54.6 % for C60 and 38.3 % for C160 of their value, after 100 years. The equivalent change of the modulus of elasticity of concrete over time is shown in Figure 3.22. Figure 3.23 shows the change of creep coefficient over time.

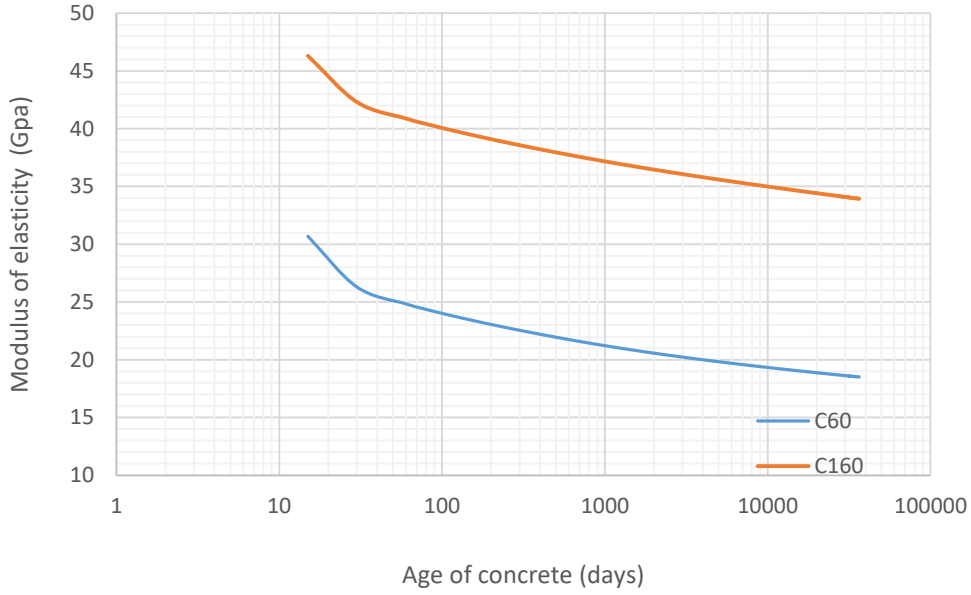

Figure 3.22 The change of the modulus of elasticity of concrete over time

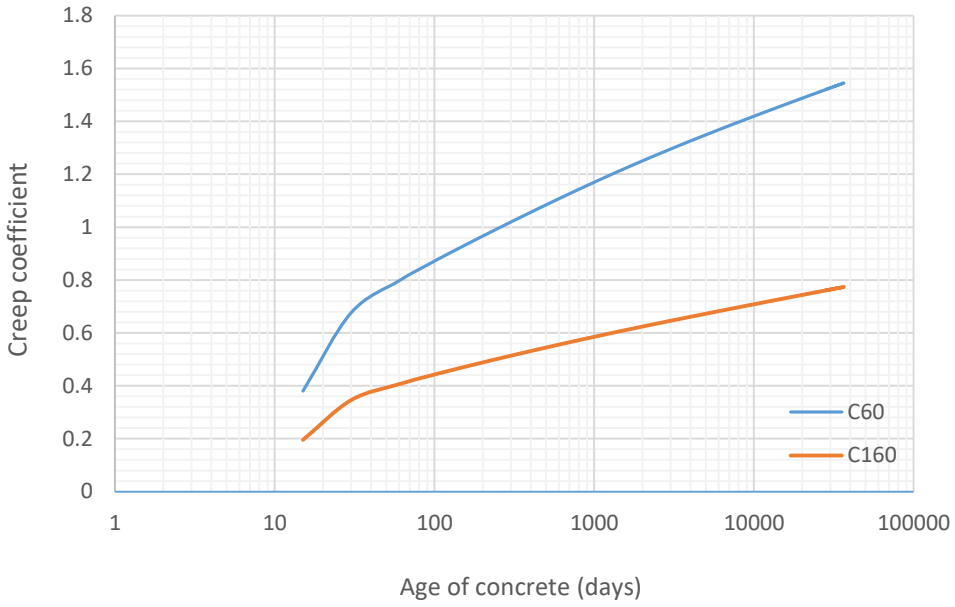

Figure 3.23 The change of creep coefficient over time

3.4.4.1 Long-term deformations

The deformation of the bridge deck increased over time due to concrete creep in the arch tubes. An increase of 4.4 cm of the maximum deflection in the bridge deck was observed for C60 solution, while 3.3 cm for C160 solution. Figure 3.24 and Figure 3.25 show the vertical deflection of the deck for dead load with and without consideration of concrete creep effects.

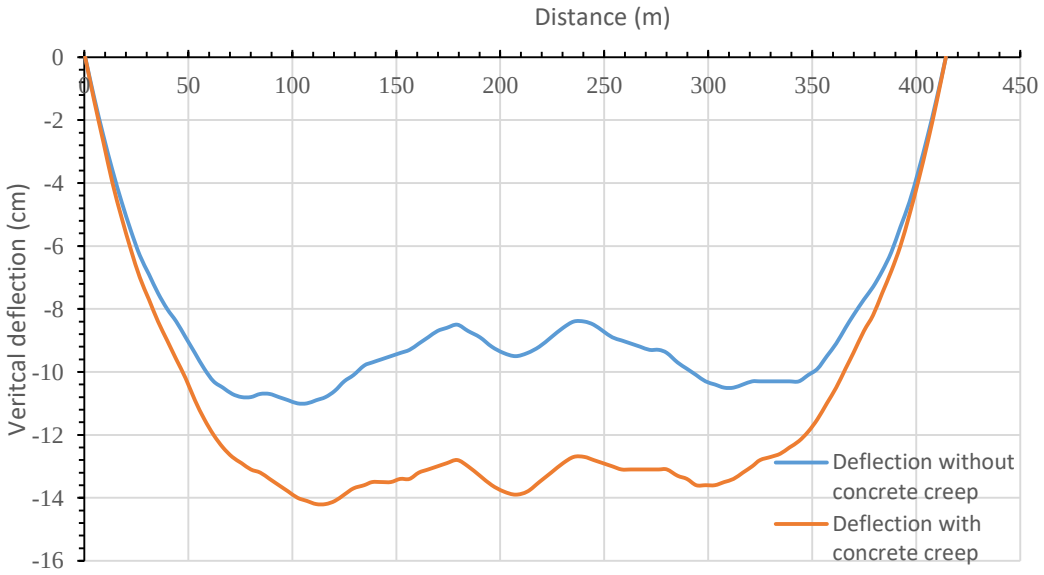

Figure 3.24 Vertical deflection of the deck for C60/S460.

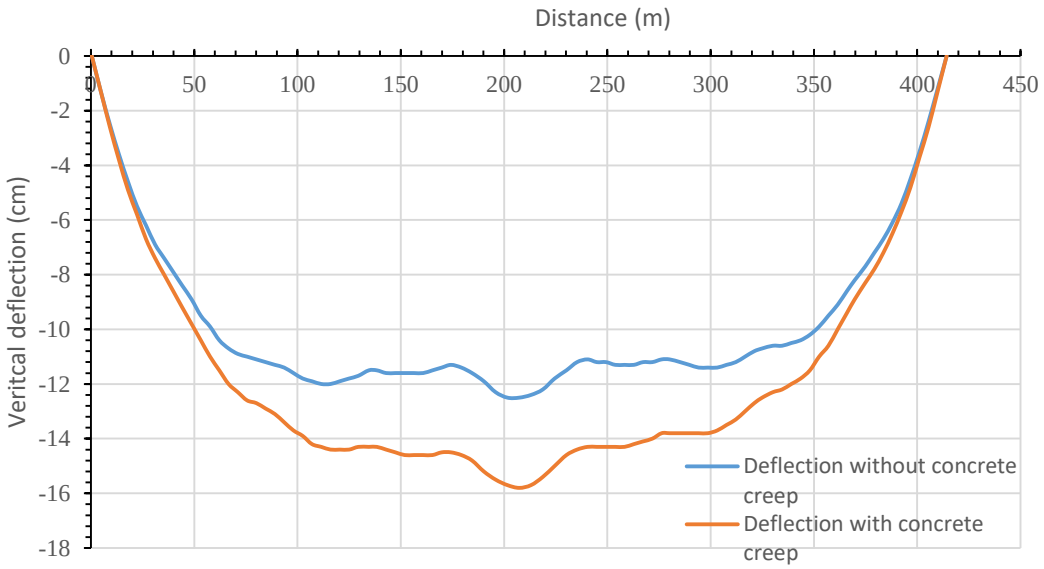

Figure 3.25 Vertical deflection of the deck for C160/S700.

The deformation in the arch tubes also increased because of concrete creep. The vertical deflection of the arch crown due to concrete creep reaches a value of 4.1 cm for C60 solution and a value of 3.1 cm for C160 solution, after 100 years. The creep deformation curve is shown in Figure 3.26, for both solutions.

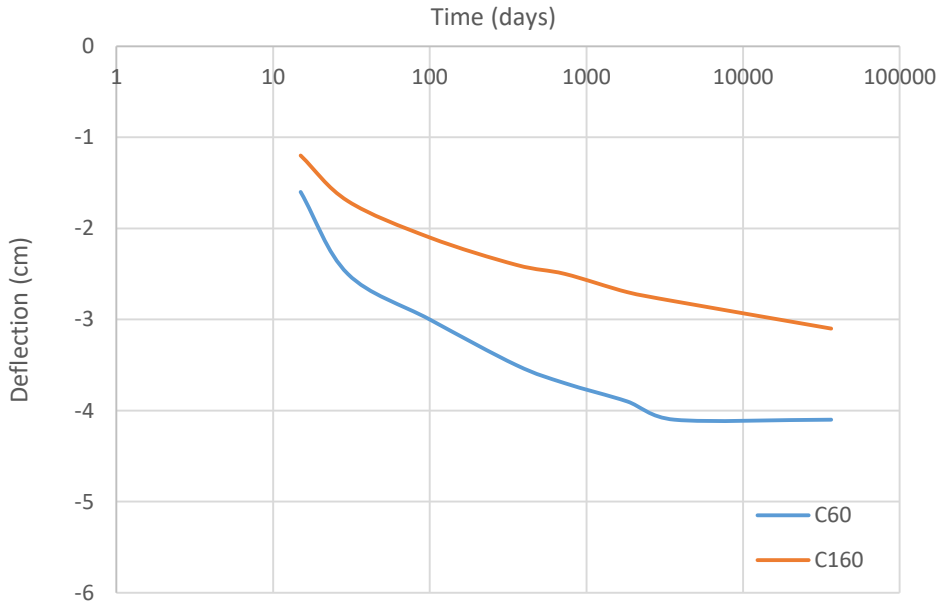

Figure 3.26 Creep deformation curve in arch crown section

3.4.4.2 Stress in steel tube

The stresses in CFST sections are redistributed between the steel tube and the concrete core due to concrete creep. The stresses in the steel tube increase and decrease in the concrete. Figure 3.27 and Figure 3.28 give the stress curves of the steel tube at arch springing section,

which is the section with the maximum forces. It shows that the stress due to dead loads in the steel tube increases with time, to reach 111.9 MPa in C60/S460, and 110.1 MPa in C160/S700 solution, 100 years after construction.

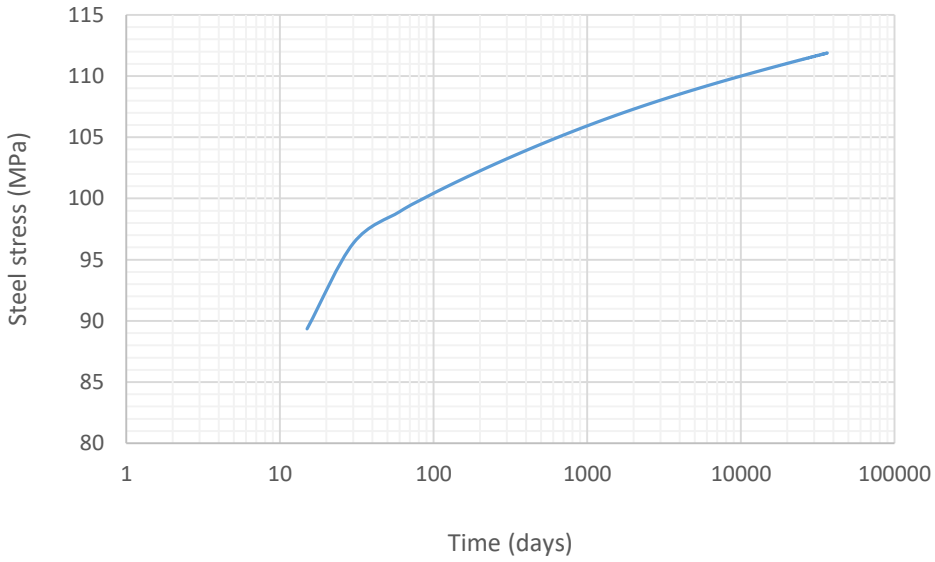

Figure 3.27 Stresses in steel tube due to dead load for C60/S460

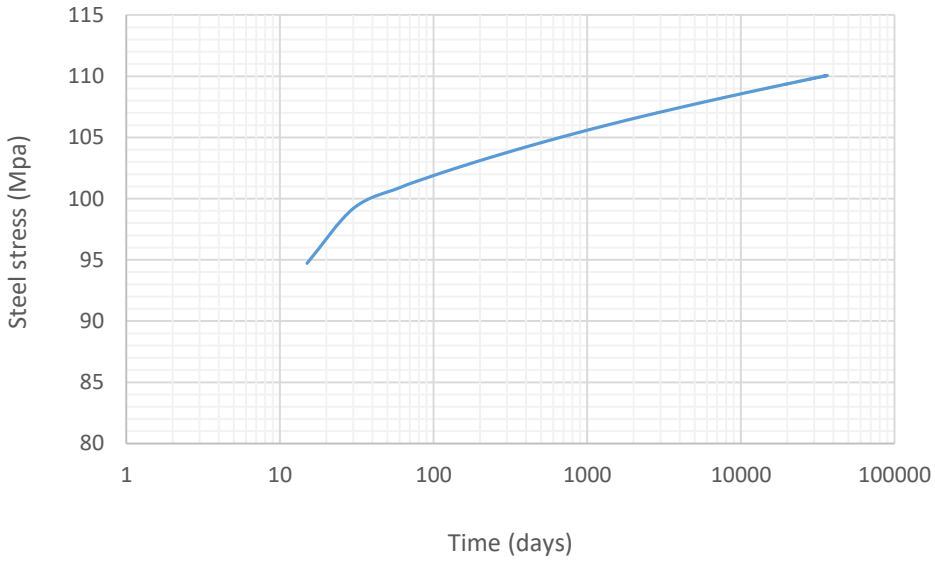

Figure 3.28 Stresses in steel tube due to dead load for C160/S700

The stress increment in arch springing section in C60/S460 and C160/S700 is 35.27 MPa (46.0%) and 23.84 MPa (27.6%), respectively. To check the stresses in the steel tube, the combination SLS 3 (3.10) was considered. The stresses due to combined bending moments and compression in the steel tube were calculated by the following expression:

$$\sigma_x = \frac{N_x}{A_s} + \frac{M_y}{I_y} z + \frac{M_z}{I_z} y \tag{3.27}$$

The verification considered two critical sections. Table 3.25 shows whether the section is subjected to compression only or not, considering that the central core of a circular section is D/8, and the load eccentricity e=M/N. For sections subjected to compression only, the expression (3.28) can be used to estimate the bending moments in the steel tube.

$$M_s = M_{Ed} \frac{E_s I_s}{E_c I_{c+} E_s I_s} \tag{3.28}$$

When the section is subjected to compression and tension, it is necessary to consider a reduction of the concrete bending stiffness, so the following formulae can be used to estimate the bending moments in the steel tube:

$$M_s = M_{Ed} \frac{E_s I_s}{o.6\, E_c I_{c+} E_s I_s} \tag{3.29}$$

Table 3.25 N_x,M_y and M_z due to SLS3

Solution	N_x (MN)	M_y (MNm)	M_z (MNm)	D/8 (cm)	e_y (cm)	e_z (cm)
C60/S460	131.86	0.42	0.59	30.00	0.31	0.45
	76.89	34.07	15.25		44.31	19.84
C160/S700	109.55	0.15	0.58	21.88	0.14	0.53
	64.66	19.61	7.16		30.33	11.08

Adding the stress increments due to concrete creep to the stresses resulting from the combination SLS 3 (3.10), the stresses are still much less than the strength of S460 and S700, as shown in Table 3.26. However, for lower strength steel, the increase of stresses due to creep can have undesirable effects, as described in [88].

Table 3.26 Stress redistribution in the steel tube due to concrete creep

Solution	$\sigma_{s,SLS3}$ (MPa)	$\Delta\sigma_s$ (MPa)	σ_s (MPa)	f_{yd} (MPa)
C60/S460	101.40	35.27	136.67	400.00
	170.55	35.27	205.82	
C160/S700	121.20	23.84	145.04	608.70
	191.60	23.84	215.44	

3.4.4.3 Stress in concrete core

Figure 3.29 and Figure 3.30 give the stress curves of the concrete core at arch springing section. It shows that the stresses due to dead load in the concrete core decrease over time,

to reach 9.9 MPa in C60/S460, and 17.8 MPa in C160/S700 solution, 100 years after construction.

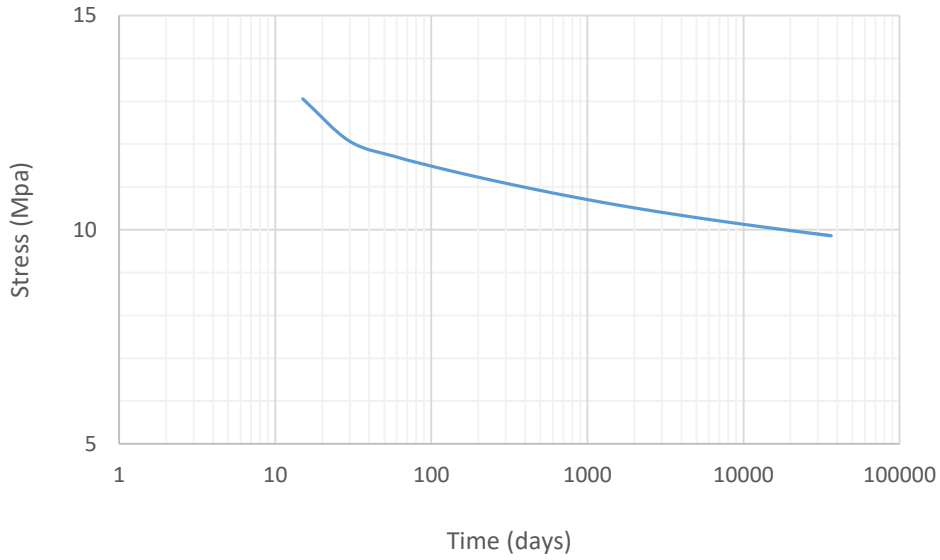

Figure 3.29 Stresses in concrete core due to dead load C60/S460

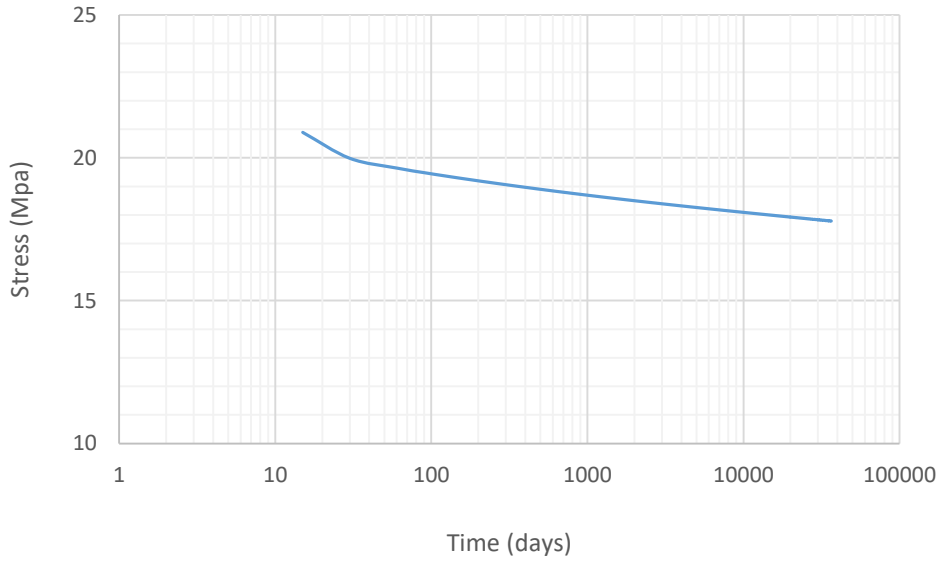

Figure 3.30 Stresses in concrete core due to dead load C160/S700

The stress decrement in the concrete core in arch springing section due to concrete creep is 5.0 MPa (33.7%) and 4.8 MPa (21.3%), for C60/S460 and C160/S700, respectively.

3.4.5 Serviceability Limit State (SLS)

The service conditions were preliminarily verified based on the bridge deck deflection. The vertical deflection of the bridge deck was determined for the combination of actions SLS 1 (3.8) and SLS 2 (3.9) defined in section 3.3, taking into account the deformations resulting from concrete creep, whose determination is described in section 3.4.4. Figure 3.31 and

Figure 3.32 contain the deformed deck configuration for both combinations and concrete creep, with the maximum values presented in Table 3.27.

For the present case, considering a speed of 300 km/h of the train and an L value of 400 m corresponding to the arch span, it seems possible to preliminarily consider a very good level of comfort, considering that the limit of the maximum vertical displacement is 33.3 cm, which corresponds to the limit of L/δ =1200.

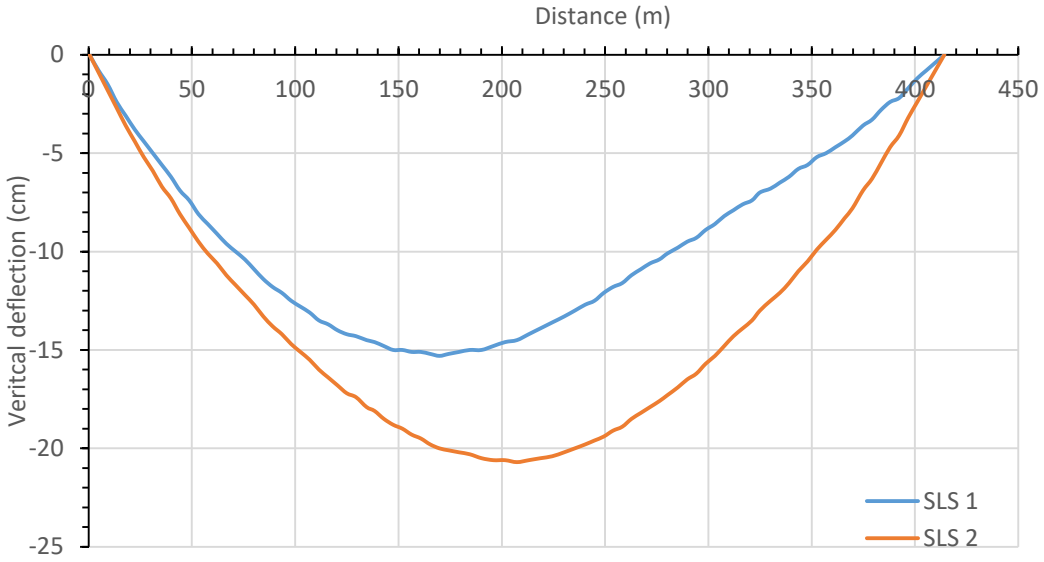

Figure 3.31 Deformed deck configuration for SLS 1 and SLS 2 combinations taking into account creep deformations for C60/S460.

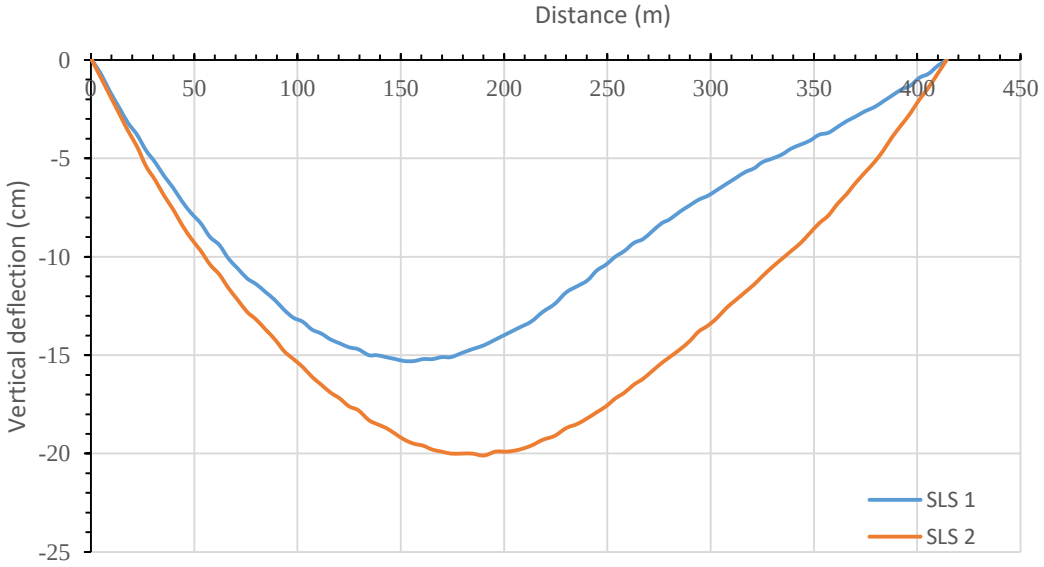

Figure 3.32 Deformed deck configuration for SLS 1 and SLS 2 combinations taking into account creep deformations for C160/S700.

Table 3.27 Maximum deflections of the deck [in cm].

Solution	Temperature	LM71	Creep	SLS 1	SLS 2
C60/S460	16.4	4.0	4.4	15.3	20.7
C160/S700	16.2	4.9	3.3	15.3	20.1

3.4.6 Modal analysis

The modal analysis was performed by Robot Autodesk Structural Office (2019) [92]. The natural frequencies of the bridge are listed in Table 3.28 and Table 3.29, for the first 3 vibration modes. Natural frequencies values of the same order of magnitude were observed in other existing long span railway arch bridges [96]. The first 3 vibration modes are shown in Figure 3.33, Figure 3.34 and Figure 3.35, respectively.

Table 3.28 The natural frequencies of the bridge (Hz) C60/S460

Vibration mode	Frequencies (Hz)
1st mode (horizontal)	0.29
2nd mode (vertical)	0.34
3rd mode (horizontal)	0.44

Table 3.29 The natural frequencies of the bridge (Hz) C160/S700

Vibration mode	Frequencies (Hz)
1st mode (horizontal)	0.43
2nd mode (vertical)	0.58
3rd mode (horizontal)	0.60

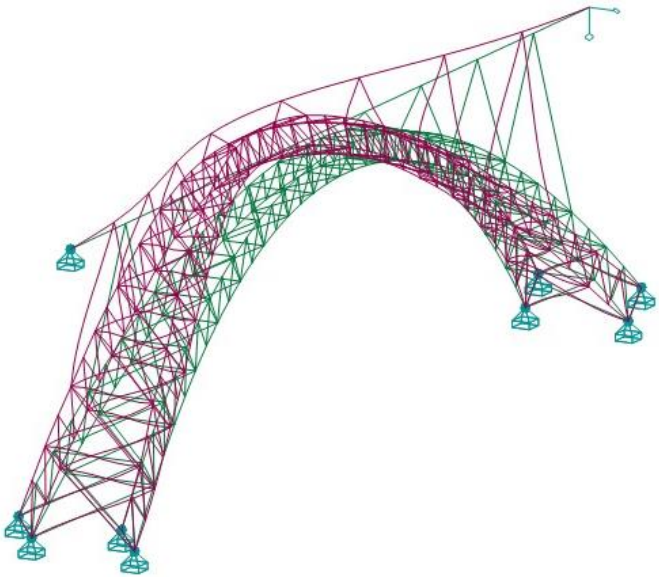

Figure 3.33 First vibration mode

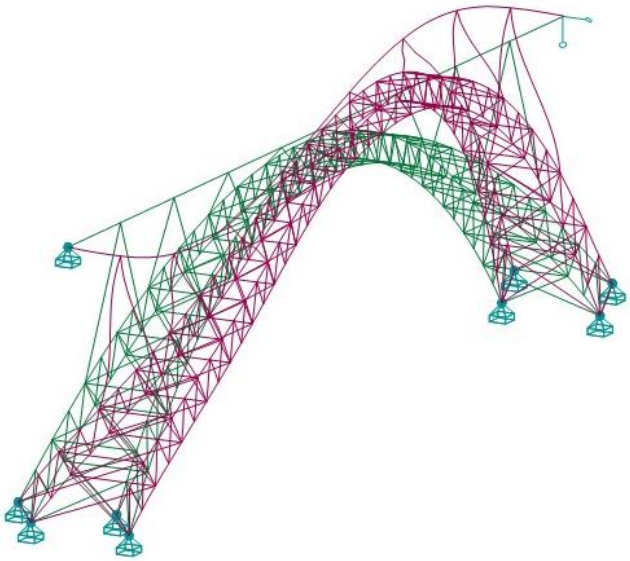

Figure 3.34 Second vibration mode

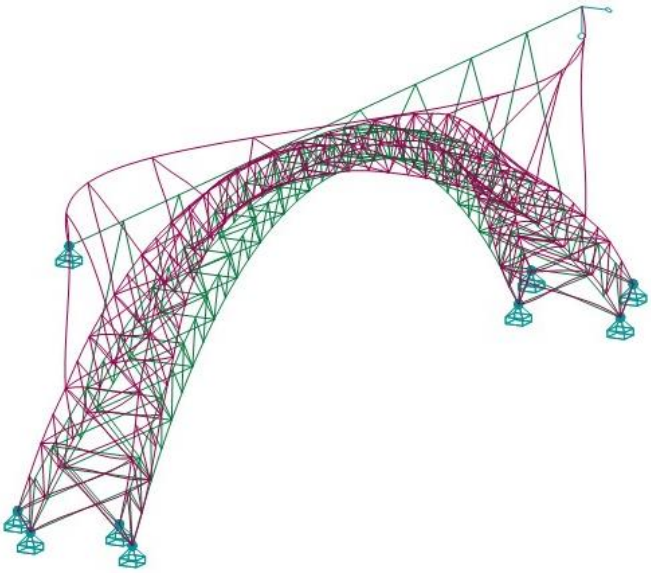

Figure 3.35 Third vibration mode

3.5 Truss rib section

3.5.1 Solution description

In this solution, the arch ribs are two CFST trusses, each rib consists of 4 tubes (Figure 3.3). This solution is typically used for long span arch bridges [10], providing large flexural stiffness.

The CFST arch tubes are of ϕ2000mm×57mm for the case of C60/S460. In the case of C160/S700, the CFST arch tubes are of ϕ1290mm×57mm. Table 3.30 and Table 3.31 contain the relevant parameters of the adopted CFST sections.

Table 3.30 CFST sections properties- truss rib section

Solution	d (cm)	t (cm)	Ac (cm^2)	As (cm^2)	Inertia,c (cm^4)	Inertia,s (cm^4)
C60/S460	200	5.7	27936.58	3479.35	62106442.36	16433373.98
C160/S700	129	5.7	10861.87	2207.94	9388564.32	4204855.82

Table 3.31 d/t relation and steel percentage in CFST sections

Solution	d/t	max (d/t)	ρ (%)	ξ
C60/S460	35.09	45.98	0.12	1.25
C160/S700	22.63	30.21	0.20	1.16

Table 3.32 shows the resistance of the section and the steel contribution ratio.

Table 3.32 The resistance of the section and the steel contribution ratio

Solution	N_{Rd} (MN)	$A_s f_{yd}$ (MN)	δ
C60/S460	250.92	139.17	0.55
C160/S700	250.26	134.40	0.54

3.5.2 Construction phase

3.5.2.1 Structural analysis

The steel arch was analyzed using Robot 2019 [92], with a three-dimensional bar model (Figure 3.36), with fixed translations in the arch supports.

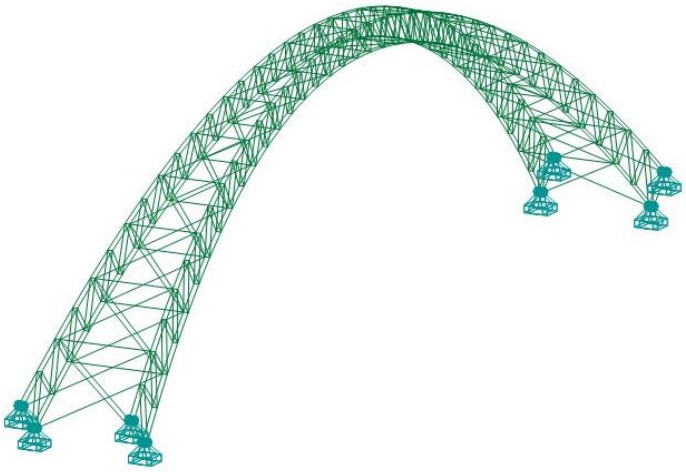

Figure 3.36 three-dimensional bar model (construction phase)

Linear and geometrically nonlinear static analyses were performed. The nonlinear analysis was also carried out by inducing the buckling mode shapes of the arch to the model as initial imperfection, for an out-of-plane local imperfection near the arch base with a value of L/350 (Figure 3.37) and an out-of-plan global imperfection with a value of L1/300 where $L1=\sqrt{20L}$ (Figure 3.38), according to [93] [94], with the same values mentioned in Table 3.7.

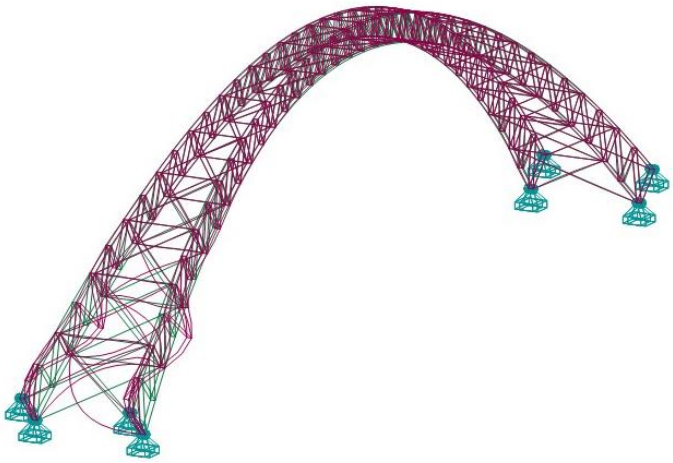

Figure 3.37 Local buckling shape of the arch (construction phase)

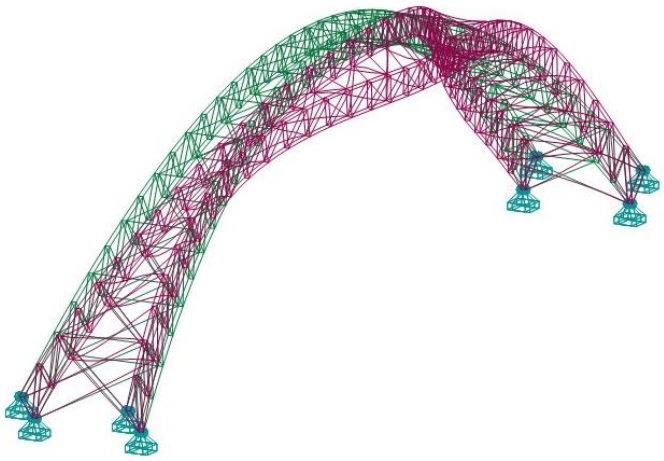

Figure 3.38 Global buckling shape of the arch (construction phase)

The maximum axial forces in the arch occur in the cross sections in arch springing. The results of the maximum axial forces resulting from the combination (3.16) are presented in Table 3.33 for both solutions.

Table 3.33 Maximum axial forces in the steel tube in (MN)

Solution	Linear analysis	Nonlinear analysis
C60/S460	62.953	63.226
C160/S700	39.572	39.707

.

3.5.2.1.1 Stability structural analysis

The critical buckling distributed load on the arch was obtained by a linear buckling analysis using Robot 2019 [92], with the results described in Table 3.34, for the first buckling mode (Figure 3.39 and Figure 3.40).

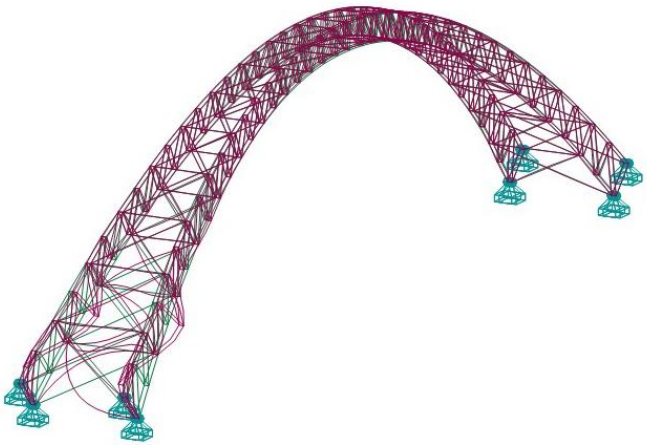

Figure 3.39 First buckling mode of the arch C60/S460 (construction phase)

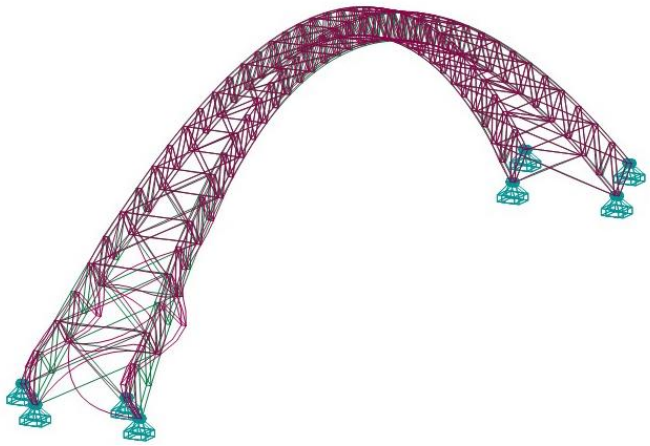

Figure 3.40 First buckling mode of the arch C160/S700 (construction phase)

Table 3.34 The critical distributed load on the arch associated with the first buckling mode (construction phase).

Solution	q_{cr} (KN/m)
C60/S460	1965.53
C160/S700	765.62

Table 3.35 contains the critical axial force N_{cr}, the slenderness λ as well as the buckling length L_{cr} associated with the first buckling mode of the steel arch (Figure 3.39 and Figure 3.40) for two conditioning bars with the maximum axial force and the minimum critical force, located in arch springing.

Table 3.35 Critical axial force N_{cr}, the slenderness λ and buckling length L_{cr} associated with the first buckling mode of the arch (construction phase).

Solution	N_{cr} (MN)	λ_y	λ_z	$L_{cr,y}$ (m)	$L_{cr,z}$ (m)
C60/S460	324.61	47.13	47.13	32.39	32.39
	800.80	30.00	30.00	20.62	20.62
C160/S700	116.41	62.70	62.70	27.36	27.36
	285.28	40.06	40.06	17.48	17.48

3.5.2.2 Resistance check of steel tubes

Table 3.36 shows the results of the buckling resistance data as well as the design value of the axial force in the conditioning bars. As the results show, the axial buckling resistance is verified for both solutions.

Table 3.36 Axial buckling resistance of the steel tube and the design value of the maximum axial force in the tube

Solution	$\bar{\lambda}$	i (cm)	λ_I	χ	$N_{b,rd}$ (MN)	$N_{x,ed}$ (MN)
C60/S460	0.70	68.72	67.12	0.90	124.61	12.00
	0.45	68.72	67.12	0.96	133.85	40.15
C160/S700	1.15	43.64	54.41	0.61	81.77	18.71
	0.74	43.64	54.41	0.88	118.56	63.43

3.5.2.2.1 Combined compression and bending moment verification

The steel tube resistance is verified for the combined effect of axial compression and bending, considering the combination (3.16) and the bending effects related to the model imperfections. This verification is applied for two bars with critical combinations of simultaneous axial force and bending moment. The values of the interaction factors needed for the expressions (3.21) and (3.22) are presented in Table 3.37, whose determination is described in Appendix C. The values of N_{ed}, $M_{y,Ed}$, $M_{z,Ed}$,N_{Rk} and $M_{i,Rk}$ are presented in Table 3.38. Both equations (3.21) and (3.22) verify the condition ≤ 1, for both solutions, as shown in Table 3.39.

Table 3.37 Interaction factors

Solution	k_{yz}	k_{zy}	k_{yy}	k_{zz}
C60/S460	0.69	0.81	0.41	0.48
	0.79	0.66	0.47	0.40
C160/S700	0.69	0.88	0.42	0.54
	0.83	0.77	0.50	0.46

Table 3.38 Ne_d, $M_{y,Ed}$, $M_{z,Ed}$,N_{Rk} and $M_{i,Rk}$ in the steel arch

Solution	N_{ed} [MN]	$M_{y,Ed}$ [MNm]	$M_{z,Ed}$ [MNm]	N_{Rk} [MN]	$M_{i,Rk}$ [MNm]
C60/S460	63.12	1.61	0.90	160.05	99.02
	38.96	1.79	4.54	160.05	99.02
C160/S700	39.71	1.09	0.55	154.56	60.70
	16.03	1.32	3.10	154.56	60.70

Table 3.39 Combined bending and axial compression verification equations

Solution	Equation (3.21)	Equation (3.22)
C60/S460	0.41	0.47
	0.25	0.29
C160/S700	0.29	0.33
	0.12	0.13

3.5.3 Service phase and ULS design

3.5.3.1 Structural analysis

The arch bridge solution was analyzed with a three-dimensional bar model (Figure 3.41) with fixed translations in the arch supports. The deck was modeled with fixed translations on one side and free displacement in the axial direction on the other. The proprieties of the equivalent CFST section are presented in Table 3.40.

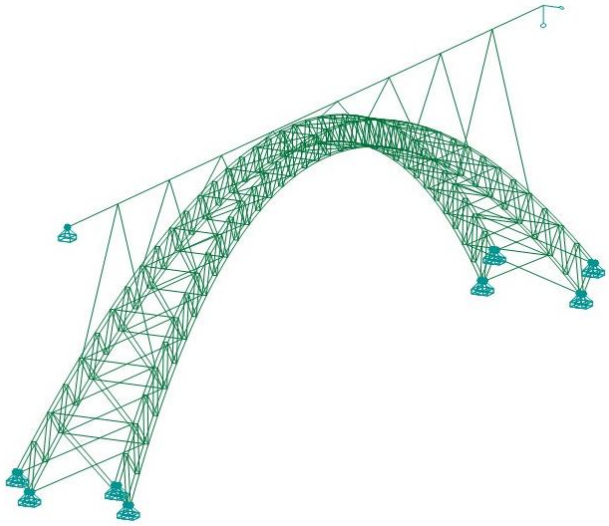

Figure 3.41 Three-dimensional bar model of the bridge

Table 3.40 The proprieties of the equivalent CFST sections

Solution	$A_{,eq}$ [cm2]	$Inertia_{,eq}$ [cm4]	$Inertiax_{,eq}$ [cm4]	$E_{,eq}$ [GPa]	W [KN/m]
C60/S460	45874.64	146830081.66	293660163.31	40.73	96.63
C160/S700	19292.19	25443468.35	50886936.70	55.06	44.16

Linear and geometrically nonlinear static analyses were performed by Robot 2019 [92]. The nonlinear analysis was carried out by inducing the buckling mode shape of the arch to the model as the initial imperfection. Two models were considered, one for an out-of-plane local imperfection near the arch base with a value of L/300 (Figure 3.42), another one for an-out of-plan global imperfection with a value of L1/300 where $L1=\sqrt{20L}$ (Figure 3.43), according to [35][94], with the values mentioned in Table 3.41.

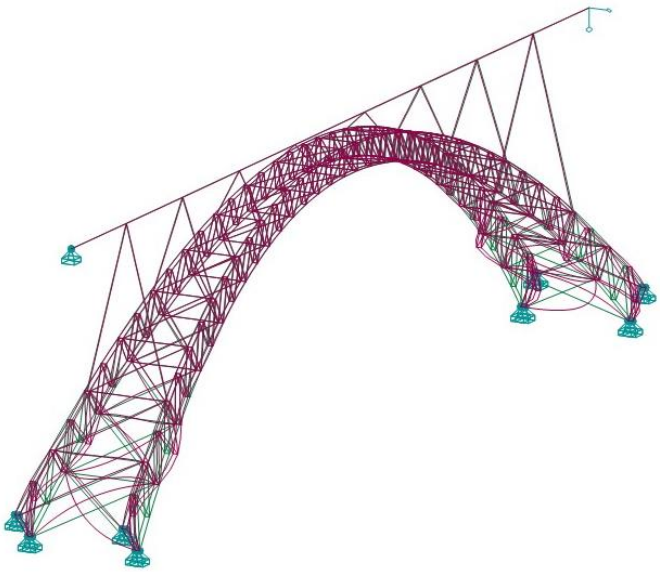

Figure 3.42 Local buckling shape of the arch

Figure 3.43 Global buckling shape of the bridge

Table 3.41 Local and global initial imperfection values e0

	Imperfection e_o (m)
Global	0.30
Local	0.10

The maximum axial force in the arch occurs in the cross section in arch springing, in the left bottom chords. The results of the axial forces of these sections for dead load and ultimate

limit state combinations are presented in Table 3.42 and Table 3.43. The values of the maximum bending moments are listed in Table 3.44.

Table 3.42 Maximum axial forces C60/S460 in (MN)

Analysis type	Dead load	ULS 1	ULS 2	ULS 3
Linear analysis	63.22	125.75	99.90	118.26
Nonlinear analysis	64.14	126.85	101.86	119.2

Table 3.43 Maximum axial forces C160/S700 in (MN)

Analysis type	Dead load	ULS 1	ULS 2	ULS 3
Linear analysis	44.946	97.392	75.728	90.560
Nonlinear analysis	45.485	99.623	77.234	94.328

Table 3.44 Maximum bending moments

Analysis type	Linear analysis		Nonlinear analysis	
Solution	My (MNm)	Mz (MNm)	My (MNm)	Mz (MNm)
C60/S460	14.340	8.436	14.664	9.589
C160/S700	6.725	4.076	7.103	5.149

3.5.3.2 Stability structural analysis

The critical buckling distributed load on the arch was obtained by a linear buckling analysis using Robot 2019 [92], with the results described in Table 3.45, for the first buckling mode (Figure 3.44 and Figure 3.46). Figure 3.45 and Figure 3.47 describe the second buckling mode.

Table 3.45 The critical distributed load on the arch associated with the first buckling mode

Solution	q_{cr} (KN/m)
C60/S460	2724.80
C160/S700	1006.57

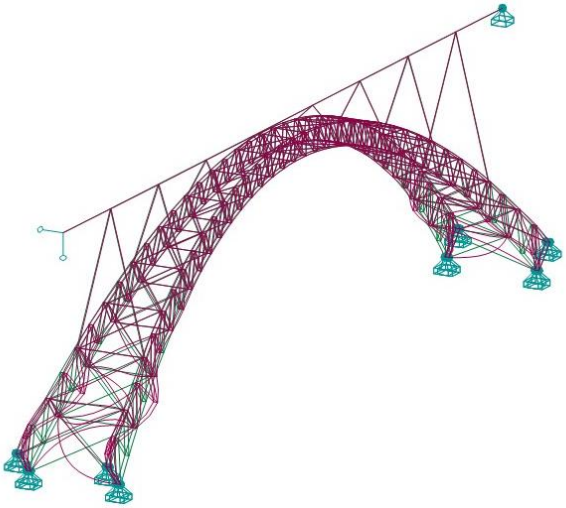

Figure 3.44 First buckling mode of the arch C60/S460

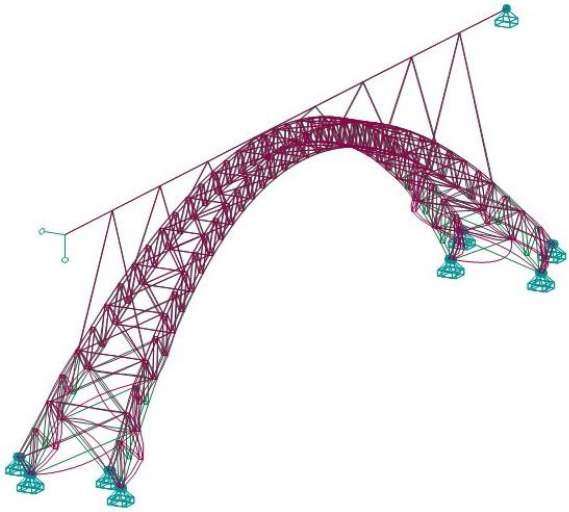

Figure 3.45 Second buckling mode of the arch C60/S460

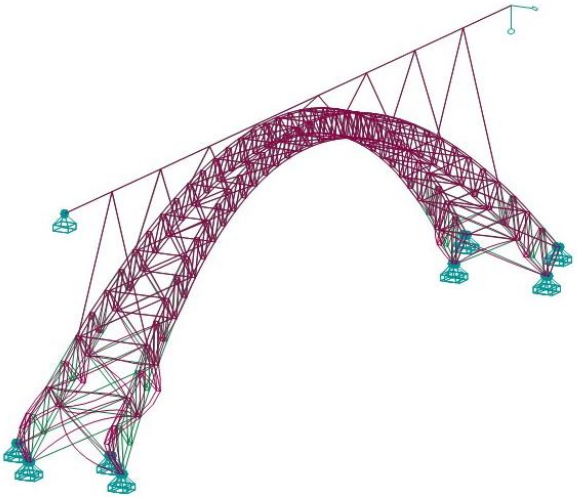

Figure 3.46 First buckling mode of the arch C160/S700

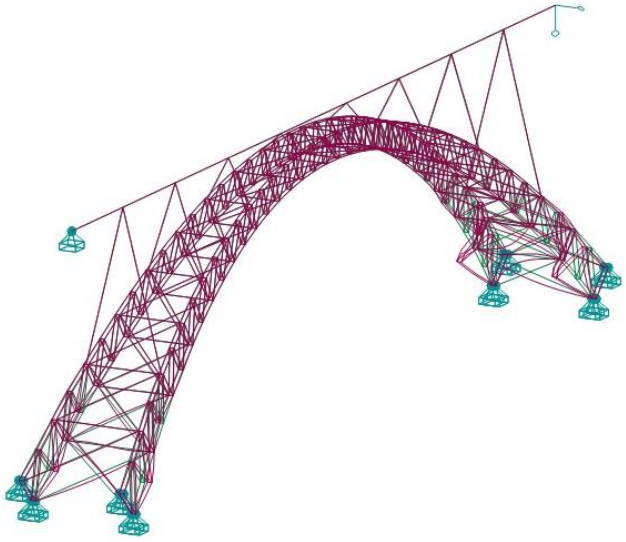

Figure 3.47 Second buckling mode of the arch C160/S700

The critical buckling distributed load on the deck was also obtained by a linear buckling analysis. The buckling of the arch appears in the 6th buckling shape for C60/S460 as a global in-plane shape (Figure 3.48) where the first 5 buckling modes are associated with the columns.

For C160/S700, the arch buckling occurs in the 5th buckling shape as a local out-of-plane shape (Figure 3.49) where the first 4 buckling modes are associated with the columns. The critical buckling distributed load on the deck associated with the arch buckling is presented in Table 3.46.

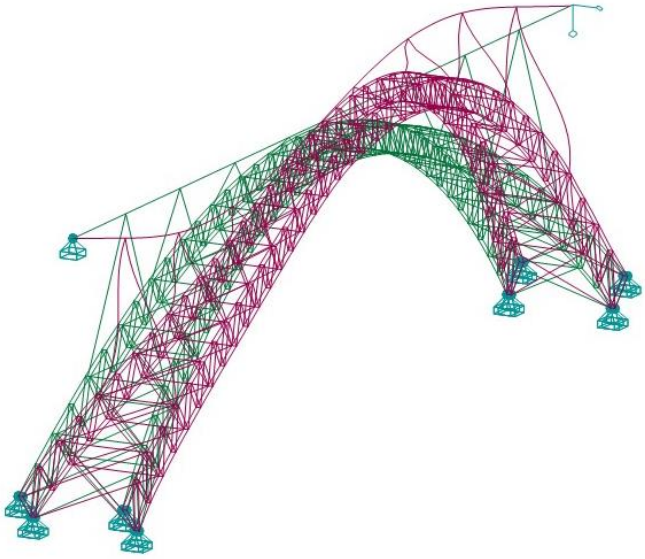

Figure 3.48 Sixth buckling mode of the bridge, the first one associated with the arch C60/S460

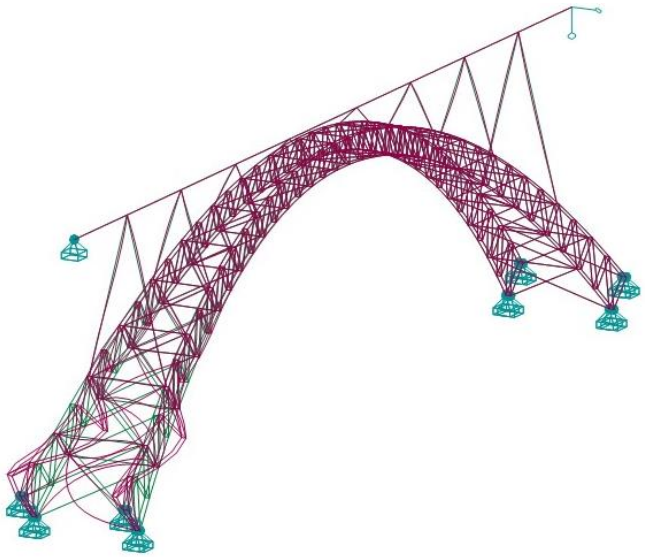

Figure 3.49 Fifth buckling mode of the bridge, the first one associated with the arch C160/S700

Table 3.46 The critical buckling distributed load on the deck associated with the arch buckling.

Solution	q_{cr} (KN/m)
C60/S460	20172.20
C160/S700	8622.42

Table 3.47 contains the critical axial force N_{cr}, the slenderness λ and the buckling length L_{cr} associated with the first buckling mode of the arch (Figure 3.44 and Figure 3.46), for two conditioning bars with the maximum axial force and the minimum critical force (located in arch springing).

Table 3.47 Critical axial force N_{cr}, the slenderness λ and the buckling length L_{cr} associated with the first buckling of the arch

Solution	N_{cr} (MN)	λ_y	λ_z	$L_{cr,y}$ (m)	$L_{cr,z}$ (m)
C60/S460	864.57	46.19	46.19	23.82	23.82
	386.75	69.05	69.05	35.61	35.61
C160/S700	383.60	52.28	52.28	17.53	17.53
	141.51	86.08	86.08	28.86	28.86

3.5.3.2 Safety verifications

The buckling resistance verification has been carried out for the two conditioning bars. The results of the axial buckling resistance are shown in Table 3.48, in addition to the maximum axial force for ULS combinations, which in this case is the axial force resulting from the combination ULS 1 (3.2).

Table 3.48 Buckling resistance of the CFST tube sections when the loading is applied on the deck and the axial force due to ULS 1 combination

Solution	$\bar{\lambda}$	i (cm)	χ	$N_{b,Rd}$ (MN)	N_{Ed} (MN)
C60/S460	0.62	51.57	0.88	221.81	126.85
	0.92	51.57	0.72	180.75	44.86
C160/S700	0.93	33.53	0.72	179.47	99.62
	1.52	33.53	0.36	90.79	28.70

As shown in Table 3.48, the buckling resistance of the CFST sections to compression is verified.

3.5.3.2.1 Combined compression and bending moment verification

The diagrams of the combined bending moment and compression resistance of the section were obtained using Interac [95]. The diagrams are presented in Figure 3.50 and Figure 3.51. This verification is applied for two sections with critical combinations of simultaneous axial force and bending moment.

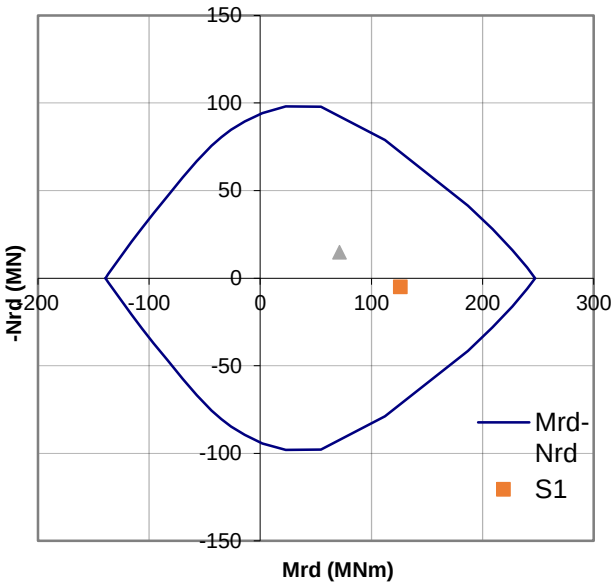

Figure 3.50 Combined bending moment and compression verification for C60/S460

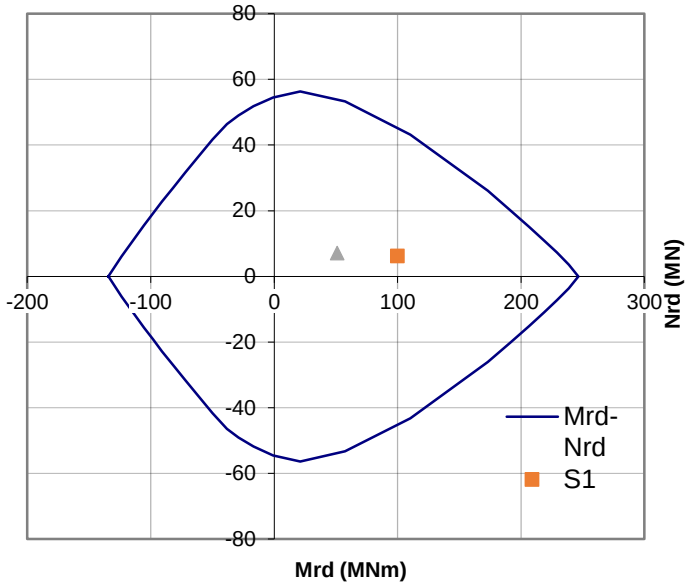

Figure 3.51 Combined bending moment and compression verification for C160/S700

Table 3.49 contains the design values of the bending moments $M_{y,Ed}$ and $M_{z,Ed}$ as well as the plastic bending resistance taking into account the normal force $M_{pl,N,Rd}$.

Table 3.49 $M_{y,Ed}$, $M_{z,Ed}$ and $M_{pl,N,Rd}$.

Solution	$M_{y,Ed}$ (MNm)	$M_{z,Ed}$ (MNm)	$M_{pl,N,Rd}$ (MNm)	$\frac{M_{y,Ed}}{M_{pl,N,Rd}} + \frac{M_{z,Ed}}{M_{pl,N,Rd}}$
C60/S460	14.340	4.794	92	0.21
	14.664	4.971	90	0.22
C160/S700	6.725	2.830	53	0.18
	7.103	3.001	53	0.19

As Table 3.49 shows, the expression (3.26) is satisfied, thus the combined compression and bending moment resistance is verified for both solutions.

3.5.4 Creep analysis

3.5.4.1 Long-term deformations

An increase of 4.8 cm of the maximum deflection in the bridge deck was observed for C60 solution, while 3.2 cm for C160 solution, due to concrete creep in the arch tubes. Figure 3.52 and Figure 3.53 show the vertical deflection of the deck caused by dead loads.

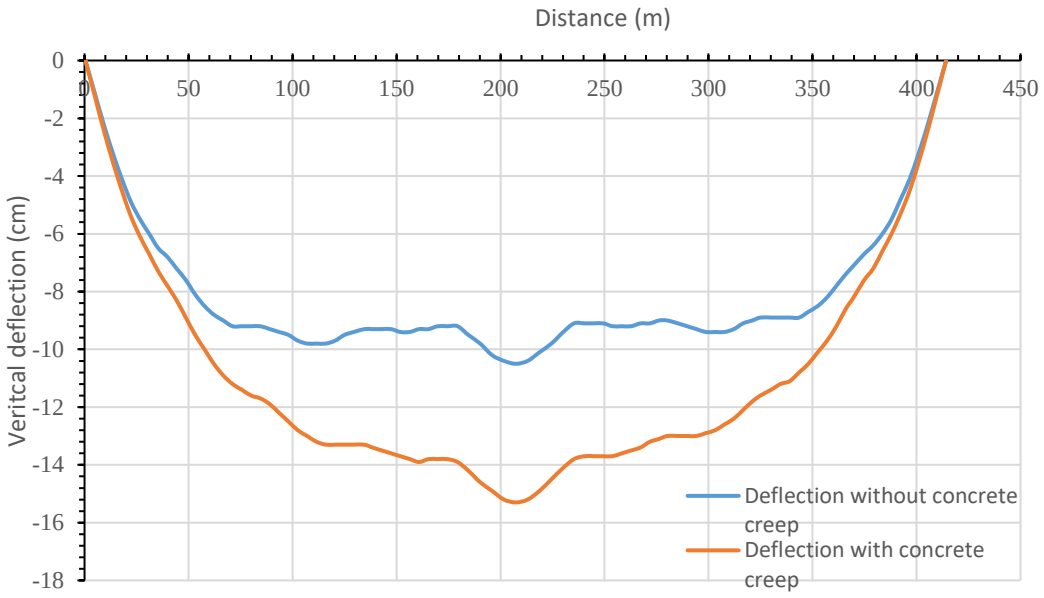

Figure 3.52 Vertical deflection of the deck for C60/S460.

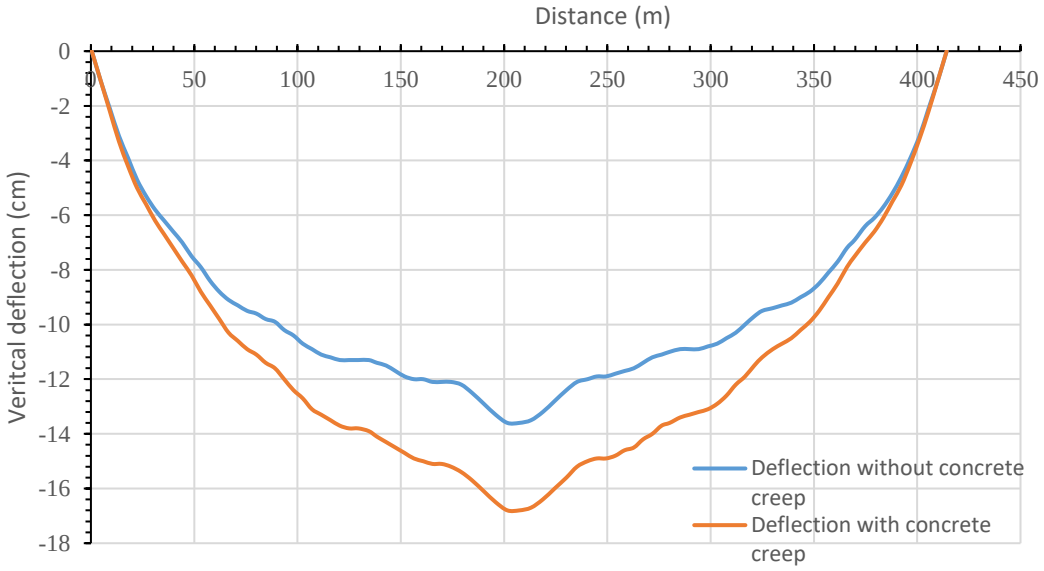

Figure 3.53 Vertical deflection of the deck for C160/S700.

The deformation in the arch tubes also increased because of concrete creep. The vertical deflection of the arch crown section due to concrete creep reaches a value of 4.6 cm for C60 solution and a value of 3.1 cm for C160 solution, after 100 years. The creep deformation curve is shown in Figure 3.54.

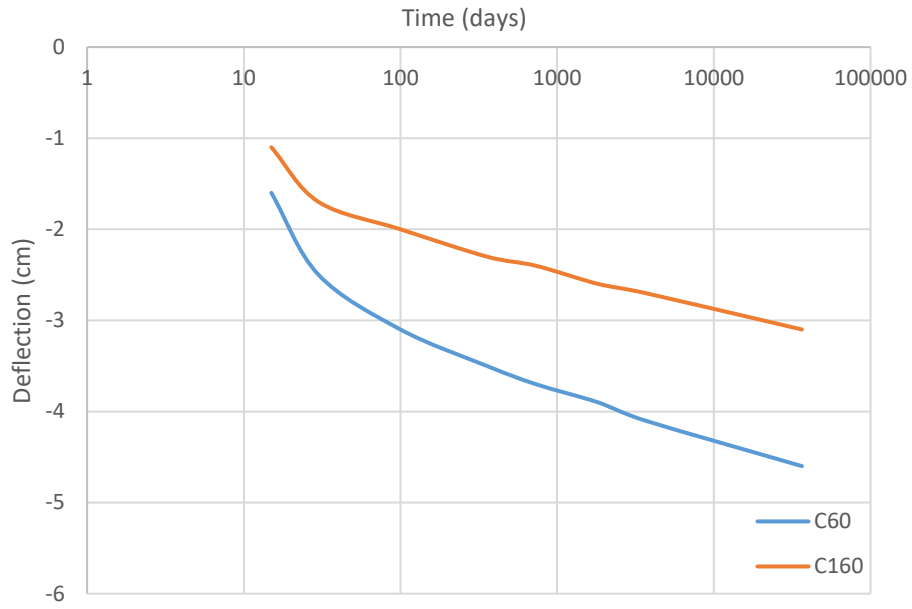

Figure 3.54 Creep deformation curve in arch crown section

3.5.4.2 Stress in steel tube

Figure 3.55 and Figure 3.56 show the stress curves of the steel tube at arch springing section, which is the section with the maximum force. The stress due to dead loads in the steel tube increases with time, to reach 108.2 MPa in C60/S460, and 114.9 MPa in C160/S700, 100 years after construction.

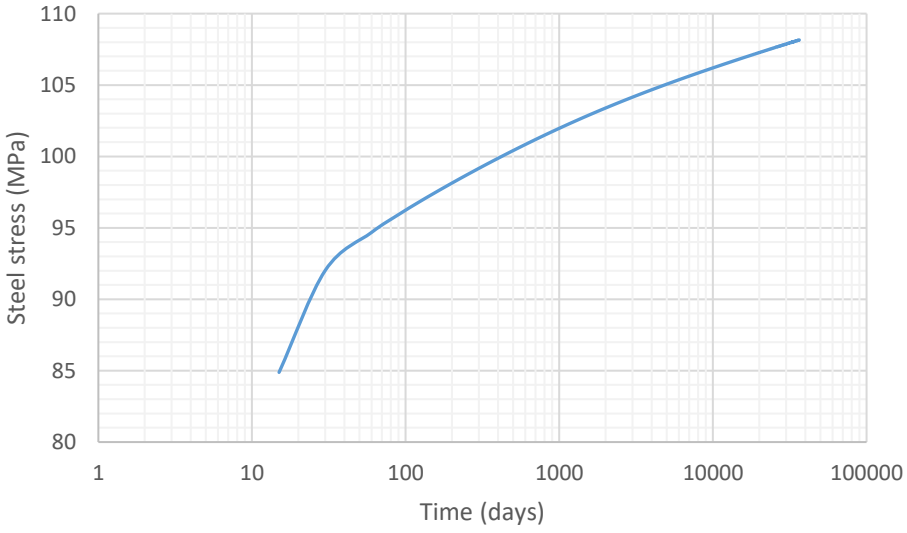

Figure 3.55 Stresses in steel tube due to self-weight for C60/S460

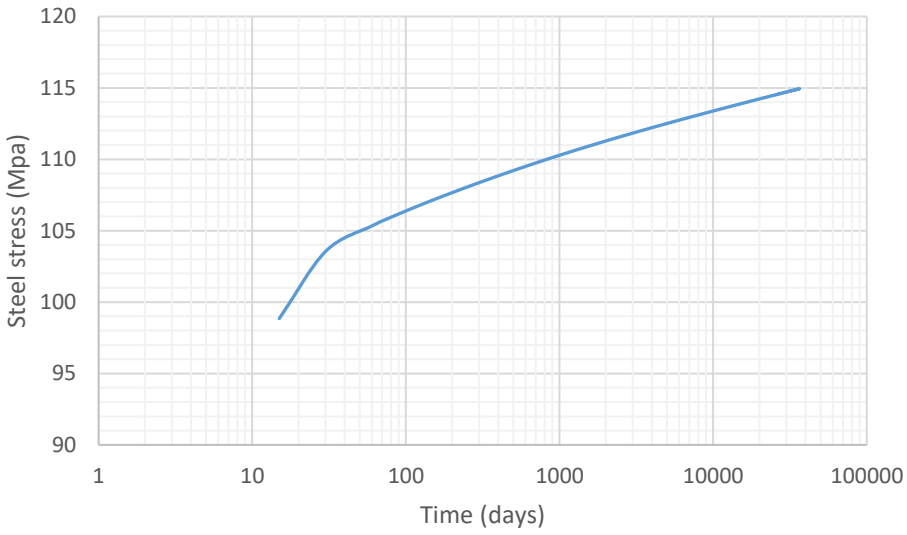

Figure 3.56 Stresses in steel tube due to self-weight for C160/S700

The stress increment in arch springing section in C60/S460 and C160/S700 is 36.08 MPa (50.0%) and 24.98 MPa (27.8%), respectively. Table 3.50 shows that the critical sections are subjected to compression only, so the equation (3.28) can be used to estimate the bending moments in the steel tube.

Table 3.50 Nx,My and Mz due to SLS3

Solution	N_x (MN)	M_y (MNm)	M_z (MNm)	D/8 (cm)	e_y (cm)	e_z (cm)
C60/S460	85.21	0.27	1.86	25.00	0.31	2.19
	49.42	10.99	4.63		22.23	9.37
C160/S700	64.01	0.10	0.44	16.13	0.16	0.69
	37.99	5.21	2.21		13.72	5.81

Adding the stress increments due to concrete creep to the stresses resulting from the combination SLS 3 (3.10), the stresses are still much less than the strength of S460 and S700, as shown in Table 3.51.

Table 3.51 Stress redistribution in the steel tube due to concrete creep

Solution	$\sigma_{s,SLS3}$ (MPa)	$\Delta\sigma_s$ (MPa)	σ_s (MPa)	f_{yd} (MPa)
C60/S460	103.24	36.08	139.32	400.00
	111.15	36.08	147.23	
C160/S700	131.94	24.98	156.92	608.70
	147.00	24.98	171.98	

3.5.4.3 Stress in concrete core

Figure 3.57 and Figure 3.58 give the stress curves of the concrete core at arch springing section. It is shown that the stresses due to dead load in the concrete core decrease over time, to reach 9.49 MPa in C60/S460, and 18.51 MPa in C160/S700 solution, 100 years after construction.

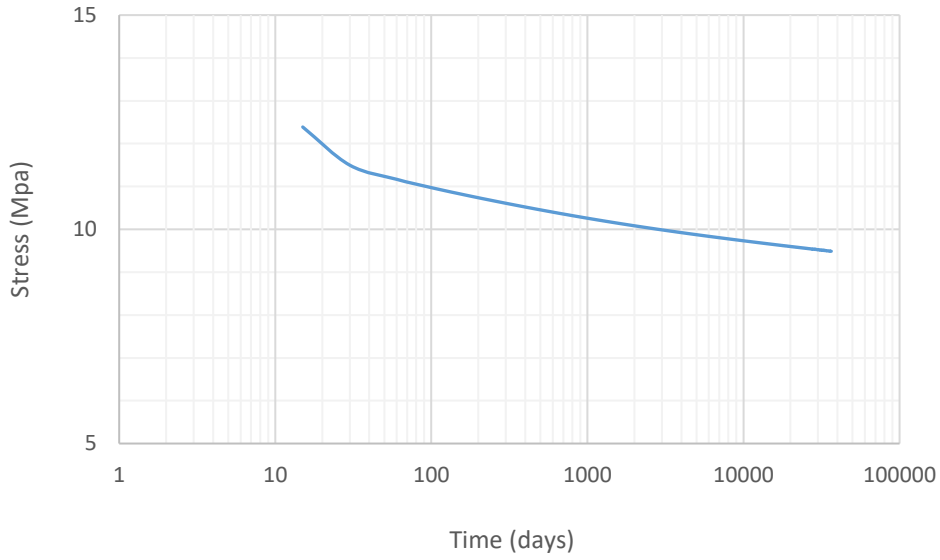

Figure 3.57 Stresses in concrete core due to self-weight C60/S460

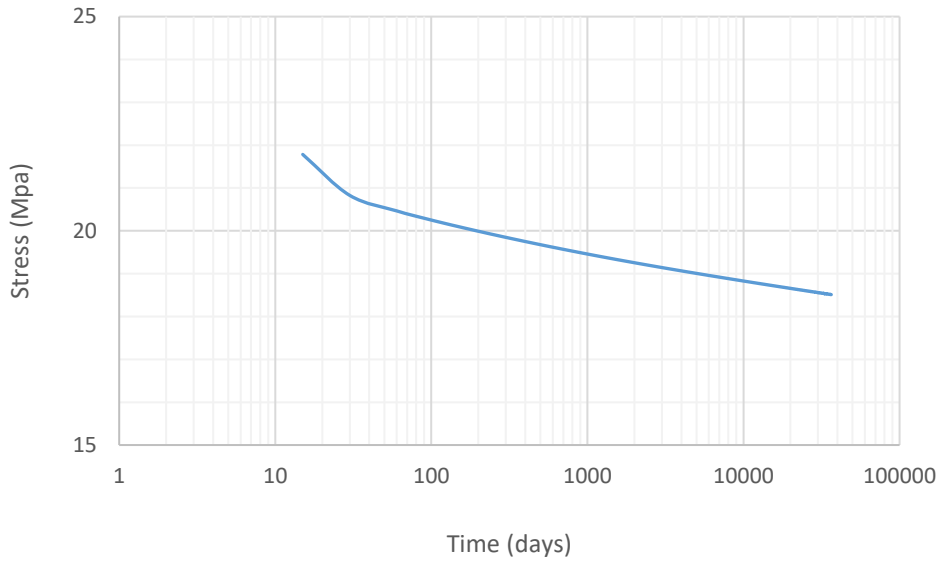

Figure 3.58 Stresses in concrete core due to self-weight C160/S700

The stress decrement in the concrete core in arch springing section due to concrete creep is 4.5 MPa (32.1%) and 5.1 MPa (21.5%), for C60/S460 and C160/S700, respectively.

3.5.5 Serviceability Limit State (SLS)

The same considerations mentioned in section 3.4.5 were adopted. Figure 3.59 and Figure 3.60 contain the deformed deck configuration for both SLS 1 and SLS 2 combinations and taking into account deflections due to concrete creep, whose determination is described in section 3.5.4. The maximum deflections values are presented in Table 3.52. it seems possible to preliminarily consider a very good level of comfort, taking into account the limit of the maximum vertical displacement of 33.3 cm, which corresponds to the limit of L/δ =1200.

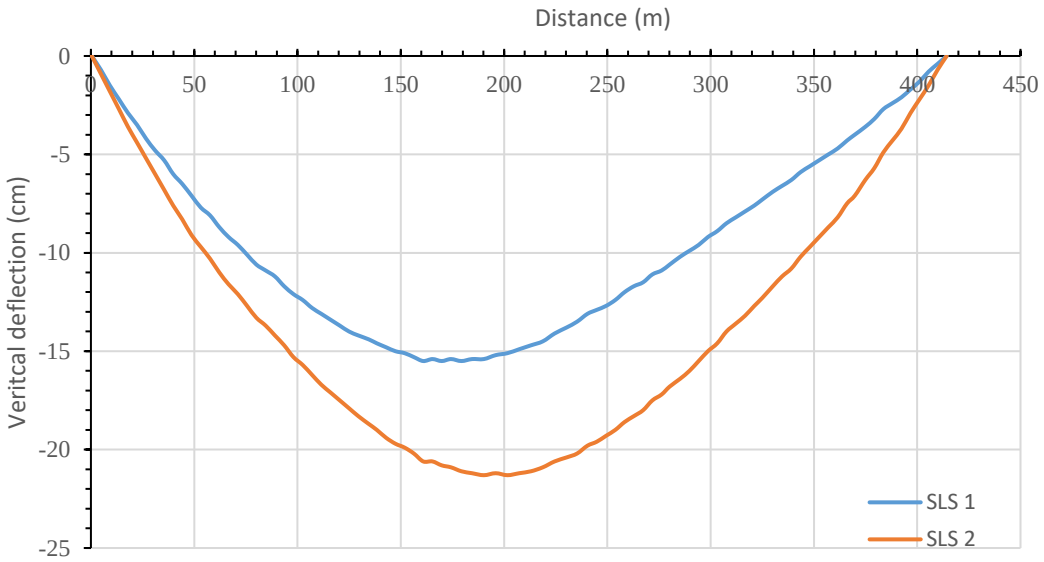

Figure 3.59 Deformed deck configuration for SLS 1 and SLS 2 combinations taking into account creep deformations for C60/S460.

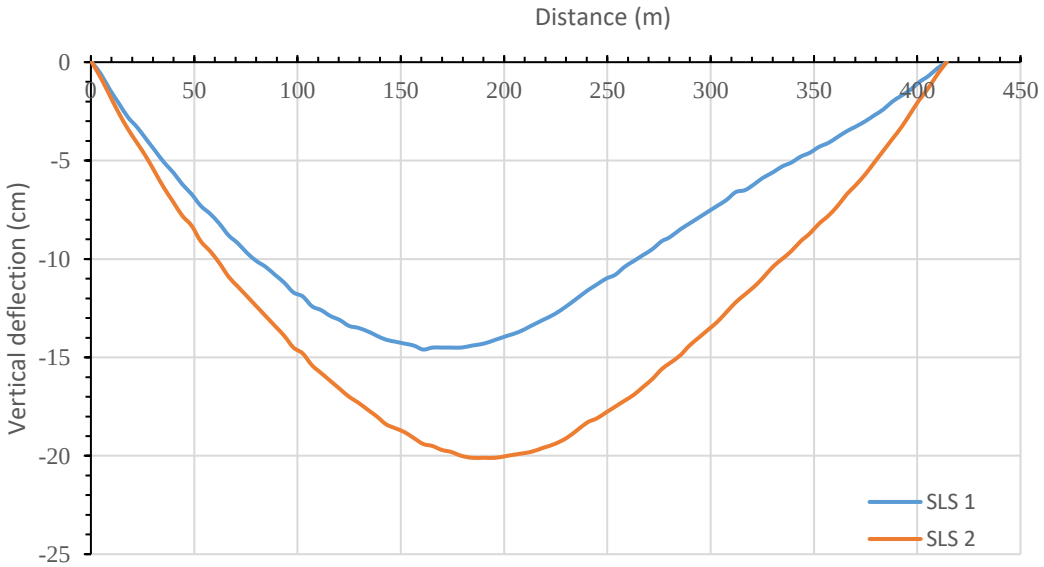

Figure 3.60 Deformed deck configuration for SLS 1 and SLS 2 combinations taking into account creep deformations for C160/S700.

Table 3.52 Maximum deflections of the deck [in cm].

Solution	Temperature	LM71	Creep	SLS 1	SLS 2
C60/S460	16.1	2.8	4.8	15.5	21.3
C160/S700	16.3	3.5	3.2	14.6	20.1

3.5.6 Modal analysis

The modal analysis was performed by Robot 2019 [92]. The natural frequencies of the bridge are listed in Table 3.53 for C60/S460 and Table 3.54 for C160/S700, for the first 3 vibration modes. The first three vibration modes are shown in Figure 3.61, Figure 3.62 and Figure 3.63 for both solutions.

Table 3.53 The natural frequencies of the bridge (Hz) C60/S460

Vibration mode	Frequencies (Hz)
1st mode (horizontal)	0.30
2nd mode (vertical)	0.38
3rd mode (horizontal)	0.47

Table 3.54 The natural frequencies of the bridge (Hz) C160/S700

Vibration mode	Frequencies (Hz)
1st mode (horizontal)	0.31
2nd mode (vertical)	0.44
3rd mode (horizontal)	0.47

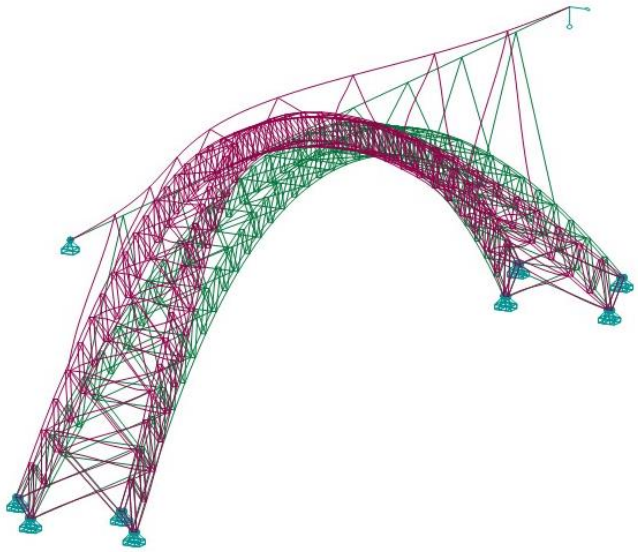

Figure 3.61 First vibration mode

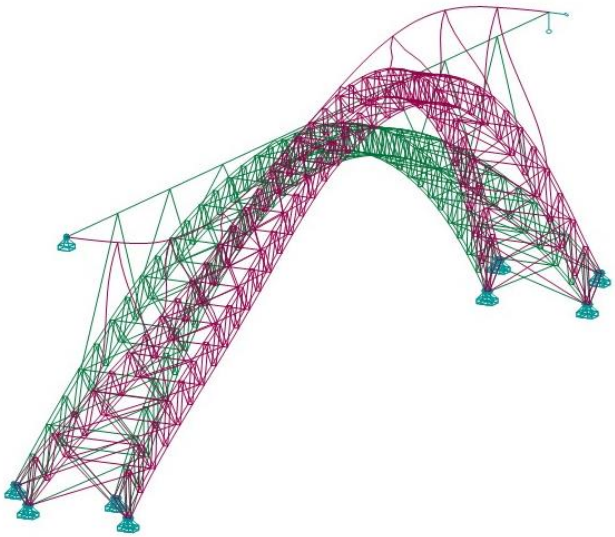

Figure 3.62 Second vibration mode

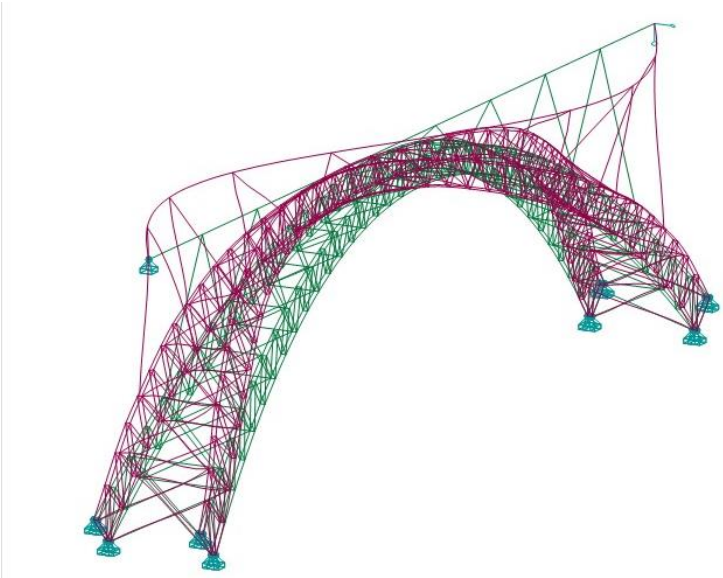

Figure 3.63 Third vibration mode

3.6 Discussion of the analysis

The advantage of lower material consumption is evident in C160/S700 solutions, making the structure lighter. The arch with C160/S700 combination is 43% lighter than with C60/S460 combination in two tubes rib section and 54% lighter in truss rib section. Regarding the reduction of materials quantity in C160/S700 combination, the reduction is of 50% in concrete and 28% of steel in two tubes section, and 61% in concrete and 37% in steel in truss rib section. The obtained results demonstrate the advantages of using high-strength materials. The analyzed solutions may be considered as overdesigned, being

possible to optimize them. This is due to the very demanding preliminary design considered for the analyses. However, this fact does not affect the comparison between the uses of high and low strength materials, which is a goal of the present work.

In the analyzed solutions, C160 shows a relatively better creep behavior. Creep coefficients reach a value of 0.77 in C160 and 1.55 in C60, 100 years after construction. Concrete creep has a limited influence on the overall deformation, the deformations are similar in the two combinations of materials. The increase of stresses in the steel tube was small, considering the adopted steel grades. However, in case of using lower steel grades, the effects of creep in the stresses of the steel tube can create undesirable effects, namely early yielding of the section. In the case of high strength materials, the better behavior of high strength concrete and the lower self-weight compensate for the lower cross-sectional area of the steel tube.

Chapter 4 Conclusions

This thesis aimed to evaluate the efficiency of using high strength concrete in long span CFST arch bridges. Thus, results of experimental studies on the behaviour of CFST elements were collected from literature, considering different levels of concrete strength, namely normal and high strength concrete. The results were studied and analyzed considering the internal mechanical behaviour of the concrete infill and the effect of its failure mechanism on the loading capacity of CFST elements.

It has been found that the enhancement of loading capacity of CFST elements, due to the confinement provided by the steel tube, is based on the internal mechanical behaviour of the concrete core. This behaviour differs when using different types of concrete, which results in distinct levels of confinement. The enhancement of loading capacity of CFST elements using high strength concrete due to confinement is not significant when compared to normal strength concrete. This is due to the unfavorable failure mode, in inclined plan, which the steel tube imposes on the concrete core. The failure in inclined plan is not typical in high strength concrete, thus, it can be concluded that the steel tube changes the failure mechanism of the concrete core, affecting its behaviour and loading capacity. This change is unfavorable in high strength concrete, as it turns the concrete core into a more damaged system, reducing its capacity. The steel tube has a positive effect as a bracing system of the internal damaged concrete, in the form of distributed micro-pillars.

Failure in inclined planes occurs when the internal damage of the material corresponds to a big number of microcracks, which happens when the progression of cracks is limited. The transversal confinement provided by the steel tube may be understood as a passive confinement. The steel tube stabilizes the cracked concrete core, thus, it is more effective in preventing the cracks progression rather than preventing their formation, contributing to this type of failure.

Using expansive agents in the concrete may delay the crack initiation and consequently the internal destruction processes, improving the behaviour of the concrete core. This may activate the confinement effect provided by the steel tube, enhancing the loading capacity of CFST sections. This technique seems promising, especially when high strength concrete is used, in which the confinement effect is not so effective in improving the loading capacity of CFST sections. Therefore, this technique should be further investigated.

An initial design of a railway long span CFST arch bridge, with a 400 m span, was carried out using different combinations of materials, namely normal and high strength materials. The obtained results demonstrate the advantages of using high-strength materials. The application of high strength materials reduces the structures' self-weight by about the half,

when compared to normal strength combination of materials, resulting in a light structure. The reduction of the concrete quantity is also around the half.

The time-dependent behaviour of the concrete core was predicted based on Age-Adjusted Elastic Modulus (AAEM) method. High strength concrete shows relatively better time-dependent behaviour. Stresses redistribution between the concrete core and the steel tube due to concrete creep was not significant in the adopted steel grades, taking into consideration the adopted tubes' sections. However, concrete creep effect may be significant in imposing additional stresses in the steel tube, in case of using lower steel grades.

It can be concluded that the application of high strength concrete in CFST long span bridges has the advantages of significantly reducing the structure self-weight and the materials consumption. However, the change of failure mechanism of the concrete core due to the steel tube should be taken into account in estimating the loading capacity of CFST sections when high strength concrete is used. Future research in this subject seems to be justified, aiming to develop solutions that increase the loading capacity of CFST solutions using high strength materials. Different concrete compositions, technical measures to increase the contact between the steel tube and the concrete core or to change the failure mode in a favorable way seem to be aspects that can be advantageous to investigate. The answer to those questions can contribute to more effective use of high strength materials, which will permit to construct new arch bridges with longer spans and higher loading capacity.

References

[1] B. C. Chen and T. Lo Wang, "Overview of concrete filled steel tube arch bridges in china," *Pract. Period. Struct. Des. Constr.*, vol. 14, no. 2, pp. 70–80, 2009, doi: 10.1061/(ASCE)1084-0680(2009)14:2(70).

[2] L. H. Han, W. Li, and R. Bjorhovde, "Developments and advanced applications of concrete-filled steel tubular (CFST) structures: Members," *J. Constr. Steel Res.*, vol. 100, pp. 211–228, 2014, doi: 10.1016/j.jcsr.2014.04.016.

[3] X. Zhou, T. Mou, H. Tang, and B. Fan, "Experimental Study on Ultrahigh Strength Concrete Filled Steel Tube Short Columns under Axial Load," *Adv. Mater. Sci. Eng.*, vol. 2017, 2017, doi: 10.1155/2017/8410895.

[4] S. Chen, R. Zhang, L. J. Jia, J. Y. Wang, and P. Gu, "Structural behavior of UHPC filled steel tube columns under axial loading," *Thin-Walled Struct.*, vol. 130, no. March, pp. 550–563, Sep. 2018, doi: 10.1016/j.tws.2018.06.016.

[5] B. Uy and S. B. Patil, "Concrete filled high strength steel box columns for tall buildings: Behaviour and design," *Struct. Des. Tall Build.*, vol. 5, no. 2, pp. 75–94, Jun. 1996, doi: 10.1002/(SICI)1099-1794(199606)5:2<75::AID-TAL69>3.0.CO;2-R.

[6] T. Kitada, "Ultimate strength and ductility of state-of-the-art concrete-filled steel bridge piers in Japan," *Eng. Struct.*, vol. 20, no. 4–6, pp. 347–354, Apr. 1998, doi: 10.1016/S0141-0296(97)00026-6.

[7] "SEG Plaza | Photo | Download image." https://en.phorio.com/file/593092925/ (accessed Dec. 15, 2020).

[8] K. Chen, B. Chen, Q. Zhao, and S. Nakamura, "State-of-the-art of steel arch bridges in China," in *ARCH'10 – 6th International Conference on Arch Bridges*.

[9] F. Huang, X. Yu, and B. Chen, "The structural performance of axially loaded CFST columns under various loading conditions," *Steel Compos. Struct.*, vol. 13, no. November, pp. 451–471, 2012, doi: 10.12989/scs.2012.13.5.451.

[10] Y. Geng, Y. Wang, G. Ranzi, and X. Wu, "Time-dependent analysis of long-span, concrete-filled steel tubular arch bridges," *J. Bridg. Eng.*, vol. 19, no. 4, pp. 1–9, 2014, doi: 10.1061/(ASCE)BE.1943-5592.0000549.

[11] J. Liu, S. Lu, and J. Yuan, "Design and Construction of the Hejiang Yangtze River Highway Bridge," in *Proceedings of ARCH 2019*, vol. 11, Springer, 2019, pp. 553–558.

[12] B. C. Chen, J. G. Wei, and Q. X. Wu, “CHINA TECHNICAL CODE FOR CFST ARCH BRIDGES,” in *8th International Conference on Arch Bridges*, 2016, pp. 363–374.

[13] J. Zheng and J. Wang, “Concrete-Filled Steel Tube Arch Bridges in China,” *Engineering*, vol. 4, no. 1, pp. 143–155, 2018, doi: 10.1016/j.eng.2017.12.003.

[14] T. Mu, B. Fan, X. Zheng, Y. Zheng, and B. Xie, “Wuxia Yangtze River Bridge in Wushan , China,” in *ARCH’07 – 5th International Conference on Arch Bridges*, 2007, pp. 911–918.

[15] “Wushan Yangtze River Bridge - HighestBridges.com.” http://www.highestbridges.com/wiki/index.php%3Ftitle%3DWushan_Yangtze_River_Bridge (accessed Dec. 15, 2020).

[16] W. Wang, W. Yan, L. Deng, and H. Kang, “Dynamic Analysis of a Cable-Stayed Concrete-Filled Steel Tube Arch Bridge under Vehicle Loading,” *J. Bridg. Eng.*, vol. 20, no. 5, p. 04014082, 2015, doi: 10.1061/(asce)be.1943-5592.0000675.

[17] “Zhijinghe Bridge - HighestBridges.com.” http://www.highestbridges.com/wiki/index.php?title=Zhijinghe_Bridge (accessed Dec. 15, 2020).

[18] S. Qin and Z. Gao, “Developments and Prospects of Long-Span High-Speed Railway Bridge Technologies in China,” *Engineering*, vol. 3, no. 6, pp. 787–794, 2017, doi: 10.1016/j.eng.2017.11.001.

[19] B. Chen, J. Liu, and T. Habib, “Recent Research and Application of Arch Bridges in China,” in *Proceedings of ARCH 2019*, Oct. 2019, vol. 11, pp. 536–544, doi: 10.1007/978-3-030-29227-0_57.

[20] “Chengdu-Guiyang railway starts trial operation - Xinhua | English.news.cn.” http://www.xinhuanet.com/english/2019-12/03/c_138601981_5.htm (accessed Dec. 27, 2020).

[21] “Nujiang Railway Bridge Darui - HighestBridges.com.” http://www.highestbridges.com/wiki/index.php?title=Nujiang_Railway_Bridge_Darui (accessed Dec. 27, 2020).

[22] B. Chen, S. Lin, G. Chen, Y. Zhuang, and H. Tabatabai, “Technical report Development and application of concrete arch bridges in China,” *J. Asian Concr. Fed.*, vol. 3, no. 1, pp. 12–19, 2017, doi: 10.18702/acf.2017.06.3.1.12.

[23] Y. Wang, R. Zhao, Y. Jia, and P. Liao, “Time-dependent behaviour analysis of long-

span concrete arch bridge," *Balt. J. Road Bridg. Eng.*, vol. 14, no. 2, pp. 227–248, 2019, doi: 10.7250/bjrbe.2019-14.441.

[24] "Beipanjiang Railway Bridge Qinglong - HighestBridges.com." http://www.highestbridges.com/wiki/index.php?title=Beipanjiang_Railway_Bridge_Qinglong (accessed Dec. 16, 2020).

[25] J. Y. R. Liew, M. Xiong, and D. Xiong, "Design of Concrete Filled Tubular Beam-columns with High Strength Steel and Concrete," *Structures*, vol. 8, pp. 213–226, 2016, doi: 10.1016/j.istruc.2016.05.005.

[26] L. H. Han, D. Y. Ma, and K. Zhou, "Concrete-encased CFST structures: behaviour and application," in *12th International Conference on Advances in Steel-Concrete Composite Structures (ASCCS 2018)*, 2018, doi: 10.4995/ASCCS2018.2018.7109.

[27] "Labajin Bridge - HighestBridges.com." http://highestbridges.com/wiki/index.php%3Ftitle%3DLabajin_Bridge (accessed Dec. 15, 2020).

[28] "Zhaohua Jialing River Bridge - HighestBridges.com." http://www.highestbridges.com/wiki/index.php?title=Zhaohua_Jialing_River_Bridge (accessed Dec. 15, 2020).

[29] "Modaoxi Bridge - HighestBridges.com." http://www.highestbridges.com/wiki/index.php?title=Modaoxi_Bridge (accessed Dec. 15, 2020).

[30] T. Y. Song and K. Xiang, "Performance of axially-loaded concrete-filled steel tubular circular columns using ultra-high strength concrete," *Structures*, vol. 24, no. December 2019, pp. 163–176, Apr. 2020, doi: 10.1016/j.istruc.2019.12.019.

[31] Y. Zhao, "Summary of the development on concrete filled steel tube structure," *Appl. Mech. Mater.*, vol. 256–259, no. PART 1, pp. 670–673, 2013, doi: 10.4028/www.scientific.net/AMM.256-259.670.

[32] B. Chen, Y. Chen, and Z. Qin, "Application of Concrete Filled Steel Tubular arch bridges and study on ultimate load-carrying capacity," *ARCH '04 - 4th Int. Conf. Arch Bridg.*, pp. 1–15, 2004.

[33] S. Rajeev, D. John Peter, and M. V. Varkey, "Study of Concrete Filled Steel Tubular Arch Bridge: A Review," *Appl. Mech. Mater.*, vol. 857, no. 2012, pp. 261–266, 2016, doi: 10.4028/www.scientific.net/amm.857.261.

[34] B. Chen, “New Development of Long Span CFST Arch Bridges In China,” in *Chinese-Croation Joint Colloquium - Long Arch Bridges*, 2008, pp. 357–368.

[35] “EN 1994-1-1 (2004) ‘design of composite steel and concrete structures - Part 1.1: General rules and rules for buildings,’ European commitee for standardization (CEN), Brussels.”

[36] “Specification for Structural Steel Buildings (ANSI/AISC 360-16) | American Institute of Steel Construction, 2016.” .

[37] “Standards Australia, AS/NZS 2327 Composite Structures - Composite Steel-Concrete Construction in Buildings, 2017.”

[38] “Architectural Institute of Japan (AIJ). (2001). Standard for Structural Calculation of Steel Reinforced Concrete Structures, 5th Ed.”

[39] “GB 50923-2013, China National standard-- Technical code for CFST Arch Bridges, 2013.”

[40] E. M. Güneyisi, A. Gültekin, and K. Mermerdaş, “Ultimate capacity prediction of axially loaded CFST short columns,” *Int. J. Steel Struct.*, vol. 16, no. 1, pp. 99–114, 2016, doi: 10.1007/s13296-016-3009-9.

[41] X. Yu and B. Chen, “A New Method for Predicting the UL of Circular CFST Columns,” *Open J. Civ. Eng.*, vol. 03, no. 03, pp. 188–193, 2013, doi: 10.4236/ojce.2013.33023.

[42] K. Sakino, H. Nakahara, S. Morino, and I. Nishiyama, “Behavior of Centrally Loaded Concrete-Filled Steel-Tube Short Columns,” *J. Struct. Eng.*, vol. 130, no. 2, pp. 180–188, Feb. 2004, doi: 10.1061/(ASCE)0733-9445(2004)130:2(180).

[43] G. D. Hatzigeorgiou, “Numerical model for the behavior and capacity of circular CFT columns, Part II: Verification and extension,” *Eng. Struct.*, vol. 30, no. 6, pp. 1579–1589, Jun. 2008, doi: 10.1016/j.engstruct.2007.11.002.

[44] Z. H. Lu and Y. G. Zhao, “Suggested empirical models for the axial capacity of circular CFT stub columns,” *J. Constr. Steel Res.*, vol. 66, no. 6, pp. 850–862, Jun. 2010, doi: 10.1016/j.jcsr.2009.12.014.

[45] X. Xie, H. Z. Chen, H. Li, and S. R. Song, “Numerical analysis of ultimate strength of concrete filled steel tubular arch bridges,” *J. Zhejiang Univ. Sci.*, vol. 6 A, no. 8, pp. 859–868, 2005, doi: 10.1631/jzus.2005.A0859.

[46] H.-T. Thai, S. Thai, T. Ngo, B. Uy, W.-H. Kang, and S. J. Hicks, “Reliability considerations of modern design codes for CFST columns,” *J. Constr. Steel Res.*, vol.

177, p. 106482, Feb. 2021, doi: 10.1016/j.jcsr.2020.106482.

[47] J. Y. Liew and D. X. Xiong, “Ultra-high strength concrete filled composite columns for multi-storey building construction,” *Adv. Struct. Eng.*, vol. 15, no. 9, pp. 1487–1504, 2012, doi: 10.1260/1369-4332.15.9.1487.

[48] S. Guler, A. Çopur, and M. Aydogan, “A Comparative study on square and circular high strength concrete-filled steel tube columns,” *Adv. Steel Constr.*, vol. 10, no. 2, pp. 234–247, 2014.

[49] J. M. Portolés, E. Serra, and M. L. Romero, “Influence of ultra-high strength infill in slender concrete-filled steel tubular columns,” *J. Constr. Steel Res.*, vol. 86, pp. 107–114, Jul. 2013, doi: 10.1016/j.jcsr.2013.03.016.

[50] Z. Huang, B. Uy, D. Li, and J. Wang, “Behaviour and design of ultra-high-strength CFST members subjected to compression and bending,” *J. Constr. Steel Res.*, vol. 175, p. 106351, 2020, doi: 10.1016/j.jcsr.2020.106351.

[51] M. X. Xiong, D. X. Xiong, and J. Y. R. Liew, “Axial performance of short concrete filled steel tubes with high- and ultra-high- strength materials,” *Eng. Struct.*, vol. 136, pp. 494–510, 2017, doi: 10.1016/j.engstruct.2017.01.037.

[52] A. Le Hoang and E. Fehling, “A review and analysis of circular UHPC filled steel tube columns under axial loading,” *Struct. Eng. Mech.*, vol. 62, no. 4, pp. 417–430, 2017, doi: 10.12989/sem.2017.62.4.417.

[53] W. L. A. de Oliveira, S. De Nardin, A. L. H. de Cresce El Debs, and M. K. El Debs, “Influence of concrete strength and length/diameter on the axial capacity of CFT columns,” *J. Constr. Steel Res.*, vol. 65, no. 12, pp. 2103–2110, Dec. 2009, doi: 10.1016/j.jcsr.2009.07.004.

[54] M. X. Xiong, D. X. Xiong, and J. Y. R. Liew, “Behaviour of steel tubular members infilled with ultra high strength concrete,” *J. Constr. Steel Res.*, vol. 138, pp. 168–183, Nov. 2017, doi: 10.1016/j.jcsr.2017.07.001.

[55] F. Abed, M. Alhamaydeh, and S. Abdalla, “Experimental and numerical investigations of the compressive behavior of concrete filled steel tubes (CFSTs),” *J. Constr. Steel Res.*, vol. 80, pp. 429–439, Jan. 2013, doi: 10.1016/j.jcsr.2012.10.005.

[56] T. Ekmekyapar and B. J. M. Al-Eliwi, “Experimental behaviour of circular concrete filled steel tube columns and design specifications,” *Thin-Walled Struct.*, vol. 105, pp. 220–230, Aug. 2016, doi: 10.1016/j.tws.2016.04.004.

[57] Q. Yu, Z. Tao, and Y. X. Wu, “Experimental behaviour of high performance concrete-filled steel tubular columns,” *Thin-Walled Struct.*, vol. 46, no. 4, pp. 362–370, Apr. 2008, doi: 10.1016/j.tws.2007.10.001.

[58] Y. Du, Z. Chen, and M. X. Xiong, “Experimental behavior and design method of rectangular concrete-filled tubular columns using Q460 high-strength steel,” *Constr. Build. Mater.*, vol. 125, pp. 856–872, Oct. 2016, doi: 10.1016/j.conbuildmat.2016.08.057.

[59] K. M. A Hossain and K. Chu, “Confinement of six different concretes in CFST columns having different shapes and slenderness,” *Int. J. Adv. Struct. Eng.*, vol. 11, no. 3, pp. 255–270, 2019, doi: 10.1007/s40091-019-0228-2.

[60] C. Ibañez, D. Hernández-Figueirido, and A. Piquer, “Shape effect on axially loaded high strength CFST stub columns,” *J. Constr. Steel Res.*, vol. 147, pp. 247–256, 2018, doi: 10.1016/j.jcsr.2018.04.005.

[61] S. P, A. Muthuraman, D. G, D. M, J. S, and S. Madumathi, “BEHAVIOR OF CONCRETE-FILLED STEEL TUBES.,” *J. Informatics Math. Sci.*, vol. 10, no. 1 & 2, pp. 297–304, 2018, doi: 10.26713/jims.v10i1-2.1056.

[62] *Mourachev V. Sigalov E, Baıkov V. Construcões de Betão Armado. Lopes Da Silva Editora, Porto; 1980. .*

[63] *Aria Mardalizad, Riccardo Scazzosi, Andrea Manes, Marco Giglio. Testing and numerical simulation of a medium strength rock material under unconfined compression loading. Journal of Rock Mechanics and Geotechnical Engineering. Volume 10, Issue 2.* 2018.

[64] “Pinto C. Design and structural analysis of a new type of slender granite pillar (in Portuguese). MSc thesis, Department of Civil Engineering and Architecture, University of Beira Interior, Covilhã, Portugal; 2008.136p.”

[65] C. Pinto and J. Fonseca, “Mechanical behavior of high strength granite for new prestressed stone structures,” *Int. J. Rock Mech. Min. Sci.*, vol. 60, pp. 452–460, 2013, doi: 10.1016/j.ijrmms.2012.12.010.

[66] A. Kuranovas and A. K. Kvedaras, “Behaviour of hollow concrete-filled steel tubular composite elements,” *J. Civ. Eng. Manag.*, vol. 13, no. 2, pp. 131–141, 2007, doi: 10.1080/13923730.2007.9636429.

[67] M. Johansson, “The efficiency of passive confinement in CFT columns,” *Steel Compos. Struct.*, vol. 2, no. 5, pp. 379–396, Oct. 2002, doi:

10.12989/scs.2002.2.5.379.

[68] J. Brauns and K. Rocens, “THE EFFECT OF MATERIAL STRENGTH ON THE BEHAVIOUR OF CONCRETE-FILLED STEEL ELEMENTS,” *J. Civ. Eng. Manag.*, vol. 10, no. 3, pp. 177–182, Sep. 2004, doi: 10.3846/13923730.2004.9636304.

[69] L. He, S. Lin, and H. Jiang, “Confinement effect of concrete-filled steel tube columns with infill concrete of different strength grades,” *Front. Mater.*, vol. 6, Apr. 2019, doi: 10.3389/fmats.2019.00071.

[70] L. H. Han and G. H. Yao, “Influence of concrete compaction on the strength of concrete-filled steel RHS columns,” *J. Constr. Steel Res.*, vol. 59, no. 6, pp. 751–767, Jun. 2003, doi: 10.1016/S0143-974X(02)00076-7.

[71] N. Khodaie, “Effect of the Concrete Strength on the Concrete-Steel Bond in Concrete Filled Steel Tubes,” *J. Persian Gulf*, vol. 4, no. 11, pp. 9–16, 2013.

[72] Y. M. Hunaiti, “Bond Strength in Battened Composite Columns,” *J. Struct. Eng.*, vol. 117, no. 3, pp. 699–714, Mar. 1991, doi: 10.1061/(ASCE)0733-9445(1991)117:3(699).

[73] M. Johansson and K. Gylltoft, “Mechanical Behavior of Circular Steel–Concrete Composite Stub Columns,” *J. Struct. Eng.*, vol. 128, no. 8, pp. 1073–1081, Aug. 2002, doi: 10.1061/(ASCE)0733-9445(2002)128:8(1073).

[74] M. Nicksiar and C. D. Martin, “Crack initiation stress in low porosity crystalline and sedimentary rocks,” *Eng. Geol.*, vol. 154, pp. 64–76, 2013, doi: 10.1016/j.enggeo.2012.12.007.

[75] “Eberhardt E. Brittle rock fracture and progressive damage in uniaxial compression, PhD thesis, Department of Geological Sciences, University of Saskatchewan, Saskatoon; 1998. 359p.”

[76] Y. Zeng, H. Zhong, C. Liu, H. Tan, and A. B. Gu, “Study of creep effects in a long-span concrete-filled steel tube arch bridge,” *Proc. Inst. Civ. Eng. Struct. Build.*, vol. 171, no. 8, pp. 642–658, 2018, doi: 10.1680/jstbu.17.00003.

[77] M. A. Bradford, Y. L. Pi, and W. Qu, “Time-dependent in-plane behaviour and buckling of concrete-filled steel tubular arches,” *Eng. Struct.*, vol. 33, no. 5, pp. 1781–1795, 2011, doi: 10.1016/j.engstruct.2011.02.018.

[78] K. M. Shrestha, B. chun Chen, and Y. F. Chen, “State of the art of creep of concrete filled steel tubular arches,” *KSCE J. Civ. Eng.*, vol. 15, no. 1, pp. 145–151, 2011, doi: 10.1007/s12205-011-0734-7.

[79] C. Zhi-hua and Y. Jian, “Creep experimental test and analysis of high-performance concrete in bridge,” *J. Cent. South Univ.*, vol. 4, p. 577–581, 2008, doi: 10.1007/s11771.

[80] Y. S. Ma and Y. F. Wang, “Creep of high strength concrete filled steel tube columns,” *Thin-Walled Struct.*, vol. 53, pp. 91–98, 2012, doi: 10.1016/j.tws.2011.12.012.

[81] “Comite Euro-International du Beton (CEB) (1993). 1990 CEB-FIP Model Code 1990: Design Code.”

[82] *ACI Committee 209. (1992). Prediction of creep, shrinkage and temperature effects in concrete structures, American Concrete Institute, Farmington Hills, MI. .*

[83] “Creep and shrinkage prediction model for analysis and design of concrete structures- model B3,” *Mater. Struct.*, vol. 28, no. 6, pp. 357–365, Jul. 1995, doi: 10.1007/BF02473152.

[84] “CEN (European Committee for Standardization). (2004). ‘Design of concrete structures. Part 1-1: General rules and rules for buildings.’ Eurocode 2, Brussels, Belgium.”

[85] Federation internationale du beton, *Fib Model Code for Concrete Structures 2010*, vol. 66. 2012.

[86] P. B. chair) RILEM Technical Committee TC-242-MDC (Zdeněk, “RILEM draft recommendation: TC-242-MDC multi-decade creep and shrinkage of concrete: material model and structural analysis*: Model B4 for creep, drying shrinkage and autogenous shrinkage of normal and high-strength concretes with multi-decade applicability,” *Mater. Struct. Constr.*, vol. 48, no. 4, pp. 753–770, Feb. 2015, doi: 10.1617/s11527-014-0485-2.

[87] Y. Wang, R. Zhao, Y. Jia, and P. Liao, “Creep characteristics of concrete used in long-span arch bridge,” *Balt. J. Road Bridg. Eng.*, vol. 14, no. 1, pp. 18–36, 2019, doi: 10.7250/bjrbe.2019-14.431.

[88] Y. Geng, “TIME-DEPENDENT BEHAVIOUR OF CONCRETE-FILLED STEEL TUBULAR ARCH BRIDGES,” PhD thesis. The University of Sydney, 2011.

[89] “EN1991-2(2003) –‘Actions on Structures – Part 2: General Actions - Traffic loads on Bridges’ European commitee for standardization (CEN), Brussels.”

[90] “EN 1991-1-4(2005)-‘Actions on Structures – Part 4: General Actions – Wind actions’, European commitee for standardization (CEN), Brussels.”

[91] “EN 1990 – Anexo 2 (2002) –‘Basic of Structural Design, anexo 2: Applications for bridges (normative)’, European Committe for Standardization (CEN), Final PT Draft, Brussels.”

[92] “Autodesk Robot Structural Analysis Program.” 2019.

[93] “EN 1993-1-1, ‘Design of steel structures - Part 1-1: General rules and rules for buildings’ European commitee for standardization (CEN), Brussels.,” .

[94] “EN 1993-2, ‘Design of steel structures - Part 2: Steel bridges’ European commitee for standardization (CEN), Brussels.”

[95] “Interac, programa utilizado no Departamento de Engenharia Civil e Arquitetura UBI, na unidade curricular de Estruturas Especiais.” .

[96] W. X. Liu, B. Zhu, Z. L. Yu, and X. Han, “Seismic response analysis of Yachi River super-large bridge,” in *Procedia Engineering*, Jan. 2011, vol. 12, pp. 149–155, doi: 10.1016/j.proeng.2011.05.024.

Appendix A The age-adjusted effective modulus method (AAEM) (FIB 2010)

The age-adjusted effective modulus method (AAEM) as described in FIB 2010 [85] is calculated based on expression (A-1).

$$E_{c,adj}(t,t_0) = \frac{E_{ci}(t_0)}{1 + \chi(t,t_0)[E_{ci}(t_0)/E_{ci}]\varphi_{28}(t,t_0)} \quad \text{(A-1)}$$

Where

$\chi(t,t_0)$ is the aging coefficient, the values are between 0.6 and 0.9 for typical values of to

E_{ci} is the modulus of elasticity of concrete at the age of 28 days (expression (A-2))

$\varphi_{28}(t,t_0)$ is the creep coefficient

$$E_{ci} = E_{c0}\left(\frac{f_{ck} + \Delta f}{10}\right)^{1/3} \quad \text{(A-2)}$$

With

E_{c0} =21.5 . 10^3 MPa

Δf =8 MPa

The modulus of elasticity of concrete at an age different than 28 days is obtained according to expression (A-3).

$$E_{ci}\,(t) = \,(\beta_{cc}(t))^{0.5}\,E_{ci} \quad \text{(A-3)}$$

With

$$\beta_{cc}(t) = exp\left\{s.\left[1 - \left(\frac{28}{t}\right)^{0.5}\right]\right\} \quad \text{(A-4)}$$

Where *s* is a coefficient related to strength class of cement. Taken as 0.20 for concrete grade higher than C60.

The creep coefficient may be estimated from expression (A-5).

$$\varphi(t,t_0) = \varphi_{bc}(t,t_0) + \varphi_{dc}(t,t_0) \quad \text{(A-5)}$$

Where

$\varphi_{bc}(t,t_0)$ is the basic creep coefficient

$\varphi_{dc}(t,t_0)$ is the drying creep coefficient

t is the age of concrete at the considered moment

t_o is the age of concrete at loading

The basic creep coefficient $\varphi_{bc}(t,t_0)$ can be calculated according to expression (A-6).

$$\varphi_{bc}(t,t_0) = \beta_{bc}(f_{cm})\beta_{bc}(t,t_0) \quad \text{(A-6)}$$

With

$$\beta_{bc}(f_{cm}) = \frac{1.8}{(f_{cm})^{0.7}} \tag{A-7}$$

$$\beta_{bc}(t, t_0) = \ln\left(\left(\frac{30}{t_0} + 0.035\right)^2 (t - t_0) + 1\right) \tag{A-8}$$

The drying creep coefficient $\phi_{dc}(t, t_0)$ may be calculated from expression (A-9).

$$\varphi_{dc}(t, t_0) = \beta_{dc}(f_{cm})\, \beta_{dc}(RH)\, \beta_{dc}(t, t_0)\, \beta_{dc}(t_0) \tag{A-9}$$

With

$$\beta_{dc}(f_{cm}) = \frac{412}{(f_{cm})^{1.4}} \tag{A-10}$$

$$\beta_{dc}(RH) = \frac{1 - \frac{RH}{100}}{\sqrt[3]{0.1\ \frac{h}{100}}} \tag{A-11}$$

$$\beta_{dc}(t_0) = \frac{1}{0.1 + {t_0}^{0.2}} \tag{A-12}$$

$$\beta_{dc}(t, t_0) = \left[\frac{(t, t_0)}{\beta_h + (t, t_0)}\right]^{\gamma(t_0)} \tag{A-13}$$

Where

$$\gamma(t_0) = \frac{1}{2.3 + \frac{3.5}{\sqrt{t_0}}} \tag{A-14}$$

$$\beta_h = 1.5\ h + 250\ \alpha_{f_{cm}} \leq 1500\ \alpha_{f_{cm}} \tag{A-15}$$

$$\alpha_{f_{cm}} = \left(\frac{35}{f_{cm}}\right)^{0.5} \tag{A-16}$$

f_{cm} is the mean compressive strength of concrete

RH is the relative humidity

h $=2A_c/u$, where u is the perimeter of the member in contact with atmosphere

However, the creep is assumed to have a linear relation with the stress for service stresses within the range $|\sigma_c| \leq 0.4\, f_{cm}(t_0)$. For high stresses in the range $0.4\, f_{cm}(t_0) \leq |\sigma_c| \leq 0.6 f_{cm}(t_0)$, the nonlinearity of creep is taken into account using expression (A-17).

$$\varphi_\sigma(t, t_0) = \varphi(t, t_0) \exp[1.5(k_\sigma - 0.40] \tag{A-17}$$

With

$$k_\sigma = |\sigma_c|/f_{cm}(t_0) \quad \text{(A-18)}$$

Appendix B Wind action

Wind action was defined according to EN1991-1-4 [90]. The Basic wind speed considered is 27 m/s. regarding the air density ρ, it was considered 1.25 kg/m^3 while the construction height is 300 meters.

Wind action on the Deck

Wind forces acting on a bridge deck is defined as follows:

$$F_w = \frac{1}{2} . \rho . v_b^2 . C . A_{ref,x} \quad \text{(B-1)}$$

Where:

V_b is the basic wind speed

C is the wind load factor

$A_{ref,x}$ is the reference area

ρ is the density of air

The expression to calculate the wind load factor C is as follows:

$$C = C_e(z)\, C_{f,x} \quad \text{(B-2)}$$

Where:

$C_e(z)$ is the exposure coefficient

$C_{f,x}$ is a force coefficient for bridges

The exposure coefficient $C_e(Z_x)$ is obtained using the following formula:

$$C_e(z) = \frac{q_b(z)}{q_b} \quad \text{(B-3)}$$

q_b (z) is the peak velocity pressure at height z and is given by the following expression:

$$q_b(z) = [1 + 7\, I_v(z)]\, \frac{1}{2}\, \rho\, v_m^2(z) \quad \text{(B-4)}$$

Where

ρ is the air density

I_v (z) is the turbulence intensity at height z

V_m (z) is the mean wind velocity at a height z

q_b is the basic velocity pressure given in the following expression:

$$q_b = \frac{1}{2} . \rho\, v_b^2 \quad \text{(B-5)}$$

Where

V_b is the basic wind speed

ρ is the air density

Wind turbulence

The recommended rule for the determination of I_v (z) is given as:

$$I_v(z) = \frac{K_I}{C_0\,(z)\,.\,ln(z/z_0)} \tag{B-6}$$

K_I is the turbulence factor. The recommended value is 1,0.

C_o is the orography factor. It has a value of 1 since the bridge is located in a valley.

Z_o is the roughness length. It equal to 0.05 according to table 4.1 of EN1991-1-4.

Therefore,

$$I_V(z) = \frac{1}{1\ \times\ ln(300/0.05)} = 0.11 \tag{B-7}$$

The mean wind velocity V_m (z)

V_m (z) is the mean wind velocity is calculated by the following expression:

$$V_m(z) = C_r(z)\ C_0(z) V_b \tag{B-8}$$

Where:

C_r(z) is the roughness factor.

C_0(z) is the orography factor. Taken as 1.

C_r(z) is calculated from the expression:

$$C_r(z) = K_r\ .\ ln(z/z_0) \tag{B-9}$$

Where:

Z_o is the roughness length

K_r is a Terrain factor depending on the roughness length Z_o calculated as:

$$K_r\ = 0.19\ (\frac{z0}{z0.II})^{0.07} \tag{B-10}$$

$Z_{0.II}$ = 0.05 m (terrain category II)

$$K_r\ = 0.19\ (\frac{0.05}{0.05})^{0.07} \tag{B-11}$$

Back to roughness factor expression:

$$C_r(\mathrm{z}) = 0.19\ \times\ \ln\left(\frac{300}{0.05}\right) = 1.65 \tag{B-12}$$

The mean wind velocity is obtained as:

$$V_m(z) = 1.65 \times 1 \times 27 = 44.55\ m/s \tag{B-13}$$

Peak velocity pressure

The peak velocity pressure is calculated as:

$$q_b\ (\mathrm{z})\ = [1 + 7 \times\ 0.11)\ ]\frac{1}{2} \times 1.25 \times 44.55 =\ 2195.58\ \mathrm{kg/ms^2} \tag{B-14}$$

q_b is the basic velocity pressure given in the following expression:

$$q_b = \frac{1}{2} \times 1.25 \times 27^2 = 455.63 \text{ kg/ms}^2 \quad \text{(B-15)}$$

The exposure coefficient $C_e(z)$ then is obtained as:

$$C_e(z) = \frac{2195.58}{455.63} = 4.82 \quad \text{(B-16)}$$

The coefficient of forces $C_{f,x}$ is taken from the following figure:

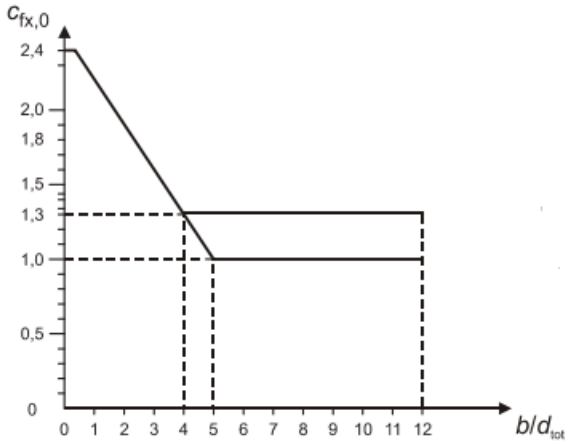

Figure B-1 Force coefficient for bridges (adapted from [90])

Regarding the calculation of b/d_{tot} ratio, d_{tot} value corresponds to the height of the deck plus one factor that takes in account the shape of the guardrails, in this case the guardrails were considered hollow from the two sides, thus:

$$d_{tot} = 4 + 0.6 = 4.6\, m \quad \text{(B-17)}$$

b is the width of the deck, the b/d_{tot} ratio is given as:

$$\frac{b}{d_{tot}} = \frac{14}{4.6} = 3.04 \quad \text{(B-18)}$$

From Figure B-1: $C_{f,x} = 1.58$

Therefore, the wind load factor is calculated as:

$$C = 4.82 \times 1.58 = 7.616 \quad \text{(B-19)}$$

The height of the reference area was considered to be 4.6 meters, since it is 4 meters height plus 0.6 relative to the guardrails, then:

$$A_{ref} = 4.6 \times 1 = 4.6\, m^2/m \quad \text{(B-20)}$$

Finally, wind forces on the deck are calculated as:

$$F_w = \frac{1}{2} \times 1.25 \times 27^2 \times 7.616 \times 4.6 = 15962.18\, N/m = 15.96\, KN/m \quad \text{(B-21)}$$

Wind action on the arch

Wind force for the arch is calculated by the following expression:

$$F_w = C_s C_d \; C_f \; q_p(z_e) \; A_{ref} \tag{B-22}$$

Where:

$C_S C_d$ is the structural factor considered as 1.

C_d is the force coefficient for the structure or structural element

$q_p(z_e)$ is the peak velocity pressure

A_{ref} is the reference area of the structure or structural element

Peak velocity pressure

Firstly, the peak velocity pressure is calculated using the following expression:

$$q_b(z) = C_e(z)\frac{1}{2}\,\rho\, {V_b}^2 \tag{B-23}$$

Where:

C_e is the exposure coefficient

V_b is the basic wind speed

ρ is the density of air

The coefficient C_e is obtained using the following formula:

$$c_e(z_e) = \left(1 + \frac{7}{ln\frac{z_e}{z_0}}\right)\left(0.19\; ln\,(\frac{z_e}{z_0})\right)^2 \tag{B-24}$$

Where:

Z_e is the reference height

Z_o is the roughness length

$$C_e(z_e) = \left(1 + \frac{7}{ln\frac{300}{0.05}}\right)\left(0.19\, ln\left(\frac{300}{0.05}\right)\right)^2 = 4.93 \tag{B-25}$$

The peak velocity pressure:

$$q_b(z) = 4.93 \times \frac{1}{2} \times 1.25 \times 27^2 = 2.246\; kg/ms^2 \tag{B-26}$$

Force coefficient

The force coefficient is calculated using the following expression:

$$C_f = C_{f,0}\; \Psi_\lambda \tag{B-27}$$

Where:

$C_{f.o}$ is the force coefficient of cylinders without free-end flow

Ψ_λ is the end-effect factor

$C_{f.o}$ is taken from the figure 7.28 in EN1991-1-4.which is based on the Reynolds number.

$$Re = \frac{b.v(Ze)}{v} \quad \text{(B-28)}$$

b is the diameter

v is the kinematic viscosity of the air (v= 15.10^{-6} m^2/s)

V(z_e) is the peak wind velocity

$$V(z_e) = \sqrt{\frac{2qb}{\rho}} = \sqrt{\frac{2 \times 2246}{1.25}} = 59.95\ m/s \quad \text{(B-29)}$$

$$R_e = \frac{1.36 \times 59.95}{15 \times 10^{-6}} = 5.4355 \times 10^6 \quad \text{(B-30)}$$

From figure 7.28 in EN1991-1-4:

$$C_{f,0} = 1.2 + \frac{0.18\, log(10\frac{k}{b})}{1 + 0.4 log(\frac{R_e}{10^6})} = 0.806 \quad \text{(B-31)}$$

With

K=0.2 mm table 7.13 (for surface type "galvanized steel" table 7.13 of EN1991-1-4)

b= 1.36 m

k/b=0.000147

The end-effect factor Ψ_λ

The end-effect factor should be determined as a function of slenderness ratio λ *and* solidity ratio ϕ.

λ= 70 from table 7.16 in EN1991-1-4.

Solidity ratio is given by the following expression:

$$\phi = \frac{A}{Ac} \quad \text{(B-32)}$$

A is the sum of the projected areas of the members

Ac is the overall envelope area

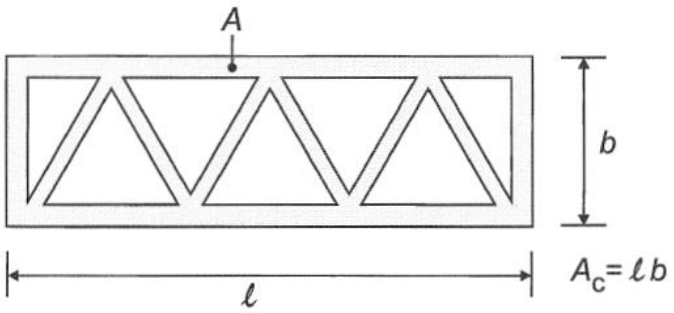

Figure B-2 Definition of solidity ratio φ

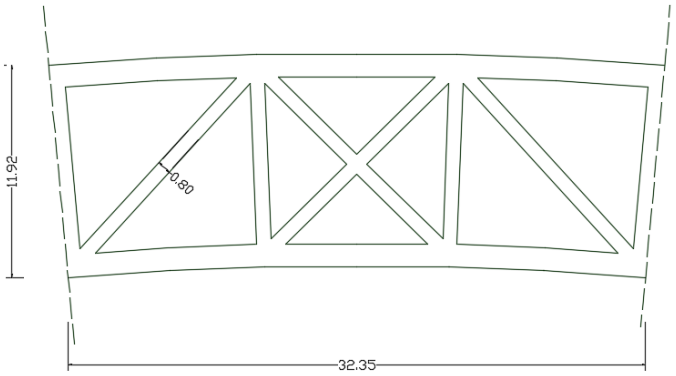

Figure B-3 Definition of solidity ratio φ

Ψ_λ= 0.98 the end-effect factor from figure 7.36 in EN1991-1-4.

Therefore, The force coefficient:

$$C_f = 0.806 \times 0.98 = 0.790 \tag{B-33}$$

The influence area in arch crown:

$$A_{ref} = d_{tot} l = 11.92\ m^2/m \tag{B-34}$$

Replacing the expression of the wind force, we obtain:

$$F_w = 2.246 \times 0.790 \times 11.92 = 21.15\ \text{KN/m} \tag{B-35}$$

There are 2 tube in each side, the wind force on each tube:

$$F_w = 21.15/2 = 10.58\ \text{KN/m} \tag{B-36}$$

The influence area in arch springing:

$$A_{ref} = d_{tot} l = 16.10\ m^2/m \tag{B-37}$$

The wind force:

$$\begin{gathered} F_w = 2.246 \times 0.790 \times 16.10 = 28.57\ \text{KN/m} \\ F_w = 2.246 \times 0.790 \times 16.10 = 28.57\ \text{KN/m} \end{gathered} \tag{B-38}$$

The wind force for each tube:

$$F_w = 28.57/2 = 14.29\ \text{KN/m} \tag{B-39}$$

The average value between the wind force in arch springing and in arch crown will be considered, obtaining F_w= 12.44 KN/m

Wind action on the columns

The calculation of the wind action on the columns involved only the calculation of one column, since all the columns have the same influence area. Wind force for columns is calculated by expression (B-22). The value of the peak velocity pressure is the same value obtained for the arch, mentioned in expression (B-26).

Force coefficient

The force coefficient is calculated using the expression (B-27). The Reynolds number is calculated by the following expression:

$$Re = \frac{0.73 \times 59.95}{15 \times 10^{-6}} = 2.917567 \times 10^{6} \quad \text{(B-40)}$$

Thus, $C_{f.o}$ is calculated as follows:

$$C_{f,0} = 1.2 + \frac{0.18 \log(10 \frac{k}{b})}{1 + 0.4 \log(\frac{Re}{10^6})} = 0.811 \quad \text{(B-41)}$$

With

K=0.2 mm (for surface type "galvanized steel" table 7.13 of EN1991-1-4)

b= 0.73 m

k/b=0.000274

The end-effect factor Ψ_λ

λ= 70 from table 7.16 in EN1991-1-4. The solidity ratio is taken as 1, since the calculation is performed for 1 columns. The end-effect factor is obtained from figure 7.36 in EN1991-1-4: Ψ_λ= 0.92.

Therefore, The force coefficient:

$$C_f = 0.811 \times 0.92 = 0.746 \quad \text{(B-42)}$$

The influence area:

$$A_{ref} = 1 \,.\, b = 0.73\ m^2/m \quad \text{(B-43)}$$

Finally replacing the expression of the wind force, we obtain:

$$F_w = 2.246 \times 0.749 \times 0.73 = 1.23\ \text{KN/m} \quad \text{(B-44)}$$

F_w=1.6 KN/m is adopted.

The wind forces on the different bridge segments are listed in Table B-1. These values are used for all the solutions.

Table B-1 Wind forces

Segment	Force KN/m
Deck	15.96
Column	1.6
Arch tube	12.44

Appendix C Interaction factors

The interaction factors are obtained according to EN1993-1-1 [93], using the following expressions.

$$k_{yy} = C_{my}C_{mLT}\frac{\mu_y}{1-\frac{N_{Ed}}{N_{cr,y}}}\frac{1}{C_{yy}} \tag{C-1}$$

$$k_{yz} = C_{mz}\frac{\mu_y}{1-\frac{N_{Ed}}{N_{cr,z}}}\frac{1}{C_{yz}}0.6\sqrt{\frac{w_z}{w_y}} \tag{C-2}$$

$$k_{zy} = C_{my}C_{mLT}\frac{\mu_z}{1-\frac{N_{Ed}}{N_{cr,y}}}\frac{1}{C_{zy}}0.6\sqrt{\frac{w_y}{w_z}} \tag{C-3}$$

$$k_{zz} = C_{mz}\frac{\mu_z}{1-\frac{N_{Ed}}{N_{cr,z}}}\frac{1}{C_{zz}} \tag{C-4}$$

With

$$C_{yy} = 1+(w_y-1)\left[\left(2-\frac{1.6}{w_y}C_{my}^2\bar{\lambda}-\frac{1.6}{w_y}C_{my}^2\bar{\lambda}^2\right)n_{pl}-b_{LT}\right] \geq \frac{w_{el.y}}{w_{pl.y}} \tag{C-5}$$

$$C_{yz} = 1+(w_z-1)\left[\left(2-14\frac{C_{mz}^2\bar{\lambda}^2}{w_z^5}\right)n_{pl}-c_{LT}\right] \geq 0.6\sqrt{\frac{w_z}{w_y}}\frac{w_{el.z}}{w_{pl.z}} \tag{C-6}$$

$$C_{zy} = 1+(w_y-1)\left[\left(2-14\frac{C_{my}^2\bar{\lambda}^2}{w_y^5}\right)n_{pl}-d_{LT}\right] \geq 0.6\sqrt{\frac{w_y}{w_z}}\frac{w_{el.y}}{w_{pl.y}} \tag{C-7}$$

$$C_{zz} = 1+(w_z-1)\left[2-\frac{1.6}{w_z}C_{mz}^2\bar{\lambda}-\frac{1.6}{w_z}C_{mz}^2\bar{\lambda}^2-e_{LT}\right]n_{pl} \geq \frac{w_{el.z}}{w_{pl.z}} \tag{C-8}$$

$$n_{pl} = \frac{N_{Ed}}{N_{Rk}} \tag{C-9}$$

$$C_{mi} = 0.79+0.21\psi_i+0.36(\psi_i-0.33)\frac{N_{Ed}}{N_{cr.i}} \tag{C-10}$$

Moment diagram:

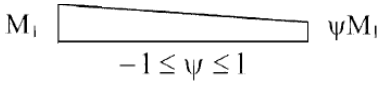

$$\mu_y = \frac{1-\frac{N_{Ed}}{N_{cr,y}}}{1-\chi_y\frac{N_{Ed}}{N_{cr,y}}} \tag{C-11}$$

$$\mu_z = \frac{1 - \frac{N_{Ed}}{N_{cr,z}}}{1 - \chi_z \frac{N_{Ed}}{N_{cr,z}}} \tag{C-12}$$

$$w_y = \frac{w_{pl,y}}{w_{el,y}} \leq 1.5 \tag{C-13}$$

$$w_z = \frac{w_{pl,z}}{w_{el,z}} \leq 1.5 \tag{C-14}$$

Solution of two-tubes rib section

Since the tubes section is circular, it will not be subjected to lateral torsional buckling. Thus, the factors related to lateral torsional buckling $C_{mLT}, b_{LT}, c_{LT}, d_{LT}, e_{LT}$ will be taken as 1.

Table C-1 Determination of μ_i

Solution	N_{Ed} (MN)	$N_{cr,i}$ (MN)	χ_i	μ_i
C60/S460	85.62	1036.15	0.95	1.00
	51.93	943.48	0.66	0.98
C160/S700	60.29	456.52	0.86	0.98
	26.48	240.80	0.66	0.96

Table C-2 Determination of C_{my}

Solution	$M_{y,min}$ (MNm)	$M_{y,max}$ (MNm)	ψ_y	C_{my}
C60/S460	0.314	-0.445	0.706	0.950
	2.107	3.040	0.693	0.942
C160/S700	0.163	0.565	0.288	0.849
	-0.763	-0.957	0.797	0.976

Table C-3 Determination of C_{mz}

Solution	$M_{z,min}$ (MNm)	$M_{z,max}$ (MNm)	ψ_z	C_{mz}
C60/S460	-0.455	-0.985	0.467	0.891
	6.091	7.794	0.781	0.963
C160/S700	-0.479	-0.638	0.752	0.968
	5.708	6.236	0.915	1.005

Table C-4 Determination of C_{ij}

Solution	n_{pl}	$W_{pl,i}$ (cm^3)	$W_{el,i}$ (cm^3)	W_i	$\bar{\lambda}$	C_{yy}	C_{zz}	C_{yz}	C_{zy}
C60/S460	0.38	415669.51	316223.32	1.31	0.50	1.14	1.15	1.15	1.14
	0.23	415669.51	316223.32	1.31	0.52	1.08	1.08	1.08	1.08
C160/S700	0.24	215669.71	162162.11	1.33	0.79	1.06	1.03	1.00	1.04
	0.11	215669.71	162162.11	1.33	1.08	0.98	0.97	0.93	0.94

Table C-5 Interaction factors

Solution	k_{yy}	k_{zz}	k_{zy}	k_{yz}
C60/S460	0.90	0.84	0.54	0.50
	0.90	0.93	0.54	0.56
C160/S700	0.90	1.06	0.55	0.65
	1.07	1.11	0.67	0.70

Solution of truss rib section

Table C-6 Determination of μ_i

Solution	N_{Ed} (MN)	$N_{cr,i}$ (MN)	χ_i	μ_i
C60/S460	63.12	800.80	0.96	1.00
	38.96	800.74	0.96	1.00
C160/S700	39.71	316.47	0.90	0.99
	16.03	316.43	0.90	0.99

Table C-7 Determination of C_{my}

Solution	$M_{y,min}$ (MNm)	$M_{y,max}$ (MNm)	ψ_y	C_{my}
C60/S460	0.026	-1.608	-0.016	0.777
	-0.518	-1.791	0.289	0.850
C160/S700	0.371	-1.092	-0.339	0.688
	-0.222	-1.322	0.168	0.822

Table C-8 Determination of C_{mz}

Solution	$M_{z,min}$ (MNm)	$M_{z,max}$ (MNm)	ψ_z	C_{mz}
C60/S460	-0.412	-0.898	0.459	0.890
	1.335	-4.543	-0.294	0.717
C160/S700	-0.176	-0.550	0.321	0.857
	0.259	-3.103	-0.084	0.765

Table C-9 Determination of C_{ij}

Solution	n_{pl}	$W_{pl,i}$ (cm^3)	$W_{el,i}$ (cm^3)	W_i	$\bar{\lambda}$	C_{yy}	C_{zz}	C_{yz}	C_{zy}
C60/S460	0.45	215250.92	164333.74	1.31	0.45	1.21	1.19	1.20	1.22
	0.28	215250.92	164333.74	1.31	0.45	1.12	1.14	1.14	1.13
C160/S700	0.30	86718.20	65191.56	1.33	0.70	1.13	1.09	1.08	1.12
	0.12	86718.20	65191.56	1.33	0.70	1.04	1.05	1.04	1.04

Table C-10 Interaction factors

Solution	k_{yy}	k_{zz}	k_{zy}	k_{yz}
C60/S460	0.69	0.81	0.41	0.48
	0.79	0.66	0.47	0.40
C160/S700	0.69	0.88	0.42	0.54
	0.83	0.77	0.50	0.46